INAUGURAL - DISSERTATION
zur
Erlangung der Doktorwürde
der
Naturwissenschaftlich-Mathematischen Gesamtfakultät
der
Ruprecht-Karls-Universität
Heidelberg

vorgelegt von
Diplom-Physiker Jens Prager
geboren in Frankfurt/Oder
Tag der mündlichen Prüfung: 19.10.2005

Title:

Modeling and Simulation of Charged Species in Lean Methane-Oxygen Flames

Gutachter: Prof. Dr. Dr. h. c. Jürgen Warnatz
PD Dr. Uwe Riedel

Abstract

Charged species occur in all combustion systems. Chemical pathways which involve ions are known to contribute to the formation of air pollutants like soot and aerosols. The appearance of electrical charges, which are closely related to the combustion process itself, offers the opportunity of their use for sensing purposes in a variety of applications.

Reliable models for the chemical reaction network and the transport processes are required for numerical simulations in these fields of research. Laminar flat flames have proven to be suitable systems for the development and validation of chemical reaction mechanisms.

In this work, the concentrations of charged species along a flat, fuel-lean, and laminar methane-oxygen flame are calculated and compared to experimental results. For the first time, these simulations also include negative ions. Existing software was enhanced to enable the inclusion of these ions.

The chemical reaction mechanism of the charged species is compiled from different sources found in according literature. Altogether, the model contains 65 reversible reactions involving 11 charged species.

Also special emphasis is put on the diffusion processes of the ions. A model is developed and discussed which describes the mutual interactions of the charged species during diffusion. It allows an arbitrary fraction of negative ions, because it does not depend on the assumption that the electrons dominate this process.

The simulations are used to validate the reaction mechanism. Reaction flow analyses show which chemical pathways are taken. Reactions which were suggested in the literature are discussed quantitatively. The influence of charged species diffusion on the simulation results as well as their sensitivities to uncertainties in the input data of the transport model are analyzed.

Kurzfassung

Geladene Spezies treten in allen Verbrennungssystemen auf. Es ist bekannt, daß Reaktionswege, die Ionen beinhalten, zur Bildung von Luftschadstoffen wie Ruß und Aerosolen beitragen. Das Auftreten elektrischer Ladungen, die in einem direkten Zusammenhang zum Verbrennungsprozess stehen, bietet die Möglichkeit, sie für sensorische Zwecke in einer Vielzahl von Anwendungen zu benutzen.

Für numerische Simulationen auf diesen Forschungsgebieten werden verläßliche Modelle für das Netzwerk aus chemischen Reaktionen und die Transportprozesse benötigt. Laminare flache Flammen haben sich als geeignete Systeme erwiesen, um an ihnen chemische Reaktionsmechanismen zu entwickeln und zu validieren.

In dieser Arbeit werden die Konzentrationen geladener Spezies in einer mageren, laminaren Methan-Sauerstoff-Flamme berechnet und mit experimentellen Daten verglichen. Diese Simulationen beinhalten zum ersten Mal auch negative Ionen. Vorhandene Software wurde erweitert, um Ionen berücksichtigen zu können.

Ein Reaktionsmechanismus der geladenen Spezies wurde aus verschiedenen Quellen in der Literatur erstellt. Das Modell enthält 11 geladene Spezies und 65 reversible Reaktionen zwischen ihnen.

Besonders herausgestellt werden auch die Diffusionsprozesse der Ionen. Ein Modell wird entwickelt und diskutiert, das die gegenseitige Wechselwirkung der geladenen Spezies während der Diffusion beschreibt. Es sind beliebige Anteile an negativen Ionen erlaubt, weil es nicht von der Annahme abhängt, daß die Elektronen diesen Prozeß dominieren.

Die Simulationen dienen der Validierung des Reaktionsmechanismus. Reaktionsflußanalysen zeigen, welche Reaktionspfade eingeschlagen werden. Reaktionen, die in der Literatur vorgeschlagen wurden, werden quantitativ diskutiert. Der Einfluß der Diffusion geladener Spezies auf die Simulationsergebnisse sowie deren Empfindlichkeit bezüglich der Unsicherheiten in den Eingangsdaten des Transportmodells werden analysiert.

Contents

Chapter 1

Introduction

Charged atoms or molecules appear in many gaseous reactive systems. Generally speaking, the chemistry in the interstellar medium as well as all different plasma processes can provide examples. Also in the upper parts of the earth's atmosphere charged species are observed [SS95].

Ions are also found in combustion systems. For more than 100 years, it has been known that flames can be influenced by the application of an external electric field. Charged species are discussed to take part in possible reaction pathways forming pollutants like soot [Fia97, COK88] and aerosols which are produced by aircraft turbine engines in the atmosphere [SSTS02, SVM03]. Ions occur in ignition processes like spark ignition [TSR$^+$00, YKT$^+$02] or laser ignition of fuel mixtures [LCW$^+$04].

The interest in ions in combustion systems has grown again during the last years because of their use for detection purposes. Even though the concentrations of ions in combustion systems are generally low in comparison to the concentrations of neutral species, the electrical conductivity can be easily measured and provides information on the combustion process. The determination of the so-called ion current is used in some modern car engines. In spark ignition engines, the spark plug itself can be used as a sensor, if a voltage is applied to it after the discharge process. This procedure offers a simple and low-cost method of measuring the current state of the combustion process. This information can be used for electronic engine management. The ion signal as a way of pressure measurement can detect misfire [MSF$^+$05, FGKW99, SRM97], but it can also be used to give information about the local air-to-fuel ratio at the spark plug for direct-injection engines [UR98, RSM97].

This variety of examples shows the great interest in a detailed knowledge of the underlying chemical processes in these systems. An additional motivation is to gain understanding of how to predict or control the system behavior. Numerical simulations have proven to be valuable tools for achieving this goal,

since complex models can be quantified and assumptions can be validated against experimental data. Highly detailed information about the system which is obtained, helps to analyze and understand the mechanisms. The development of reliable and predictive models for the chemical processes is a challenging task, but it is a necessary precondition for simulations in these fields of application.

1.1 Ions in flames

Charged species in flames have been an active subject of research which, for instance, is shown in the extensive review of Fialkov [Fia97]. Especially laminar premixed flames have proven to be very suitable for studying ion chemistry in combustion systems. Most of the flames have been studied at low pressure, because, in this case, the flame thickness is larger. But there are also some experiments which were carried out at atmospheric pressure.

The main question has been how these charged species appear in the flames. This includes the identification of the ionization processes and also the identification of how an ion is converted into another one. It was found that not thermal ionization is responsible for the ions but chemiionization reactions, i. e., chemical reactions of two neutral species which lead to a cation and an anion at temperatures which are too low for thermal ionization. Much of the early research has been concerned with the identification of these chemiionization reactions and the global ionic structure of the flames, depending on the type of fuel and stoichiometry. Optical techniques, but mostly saturation-current and Langmuir-probe methods, have been utilized in these experiments. To measure electrical saturation currents, an electric field is applied to the flame and the voltage-current characteristic is obtained. Langmuir-probe studies utilize an electric probe which is positioned in variable regions of the flame. They also measure the dependence of the electrical current on the applied voltage relative to the burner. Electron concentrations and total charge concentrations have been obtained with this method.

Beam sampling methods have made it possible to measure and identify concentration profiles of single species since the charge-to-mass ratio of the ions can be determined in the analyzer after sampling. These measurements have built up the hopes to also get indirect experimental access to concentrations of neutral species which can not be observed by other methods. But this approach requires a good knowledge of the ion chemistry to interpret the experimental data.

1.2 Simulations of premixed flat flames

Even though there has been much interest in the experimental side of the ion chemistry of flames, only a few publications exist which aim to quantify suggested ion reaction mechanisms using numerical simulations of these flames.

One publication examines the effects of an applied electric field to a lean, a stoichiometric, and a rich methane-oxygen flame at atmospheric pressure [PB93]. This work focuses on the prediction of saturation currents and their relation to individual ion reactions. The species concentration profiles are also compared to experimental data. Five positive ions are included in the reaction mechanism, but negative ions are neglected. Overall, the kinetic mechanism consists of 13 ion reactions. Ambipolarity of the diffusion fluxes, which maintains local charge neutrality, is accounted for indirectly by solving Poisson's equation for the electric field. However, the diffusion coefficients of the ions are taken to be the same as the diffusion coefficients of the corresponding neutrals. The calculations show that the peak ion concentration of three ions are reproduced well, but the species profiles agree only qualitatively. The lean methane-oxygen flame is also studied in this thesis, so that the results can be compared to the simulation results of this earlier work.

In two earlier publications of the same research group, the ion chemistry in lean, close-to-stoichiometric, and rich acetylene flames at low pressure are studied numerically [BE88, EB88]. The main focus of this research is on the compilation of a detailed ionic reaction mechanism and its validation against experimental data. The numerical model of a one-dimensional, laminar, premixed flame is similar to the one presented in this work. Overall, 12 positive ions are included in the model, but again, negative ions are excluded. The kinetic mechanism for the ions consists of 62 reactions, but many of the reaction rates are estimated due to lack of experimental data. Ambipolar diffusion is neglected in this early work. The ions diffuse in the same way as uncharged species with the diffusion coefficients of their corresponding neutrals. While the total ion concentration and its dependence on the stoichiometry is reproduced well in their calculations, the species profiles agree qualitatively only in the stoichiometric case.

1.3 Objective of this work

It is the objective of this thesis to enable simulations of ionic species in laminar premixed flat flames. The lean methane-oxygen flame studied by Goodings et al. [GBN79a, GBN79b] is calculated and used for evaluation, because it offers by far the most detailed experimental data. The approach employed is similar to the methodology used in the papers cited above. But for the first time, also negative

ions are regarded in the simulations.

Fuel-lean flames are characterized by an excess of oxygen. Especially in this case, negative ions occur in concentrations comparable to positive ions. It is shown, that anions play a crucial role for the ionic structure of these flames. They bind free electrons and therefore change physical properties of the gas mixture which are usually dominated by the electrons. The electrical conductivity is an important example if one has in mind the applications mentioned above. But the distribution of the cations along the flames is altered by the anions, too, mostly caused by the properties of charged-species diffusion but also by ion-ion recombination reactions.

Detailed submodels are employed for the chemical and physical processes. Chemical reactions are treated on an elementary level by a reaction mechanism. Species diffusion and the heat conductivity of the gas mixture are calculated by the Chapman-Enskog theory, which is based on a molecular description of the individual species collisions. In contrast to the other simulations of ions in flames in the literature, this detailed diffusion model also includes the ion collisions. The process of ambipolar diffusion, which guarantees local charge neutrality, is directly incorporated into the model equations so that no additional partial differential equation for the electric field has to be solved.

The simulation of species profiles in a flat premixed flame serves as a sensitive test case for the reaction mechanism, which is set up in this thesis. The network of reactions is critically evaluated, and the resulting species profiles are compared to experimental data. In this work, kinetic data for elementary reactions are collected from the literature. It is tried to base the reaction mechanism as far as possible on measured reaction rates. In the literature, many reactions among charged species have been discussed qualitatively. Now, the numerical simulation enables a quantitative discussion of the suggested reactions. Within the framework of the reaction mechanism established, it is analyzed which pathways the chemical reactions take.

In addition to setting up a reaction mechanism, the second focus in this thesis is the formulation of a general method to deal with charged species diffusion in the flame. This is especially necessary for the inclusion of negative ions. In general, regions in the flame will exist where electrons are bound as negative ions. In this case, approaches are not valid anymore which rely on the assumption that the electrons dominate the diffusion processes with their high mobility. In addition, simple expressions for effective ambipolar diffusion coefficients cannot be found anymore. The equations derived in this thesis give a simple and intuitive picture of ambipolar diffusion. If the electron concentration is not too low, it is shown, that they still dominate the diffusion process, and expressions are found for this limit.

The new model of charged species diffusion is used in the simulations of the

laminar premixed flame. Its influence on the species profiles is discussed.

Finally, a main part of the work is devoted to the collection of the input data, which has to be provided for the simulations. This includes kinetic rate coefficients for the chemical reactions, thermodynamic properties, and molecular data from which the diffusion coefficients of the species are calculated. General sources of this information are given. In the case of lacking data, the information needed is estimated, and the influence of the respective uncertainties on the simulation results is discussed.

Chapter 2

Survey of the methodology used

This chapter will introduce the methodology used in this work to study charged species in premixed laminar flames. It provides the model equations, and all necessary material properties are introduced. Finally, it is shown how the reaction rates are obtained. This work uses methodologies of reactive flow simulations [WMD97] and also methodologies of plasma physics, see for instance [FK04].

The gas mixture is described by means of its density ρ, the local flow velocity v, the temperature T, and the mixture composition. Mass fractions Y_i are used in this work. The mass fraction of a species i is the ratio of its mass in the mixture m_i to the total mass. The mole fraction, instead, is the number of moles of the species n_i compared to the total number of moles in the system. Especially if the conservation of charge is discussed, the use of mole fractions is advantageous, because they reflect the number of particles instead of their mass which is most significant for the electrons:

$$Y_i = \frac{m_i}{\sum_j m_j} \qquad \text{and} \qquad X_i = \frac{n_i}{\sum_j n_j} \quad . \tag{2.1}$$

The concentrations c_i of the species can be calculated from the density, the pressure, the temperature, and the mole or mass fractions by the ideal gas law. For the conversion of mole and mass fractions the molar masses M_i and the mean molar mass of the gas mixture $\overline{M}$ are needed; R is the gas constant:

$$c_i = Y_i \frac{\overline{M}}{M_i} \frac{p}{RT} = X_i \frac{p}{RT} \quad . \tag{2.2}$$

To quantify the stoichiometry of the combustion process, the ratio of fuel to oxidizer is given as the equivalence ratio Φ:

$$\Phi = \frac{X_{\text{fuel}}/X_{\text{oxidizer}}}{\left(X_{\text{fuel}}/X_{\text{oxidizer}}\right)_{\text{st}}} \quad . \tag{2.3}$$

The subscript "st" stands for the ratio of a stoichiometric mixture, i. e., a mixture with the exact amount of fuel and oxidizer for a complete conversion to H_2O and CO_2 only.

2.1 MIXFLAME

The simulation of species profiles in laminar premixed flat flames is accomplished with the program MIXFLAME [War78a, War78b]. Flat flames are burner-stabilized flames, where the diameter of the burner surface is big enough allowing to neglect edge effects when examining the spatial profiles of species perpendicular to the burner surface. In this case, a one-dimensional model can be applied for the simulations.

In this section, the model is described for the simulation of neutral species only. For the program extensions which had to be made to include charged species see Chapter 5.

The program is based on the solution of the instationary conservation equations of reactive flows to obtain the spatial profiles of the mass fractions and the temperature in the steady state. The following main assumptions are made:

- Local thermodynamic equilibrium exists.
- The ideal gas law is valid.
- There are no external forces acting on the flame.
- The pressure is constant throughout the flame.
- Energy loss and transfer due to radiation can be neglected.

For the chemical processes and the transport phenomena, detailed submodels are applied.

2.1.1 Equations describing the fluid motion

In the following, the conservation equations of the total mass, the individual species masses, and the enthalpy – respectively temperature – in one spatial dimension are shown. These equations, together with the state law of an ideal gas, constitute the set of equations which are solved numerically.

For a gas of density ρ and flow velocity v the mass continuity equation in the steady state reads

$$\frac{\partial(\rho v)}{\partial x} = 0 \quad , \tag{2.4}$$

where x is the spatial coordinate. With a given flow velocity and gas composition at the burner surface, the flow velocity in each point in the flame can be calculated from the mass fractions of the species. For the mass fractions Y_i and the temperature T, the instationary conservation equations are solved until the stationary solution is reached. For the mass fractions they read

$$\rho\frac{\partial Y_i}{\partial t} + \rho v\frac{\partial Y_i}{\partial x} + \frac{\partial j_i}{\partial x} = r_i \quad . \tag{2.5}$$

The diffusion fluxes j_i are calculated from the gradient in the mass fraction and a mixture-composition and temperature-dependent diffusion coefficient D_i by Fick's law,

$$j_i = -D_i\rho\frac{\partial Y_i}{\partial x} \quad . \tag{2.6}$$

The chemical source term r_i depends on the mixture composition and the temperature as described in Section 2.2.

For the calculation of the temperature, the heat flux due to the diffusion of the species j_H, the heat conductivity λ, the heat capacity of the gas c_p, and the enthalpies of the species h_i are required. They are obtained from thermodynamic and transport properties databases, see the Sections 2.4 and 2.5:

$$\rho\frac{\partial T}{\partial t} + (\rho v + j_\mathrm{H})\frac{\partial T}{\partial x} - \frac{1}{c_p}\frac{\partial}{\partial x}\left(\lambda\frac{\partial T}{\partial x}\right) = -\frac{1}{c_p}\sum_i r_i h_i \quad . \tag{2.7}$$

The diffusion fluxes of the species are weighted by their heat capacities for the calculation of j_H,

$$j_\mathrm{H} = \frac{1}{c_p}\sum_i c_{p,i}\, j_i \quad . \tag{2.8}$$

Finally, the ideal gas law relates temperature, pressure, density and mixture composition:

$$p = \rho\sum_i \frac{Y_i}{M_i}RT \quad . \tag{2.9}$$

2.1.2 Numerical aspects

It is convenient, not to use the real spatial coordinate x as independent variable, but instead a dimensionless variable ϕ, which is given by the following transformation:

$$\phi = \frac{\psi}{\psi_\mathrm{h} - \psi_\mathrm{c}} \qquad \text{with} \qquad \frac{\partial\psi}{\partial x} = \rho \quad . \tag{2.10}$$

The parameters ψ_c and ψ_h for the cold and hot side of the flame are chosen widely enough, so that the coordinate system contains the flame entirely. After

this transformation the partial differential equations are obtained in the following standard forms:

$$\frac{\partial Y_i}{\partial t} = A\frac{\partial}{\partial \phi}\left(B_i\frac{\partial Y_i}{\partial \phi}\right) + C\frac{\partial Y_i}{\partial \phi} + D_i \tag{2.11}$$

$$\frac{\partial T}{\partial t} = \tilde{A}\frac{\partial}{\partial \phi}\left(\tilde{B}\frac{\partial T}{\partial \phi}\right) + \tilde{C}\frac{\partial T}{\partial \phi} + \tilde{D} \tag{2.12}$$

with the following six coefficients:

$$\begin{aligned} A &= -\frac{1}{\psi_\mathrm{h} - \psi_\mathrm{c}} & \tilde{A} &= \frac{1}{c_p(\psi_\mathrm{h} - \psi_\mathrm{c})} \\ B_i &= -\frac{D_i\rho^2}{\psi_\mathrm{h} - \psi_\mathrm{c}} & \tilde{B} &= \frac{\lambda\rho}{\psi_\mathrm{h} - \psi_\mathrm{c}} \\ C &= -\frac{\rho v}{\psi_\mathrm{h} - \psi_\mathrm{c}} & \tilde{C} &= -\frac{\rho v + j_\mathrm{H}}{\psi_\mathrm{h} - \psi_\mathrm{c}} \\ D_i &= \frac{r_i}{\rho} & \tilde{D} &= -\frac{1}{\rho c_p}\sum_i h_i r_i \quad . \end{aligned}$$

The derivatives with respect to ϕ are expressed as central differences, while for the time derivatives forward differences are used. Because of the stiffness mainly caused by the chemical source terms an implicit solution method is used. For this purpose, the chemical source term is linearized,

$$D_i^{(t+\Delta t)} = D_i^{(t)} + \left(\frac{\partial D_i^{(t)}}{\partial Y_i}\right)\left[Y_i^{(t+\Delta t)} - Y_i^{(t)}\right] \quad . \tag{2.13}$$

Apart from this implicit treatment, all other terms on the right hand side of the equation are taken at the time t. This leads to a linear system of equations for the unknown variables at time $t + \Delta t$. On the cold boundary of the flame, the temperature of the unburnt gas and its composition are imposed as boundary conditions, while at the hot boundary vanishing gradients are demanded:

$$\frac{\partial Y_i^\mathrm{h}}{\partial \phi} = 0 \qquad \text{and} \qquad \frac{\partial T^\mathrm{h}}{\partial \phi} = 0 \quad . \tag{2.14}$$

To save computing time, the system of partial differential equations is not solved simultaneously, but sequentially at a given time t for the mass fractions and temperature. The error involved in this approach vanishes, when the stationary solution is reached.

2.2 Reaction kinetics

The chemical processes in the flame are modeled in a detailed way by the use of a set of elementary reactions. These reactions – in contrast to global reactions – are supposed to be actually proceeding in the gas phase on a molecular level. This permits to establish a rate law for each reaction in an easy way since the order of a reaction in this case is equal to its molecularity. All reactions are considered to be reversible. The rates of all backward reactions are calculated from the forward rates by the use of the thermodynamic equilibrium constants.

A general chemical reaction reads as follows, where S_i are the species symbols, ν_{ir}^{e} and ν_{ir}^{p} are the stoichiometries of the educts and products for reaction r respectively:

$$\sum_i \nu_{ir}^{\mathrm{e}} S_i \rightharpoonup \sum_i \nu_{ir}^{\mathrm{p}} S_i \quad . \tag{2.15}$$

The total rate of production or consumption of a species r_i results from the sum over the rates of all reactions including backward reactions,

$$r_i = \left(\frac{\partial c_i}{\partial t}\right)_{\mathrm{chem}} = \sum_r \left(\nu_{ir}^{\mathrm{p}} - \nu_{ir}^{\mathrm{e}}\right) k_r(T) \prod_j c_j^{\nu_{jr}^{\mathrm{e}}} \quad . \tag{2.16}$$

The c_i denote the species concentrations. The modified Arrhenius law is applied for the temperature-dependent reaction coefficients k_r:

$$k_r(T) = A_r T^{n_r} \exp\left(-\frac{E_{\mathrm{a},r}}{RT}\right) \quad . \tag{2.17}$$

The three parameters A_r, n_r, and the activation energy $E_{\mathrm{a},r}$ are provided for all forward reactions in a database. The concentrations are easily obtained from the mass fractions Y_i, which are used as variables in the simulations. The ideal gas law, together with the molar masses M_i are needed for this:

$$c_i = c\frac{\overline{M}}{M_i} Y_i \qquad \text{with} \qquad \overline{M} = \left(\sum_i \frac{Y_i}{M_i}\right)^{-1} \quad , \quad c = \frac{p}{RT} \quad . \tag{2.18}$$

The rate coefficients for the backward reactions k_r^{-1} are calculated from the thermodynamic equilibrium constants $K_{c,r}$,

$$k_r^{-1}(T) = \frac{1}{K_{c,r}(T)} \cdot k_r(T) \quad . \tag{2.19}$$

These constants can be obtained from the standard molar free reaction enthalpies $\Delta_r \overline{G}^0$ at standard pressure p_0 of one atmosphere:

$$K_{c,r}(T) = \left(\frac{p_0}{RT}\right)^{\sum_i \nu_{ir}^{\mathrm{p}} - \nu_{ir}^{\mathrm{e}}} \cdot \exp\left(-\frac{\Delta_r \overline{G}^0(T)}{RT}\right) \quad . \tag{2.20}$$

The free reaction enthalpies can be calculated from the standard values of the molar reaction enthalpies $\Delta_r\overline{H}^0$ and entropies $\Delta_r\overline{S}^0$:

$$\Delta_r\overline{G}^0(T) = \Delta_r\overline{H}^0(T) - T\Delta_r\overline{S}^0(T) \quad . \tag{2.21}$$

These values can be obtained from the molar enthalpies $\overline{H}^0$ and entropies $\overline{S}^0$ of the species participating in the reaction at standard pressure. These values are provided in a database as described in Section 2.4,

$$\Delta_r\overline{H}^0(T) = \sum_i (\nu_{ir}^{\mathrm{p}} - \nu_{ir}^{\mathrm{e}})\,\overline{H}_i^0(T) \qquad \text{and} \qquad \Delta_r\overline{S}^0(T) = \sum_i (\nu_{ir}^{\mathrm{p}} - \nu_{ir}^{\mathrm{e}})\,\overline{S}_i^0(T) \quad .$$

For some reactions, one species serves as a so-called third body which is left unchanged in the reaction. Most of the neutral species with high concentrations can be effective third bodies. These different third bodies are represented by the symbol M in the reaction mechanism. The rates for the single reactions are calculated from the common Arrhenius expression and multiplied by the third body efficiencies which are part of the reaction mechanism. Four different sets of third bodies are used and are denoted by M(1), ... , M(4).

Some reactions appear twice in the reaction mechanism due to strong non-Arrhenius behavior. In this case the final kinetic rate is the sum of both kinetic rates following the Arrhenius law expressions.

Finally, there are pressure-dependent reactions in the mechanism of the neutral species. Here, the rate coefficient depends on the gas pressure and is calculated as described in [Kar].

2.3 Reaction flow analysis

A general reaction mechanism can consist of hundreds of species and thousands of reactions. Information about the behavior of this network of reactions can be gained for individual situations by reaction flow analysis. In such an analysis, the contribution of each reaction to the production and consumption of a species is evaluated. Starting from this information, a global scheme can be developed which shows the pathways by which a species is produced or consumed. The reaction flow depends on the choice of parameters for the system, like temperature, pressure, and mixture composition.

In this work, only global reaction flow analyses are presented which are done in the following way: For the stationary flames the local reaction rates $r_{i,r}$ for the species i of each individual reaction r are integrated along the flame:

$$\begin{aligned} r_{i,r}^{+} &= \int \Theta(r_{i,r})|r_{i,r}(\phi)|\,\mathrm{d}\phi \\ r_{i,r}^{-} &= \int \Theta(-r_{i,r})|r_{i,r}(\phi)|\,\mathrm{d}\phi \quad . \end{aligned}$$

The Θ-function is used so that the integration is only carried out over regions where the reaction rate has the same sign. In this way, the contribution of each reaction to the production R^+ respectively consumption R^- of a species can be obtained from the integrated rates $r^\pm$:

$$R_{i,r}^{\pm} = \frac{r_{i,r}^{\pm}}{\sum_r r_{i,r}^{\pm}} \quad . \tag{2.22}$$

It was found to be advantageous not to treat the forward and respective backward reactions as independent reactions in the analysis. Instead, their kinetic rates are added before they are integrated along the flame and regarded as a single reaction. In this way, the global contribution of a reaction to the production and consumption of a species is obtained.

2.4 Thermodynamic properties

In the partial differential equation 2.7 for the gas temperature, the heat capacity of the gas mixture as well as the enthalpies of all species are needed. Moreover, the heat capacities are required to calculate the heat conductivity. In addition, the entropies of all species are used to calculate the reaction rates of the backward reactions, see Section 2.2. This thermodynamic information is provided for each species in a database as described in this section.

In systems with constant pressure and valid ideal gas law, the molar enthalpy $\overline{H}$ and entropy $\overline{S}$ of each species can be calculated from its temperature dependent heat capacity $\overline{C}_p$:

$$\overline{H}(T) = \overline{H}_0 + \int_{T_0}^{T} \overline{C}_p(T')\,\mathrm{d}T' \tag{2.23}$$

$$\overline{S}(T) = \overline{S}_0 + \int_{T_0}^{T} \frac{\overline{C}_p(T')}{T'}\,\mathrm{d}T' \quad . \tag{2.24}$$

Here, the subscript "0" denotes standard conditions, which is 298.15 Kelvin and a pressure of one atmosphere. The heat capacities are given as fourth order polynomials together with the two integration constants at standard conditions $\overline{H}_0$ and $\overline{S}_0$, following the standard NASA formulation [GM71]. These seven parameters a_1, a_2, ... , a_7 are given for two temperature ranges to fit the exact data better. From these coefficients, the heat capacities, enthalpies and entropies of all species can be calculated in the following way:

$$\frac{\overline{C}_p}{R} = a_1 + a_2 T + a_3 T^2 + a_4 T^3 + a_5 T^4$$

$$\begin{aligned}\frac{\overline{H}}{R} &= a_1 T + \frac{a_2}{2}T^2 + \frac{a_3}{3}T^3 + \frac{a_4}{4}T^4 + \frac{a_5}{5}T^5 + a_6 \\ \frac{\overline{S}}{R} &= a_1 \ln T + a_2 T + \frac{a_3}{2}T^2 + \frac{a_4}{3}T^3 + \frac{a_5}{4}T^4 + a_7 \quad .\end{aligned}$$

Here R is the gas constant. There is a new standard of the NASA format which extends the previous one in allowing for more than two temperature ranges and the inclusion of T^{-1} and T^{-2} terms in the fit function for the heat capacities [MG96]. This yields the following expressions for the needed thermodynamic properties:

$$\begin{aligned}\frac{\overline{C}_p}{R} &= a_1 T^{-2} + a_2 T^{-1} + a_3 + a_4 T + a_5 T^2 + a_6 T^3 + a_7 T^4 \\ \frac{\overline{H}}{R} &= -a_1 T^{-1} + a_2 \ln T + a_3 T + \frac{a_4}{2}T^2 + \frac{a_5}{3}T^3 + \frac{a_6}{4}T^4 + \frac{a_7}{5}T^5 + a_8 \\ \frac{\overline{S}}{R} &= -\frac{a_1}{2}T^{-2} - a_2 T^{-1} + a_3 \ln T + a_4 T + \frac{a_5}{2}T^2 + \frac{a_6}{3}T^3 + \frac{a_7}{4}T^4 + a_9 \quad .\end{aligned}$$

With this information, the heat capacity of the gas mixture can be calculated as an average weighted by the mass fractions Y_i,

$$c_p = \sum_i Y_i \frac{\overline{C}_{p,i}}{M_i} \quad . \tag{2.25}$$

2.5 Transport processes

The local properties of a gas mixture do not change solely because of convection and chemical production respectively consumption processes. Inhomogeneities in these properties lead to transport processes which tend to equalize the spatial variations. Fluxes of particles (diffusion), energy (heat conduction) and momentum result.

In this work, the Chapman-Enskog theory for dilute gases is used to calculate the transport processes [CC94, HCB64, BSL02]. Its key assumptions are the existence of local thermodynamic equilibrium and the dominance of two-particle interactions. Therefore, it can only be applied to partially ionized gases and not too high external electric fields. These conditions are fullfilled for the systems considered in this thesis.

Previous work led to a software library for the calculation of transport coefficients in reactive and partially ionized flows. This TRAPLA library is used to calculate the species diffusion coefficients and the heat conductivity inside the methane-oxygen flame. Details of the transport model and the library can be

Parameter	Neutral species	Charged species
Lennard-Jones parameters (ϵ, σ)	×	
Dipole (q)	×	
Dipole polarizability (α)	×	×
Quadrupole polarizability (α_{q})	×	
Dispersion coefficient (C_6)	×	×
Rotational collision number (Z_{rot})	×	×
Stockmayer parameter (n)		×
Resonant charge transfer (A_{rct}, B_{rct})		×

Table 2.1: Parameters of the heavy species required to calculate the transport coefficients.

found in [Sel02, SRW98, SR99]. It has been proven that it delivers very good results for the prediction of the transport properties of air in the temperature range from 300 K to 30000 K.

The Chapman-Enskog theory is based on the individual interaction potentials between all possible pairs of species. It offers a detailed description of macroscopic transport processes with the need for little input data only. Table 2.1 shows all parameters of the charged and neutral species which are needed to calculate the transport coefficients. The electrons have to be treated differently as described later.

As input data, the Lennard-Jones (ϵ, σ) and Stockmayer (n) potential parameters, the permanent dipoles (q), the dipole and quadrupole polarizabilities (α, α_{q}), a dispersion coefficient (C_6), the rotational collision number (Z_{rot}), and fit parameters for resonant charge transfer processes (A_{rct}, B_{rct}) have to be provided.

The following interaction potentials are used, depending on the nature of the colliding species. The potentials are orientation-averaged, so that they only depend on the distance r of both species i and j. The library offers a correction of the interaction potentials for high collision energies by the Born-Mayer potential, which is not used in this work, because it does not contribute significantly at the relatively low temperatures in the flames studied here.

2.5.1 Collision between two uncharged species

The Stockmayer potential represents the collision of two uncharged species,

$$\phi(r)_{\mathrm{St}} = 4\epsilon_{ij}\left[\left(\frac{\sigma_{ij}}{r}\right)^{12} - \left(\frac{\sigma_{ij}}{r}\right)^{6} + \delta_{ij}\left(\frac{\sigma_{ij}}{r}\right)^{3}\right] \quad . \tag{2.26}$$

For calculating the three parameters ϵ, σ, and δ, combination rules are applied, which combine the corresponding parameters for gases of the pure species:

$$\begin{aligned} \sigma_{ij} &= \frac{1}{2}(\sigma_i + \sigma_j)\xi_{ij}^{-1/6} \\ \epsilon_{ij} &= \sqrt{\epsilon_i \epsilon_j}\xi_{ij}^2 \quad . \end{aligned}$$

If both species are polar or both species have no permanent dipole, then

$$\xi_{ij} = 1 \qquad \text{and} \qquad \delta_{ij} = \frac{1}{4}\frac{q_i q_j}{\epsilon_{ij}\sigma_{ij}^3} \quad .$$

Else, if only the species j is polar, then the following expressions are valid for ξ and δ:

$$\xi_{ij} = 1 + \frac{1}{4}\left(\frac{\alpha_i}{\sigma_i^3}\right)\left(\frac{q_j^2}{\epsilon_j \sigma_j^3}\right)\sqrt{\frac{\epsilon_j}{\epsilon_i}} \qquad \text{and} \qquad \delta_{ij} = \frac{1}{4}\frac{q_j^2}{\epsilon_{ij}\sigma_{ij}^3} \quad .$$

2.5.2 Collision between a charged and a neutral species

The interaction potential between a charged species i and a neutral species j is described by the (n,6,4)-potential:

$$\begin{aligned} \phi(r)_{n,6,4} &= \frac{n_i \epsilon_{ij}}{n_i(3+\gamma_{ij}) - 12(1+\gamma_{ij})} \\ &\cdot \quad \left[\frac{12}{n_i}(1+\gamma_{ij})\left(\frac{\sigma_{ij}}{r}\right)^{n_i} - 4\gamma_{ij}\left(\frac{\sigma_{ij}}{r}\right)^6 - 3(1-\gamma_{ij})\left(\frac{\sigma_{ij}}{r}\right)^4\right] \quad . \end{aligned}$$

Here, σ and ϵ represent the position and depth of the minimum of the interaction potential respectively. They are estimated, based on the polarizabilities of both species. $K_1 = 1.767$, $K_2 = 0.72$, and $\kappa = 0.095$ are used as constants,

$$\sigma_{ij} = K_1 \frac{\alpha_i^{1/3} + \alpha_j^{1/3}}{[\alpha_i \alpha_j (1 + 1/\xi_{ij})]^\kappa} \qquad \text{and} \qquad \epsilon_{ij} = K_2 \frac{\alpha_j Z_i^2 e^2}{8\pi\epsilon_0 \sigma_{ij}^4}(1+\xi_{ij})$$

$$\xi_{ij} = \frac{\alpha_i}{Z_i^2\left[1 + (2\alpha_i/\alpha_j)^{2/3}\right]\alpha_j^{1/2}} \quad .$$

The remaining parameter γ is calculated again by a combination rule from the polarizabilities and dispersion coefficients of both species and the quadrupole polarizability of the neutral species:

$$\gamma_{ij} = \frac{(2/Z_i^2)(C_{6,ij}/e^2) + \alpha_{\mathrm{q},j}}{\alpha_j \sigma_{ij}^2} \qquad \text{with} \qquad C_{6,ij} = \frac{2C_{6,i}C_{6,j}}{(\alpha_j/\alpha_i)C_{6,i} + (\alpha_i/\alpha_j)C_{6,j}} \quad .$$

A special case is the collision of an ion with its uncharged counterpart. In this situation, the interaction between both species is increased by resonant charge transfer. This quantum mechanical effect is not accounted for in the interaction potential, but will lead to a correction term in the collision cross sections, see Section 2.5.6.

2.5.3 Collision between two charged species

Finally, the Debye-Hückel potential models the interaction between two charged species. This also includes the electrons,

$$\phi(r)_{\mathrm{DH}} = \frac{Z_i Z_j e^2}{4\pi\epsilon_0 r} \exp(-r/\lambda_{\mathrm{D}}) \quad . \tag{2.27}$$

It only depends on the charges of the species $Z_i e$ and the Debye length λ_{D}, which gives the length scale on which the strong Coulomb interaction is screened by species of the opposite charge. Usually, the Debye length is expressed in terms of the electron number density n_{e} only, because in gases without other negatively charged species they represent the main charge carriers. In this work, the electrons can attach to neutral species, so that the number densities of all charged species n_i have to be accounted for to calculate the Debye length:

$$\lambda_{\mathrm{D}} = \sqrt{\frac{\epsilon_0 kT}{e^2 \sum_i n_i Z_i^2}} = \sqrt{\frac{\epsilon_0 kT}{e^2 N_{\mathrm{A}} \rho \sum_i Y_i Z_i^2 / M_i}} \quad . \tag{2.28}$$

The latter formula expresses the number densities in terms of the mass fractions Y_i which are used as variables in the simulations. M_i are the molar masses and N_{A} is the Avogadro constant. The Debye length is chosen as the collision cross section in a hard-sphere model, $\sigma_{ij} = \lambda_{\mathrm{D}}$, see Equation 2.35.

2.5.4 Collision between electrons and neutral species

The scattering of electrons from neutral species cannot be calculated in a semi-classical way by interaction potentials. Especially at the low electron energies present in flames, quantum mechanical effects are important. For this reason, differential collision cross sections for elastic scattering or transport collision integrals are needed for each single collision.

The differential elastic collision cross section $q_{\mathrm{e}j}(E, \chi)$ gives the probability to find the electron of incident energy E at a scattering angle χ after the collision with species j. An integration leads to the transport cross sections $Q^{(l)}$,

$$Q^{(l)}_{\mathrm{e}j}(E) = 2\pi \int_0^{\pi} q_{\mathrm{e}j}(E, \chi) \left(1 - \cos^l \chi\right) \sin\chi \, \mathrm{d}\chi \quad . \tag{2.29}$$

2.5.5 Reduced collision integrals

Reduced collision integrals $\Omega^{(l,s)*}$ are temperature-dependent functions which describe the difference of the collision between all species pairs i and j compared to the hard-sphere-model. The superscripts l and s stem from the perturbation theory used by Chapman and Enskog,

$$\Omega_{ij}{}^{(l,s)*}(T) = \frac{1}{(s+1)!}\frac{\sqrt{\pi}}{2}\frac{1}{(kT)^{s+1/2}}\int_0^\infty E^{s+1/2}Q_{ij}^{(l)*}(E)f(E)\,\mathrm{d}E \quad . \tag{2.30}$$

The averaging over collision energies is done using the Maxwell distribution function expressed in terms of the kinetic energy E of the gas species,

$$f(E)\,\mathrm{d}E = \frac{2}{\sqrt{\pi}}(kT)^{-3/2}\sqrt{E}\,e^{-E/(kT)}\,\mathrm{d}E \quad . \tag{2.31}$$

The transport cross sections $Q_{ij}^{(l)}$ can be calculated from the interaction potentials by classical theory,

$$Q_{ij}^{(l)}(E) = 2\pi\int_0^\infty \Big(1-\cos^l\chi(E,b)\Big)\,b\,\mathrm{d}b \quad . \tag{2.32}$$

Here, χ is the scattering angle after the collision and b is the impact parameter. Finally, the reduced collision cross sections $Q^{(l)*}$ are normalized to yield $\Omega_{ij}{}^{(l,s)*} = 1$ for the hard-sphere model,

$$Q_{ij}^{(l)*} = \frac{1}{\pi\sigma_{ij}^2}\left[1-\frac{1}{2}\frac{1+(-1)^l}{1+l}\right]^{-1}Q_{ij}^{(l)} \quad . \tag{2.33}$$

For the higher orders of the collision integrals with respect to s, the following recursion formula is applied:

$$\Omega^{(l,s+1)*} = \Omega^{(l,s)*} + \frac{T}{s+2}\frac{\mathrm{d}\Omega^{(l,s)*}}{\mathrm{d}T} \quad . \tag{2.34}$$

2.5.6 Resonant charge transfer

The collision of a neutral species A with its charged counterpart $\mathrm{A}^\pm$ is altered by the quantum mechanical process of resonant charge transfer,

$$\mathrm{A} + \mathrm{A}^\pm \rightharpoonup \mathrm{A}^\pm + \mathrm{A} \quad .$$

This changes the collision cross sections for odd parameters l, leading to a reduced binary diffusion coefficient. The energy dependence of the correction is fitted by two parameters A and B for each resonant charge transfer process respectively:

$$\begin{aligned} Q_{\mathrm{corr}}^{(1)}(E) &= Q^{(1)}(E) + 2Q_{\mathrm{rct}}(E) \\ \sqrt{Q_{\mathrm{rct}}(E)} &= A_{\mathrm{rct}} - B_{\mathrm{rct}}\ln\left(E/k\right) \quad . \end{aligned}$$

2.6 Transport coefficients of binary or pure gas mixtures

The binary diffusion coefficients D_{ij} depend on the temperature and the pressure. They are calculated from the momentum transfer ("diffusion") collision integrals $\Omega_{ij}^{(1,1)*}$ and the reduced molar masses M_{ij},

$$D_{ij} = \frac{3}{8}\frac{\sqrt{\pi N_{\mathrm{A}}(kT)^3/M_{ij}}}{\pi\sigma_{ij}^2 p\Omega_{ij}^{(1,1)*}} \qquad \text{with} \qquad M_{ij} = \frac{2M_iM_j}{M_i+M_j} \quad . \tag{2.35}$$

The viscosity η_i of a pure gas of species i is calculated from the collision integral $\Omega_{ii}^{(2,2)*}$,

$$\eta_i = \frac{5}{16}\frac{\sqrt{M_i kT/(\pi N_{\mathrm{A}})}}{\sigma_{ii}^2\Omega_{ii}^{(2,2)*}} \quad . \tag{2.36}$$

Finally, the heat conductivity λ_i of a gas of species i is obtained in the following way:

$$\lambda_i = \frac{\eta_i}{M_i}(f_{\mathrm{trans}}\overline{C}_{V,\mathrm{trans}} + f_{\mathrm{rot}}\overline{C}_{V,\mathrm{rot}} + f_{\mathrm{vib}}\overline{C}_{V,\mathrm{vib}}) \quad . \tag{2.37}$$

The contributions of translational, rotational and vibrational degrees of freedom to the heat conductivity are calculated from the respective molar heat capacities at constant volume $\overline{C}_V$,

$$\begin{aligned} \overline{C}_{V,\mathrm{trans}} &= \frac{3}{2}R \quad , \quad \overline{C}_{V,\mathrm{vib}} = \overline{C}_p - R - \overline{C}_{V,\mathrm{trans}} - \overline{C}_{V,\mathrm{rot}} \\ \overline{C}_{V,\mathrm{rot}} &= \frac{F}{2}R \qquad \text{with} \qquad F = \begin{cases} 0 & : \text{ atoms} \\ 2 & : \text{ linear molecules} \\ 3 & : \text{ non-linear molecules} \end{cases} , \end{aligned}$$

and correction factors f,

$$\begin{aligned} f_{\mathrm{trans}} &= \frac{5}{2}\left(1 - \frac{2}{\pi}\frac{\overline{C}_{V,\mathrm{rot}}}{\overline{C}_{V,\mathrm{trans}}}\Delta_{\mathrm{rot}}\right) \\ f_{\mathrm{rot}} &= \frac{6}{5}A^*\left(1 + \frac{2}{\pi}\Delta_{\mathrm{rot}}\right) \\ f_{\mathrm{vib}} &= \frac{6}{5}A^* \end{aligned}$$

with

$$A^* = \frac{\Omega^{(2,2)*}}{\Omega^{(1,1)*}} \quad \text{and} \quad \Delta_{\mathrm{rot}} = \left(\frac{5}{2} - \frac{6}{5}A^*\right)\left[Z_{\mathrm{rot}}(T) + \frac{2}{\pi}\left(\frac{5}{3}\frac{\overline{C}_{V,\mathrm{rot}}}{R} + \frac{6}{5}A^*\right)\right]^{-1} \quad .$$

The rotational collision number at temperature T is obtained from its value at 298 K, which has to be provided as input data, and a function $\zeta(T)$:

$$Z_{\mathrm{rot}}(T) = Z_{\mathrm{rot}} \frac{\zeta(298K)}{\zeta(T)} \quad .$$

Higher orders of the perturbation theory of Chapman and Enskog are used for the self-diffusion coefficient of the electrons D_{ee} and their contribution to the heat conductivity. This requires higher orders of the collision integrals concerning electrons with respect to the index s. They are calculated by Equation 2.34. Details of the TRAPLA transport model can be found in [Sel02].

2.6.1 Transport coefficients of a gas mixture

Empirical formulas are used to calculate the transport coefficients for a gas mixture of different species from the respective coefficients of pure or binary gases. This procedure is less accurate compared to a detailed multi-component formulation of the transport coefficients, but numerically much less demanding in terms of computation time. The accuracy which is achieved by the empirical formulas is sufficient for the purpose of this work, because the ion concentrations are not very sensitive to the diffusion coefficients, as shown in Section 5.4.

The diffusion flux j_i of species i is caused by a gradient in its mass fraction Y_i. With the help of the effective diffusion coefficient D_i of species i in the gas mixture, the following expression is used:

$$j_i = -D_i \rho \frac{\partial Y_i}{\partial x} \quad . \tag{2.38}$$

The effective diffusion coefficient is calculated from the binary diffusion coefficients:

$$D_i = \frac{1 - Y_i}{\sum_{j \neq i} X_j / D_{ij}} \quad . \tag{2.39}$$

Also the heat conductivity of the gas mixture λ is calculated from the heat conductivities of the pure gases weighted by the mole fractions of the species X_i,

$$\lambda = \frac{1}{2} \left[\sum_i X_i \lambda_i + \left(\sum_i \frac{X_i}{\lambda_i} \right)^{-1} \right] \quad . \tag{2.40}$$

The viscosity η of the gas mixture can be calculated in the same way as the heat conductivity in Equation 2.40. In this work it is not needed, because no momentum conservation equation has to be solved, see Section 2.1.

Chapter 3

Model data

This chapter documents the origin of all necessary input data which has to be provided for the simulations. First of all, this consists of an elementary reaction mechanism which contains the reaction paths and the kinetic data of all reactions. Secondly, the thermodynamic information of all species has to be provided. Therefore, the temperature-dependent heat capacities, enthalpies and entropies are needed. Finally, a number of parameters is required for each species to calculate the interaction potentials of all species pairs. With this information the transport properties of the gas mixture can be evaluated, i. e., diffusion coefficients and the heat conductivity are obtained. All data used in the simulations can be found in the appendix.

3.1 Reaction mechanism

The collection of reactions and the corresponding kinetic data is based on a reaction mechanism for the combustion of lean to stoichiometric methane-air flames [Kar]. This mechanism consists of 208 reactions involving 38 neutral species. Charged species are not included. This mechanism has proven to describe the occurring chemical processes very well. It has been validated with the aid of homogeneous systems like shock-tube experiments as well as one-dimensional systems like burner stabilized flat flames.

3.1.1 Sources of ion-chemistry data

The reactions concerning charged species are mainly taken from the literature. There are several main research areas in which kinetic data for ion-chemistry can be found. These are:

- Combustion research: Natural occurring ionization in different flames has been studied experimentally as well as theoretically. Hydrogen, methane, and acetylene – sometimes with additives of other hydrocarbons or metallic substances – as fuels have been investigated. Ionic species in homogeneous systems have been studied also. Moreover, the chemistry of discharge processes is a source of kinetic data.

- Plasma research: Reactions of charged species occur in a variety of low pressure plasma processes, like plasma etching.

- Atmospheric chemistry research: A number of species occur in some regions in the atmosphere which are also important for the ion chemistry in flames. This includes cations as well as anions.

- Interstellar chemistry research: Species like CHO^+ can also be found in the interstellar medium. Some of the reactions found there can also contribute to the chemistry in flames.

The environments for the chemical processes differ considerably in these research areas. The temperature and pressure varies over several orders of magnitude. Also, most of the reaction rates were measured at room temperature only. This leads to uncertainties concerning the temperature dependence of the reaction rates, having in mind the usual temperature range from 300 K up to about 2000 K in methane-oxygen flames. On the other hand, exothermic ion-neutral and ion-ion reactions are expected to be only slightly temperature-dependent, i. e., they have vanishing or very low activation energies.

3.1.2 Estimation of reaction rates

Measurements of rate coefficients exist for a number of reactions, but for some important pathways in methane-oxygen flames they are not available. In lack of data, the ADO theory is regularly used. This so-called "average-dipole-orientation" approach calculates the collision rates between an ion and a neutral species [SB73, SSB78]. For exothermic reactions, this collision rate is taken as the reaction rate, so that it is assumed that each collision leads to a reaction. This assumption has shown its validity in many cases. To calculate the collision rate, the charge Z of the ion, the reduced mass μ of the pair of species, the dipole polarizability α, and the permanent electric dipole q of the neutral species are needed:

$$k_{\mathrm{ADO}} = \frac{2\pi Z}{\sqrt{\mu}} \left[\sqrt{\alpha} + Cq\sqrt{\left(\frac{2}{\pi kT}\right)} \right] \quad . \tag{3.1}$$

Cations	Anions
H_3O^+, $C_2H_3O^+$, CH_5O^+, CHO^+	E^-, O_2^-, O^-, OH^-, CHO_2^-, CHO_3^-, CO_3^-

Table 3.1: Empirical formulas of the charged species which are included in the reaction mechanism.

The parameter C is a function of the ratio $q/\sqrt{\alpha}$ and has approximate values from 0.1 for small ratios to 0.3 for large ratios [SSB78]. The resulting collision rate coefficients are in the order of 10^{15} cm^3/(mol s) and show a slight decrease with temperature for polar neutral species.

3.1.3 List of charged species

The most abundant cations and anions which were observed in the experiments of Goodings et al. [GBN79a, GBN79b] are included in the model. In a lean methane-oxygen flame, three cations are responsible for more than 70% of the total charge in the cold region of the flame and for about 100% in the reaction zone and the burnt gas region. Six anions together with the electrons constitute almost completely the negative charges in this flame. In addition to these 10 species, CHO^+ is also included even though it appears only in low concentrations, because it is known to be the initial chemi-ion. Table 3.1 lists all ions as empirical formulas. Figure 3.1 shows the expected structures. The so-called cluster-ions CHO_3^- and CO_3^- are known from atmospheric chemistry. Despite this designation as cluster-ions, quantum mechanical calculations showed that they are bound in a classical chemical sense.

3.1.4 Cation chemistry

The cation chemistry in a methane flame has been subject to research for many years and is believed to be relatively well known [GBN79a, PB93]. Most of the major reactions were measured at least at room temperature. Besides the chemi-ionization reaction, proton transfer reactions dominate the cation chemistry. The proton affinities of the relevant neutral species are shown in Table 3.2. Finally, electron recombination and recombination with anions are the channels which remove the cations.

Table 3.3 shows the cation reactions in the mechanism used in this work. The references are cited and, if available, the temperature range and uncertainties of the rate coefficients are given. Most of the reactions can be found in several references. Here, the most recent ones or the references which give a temperature range and errors are shown.

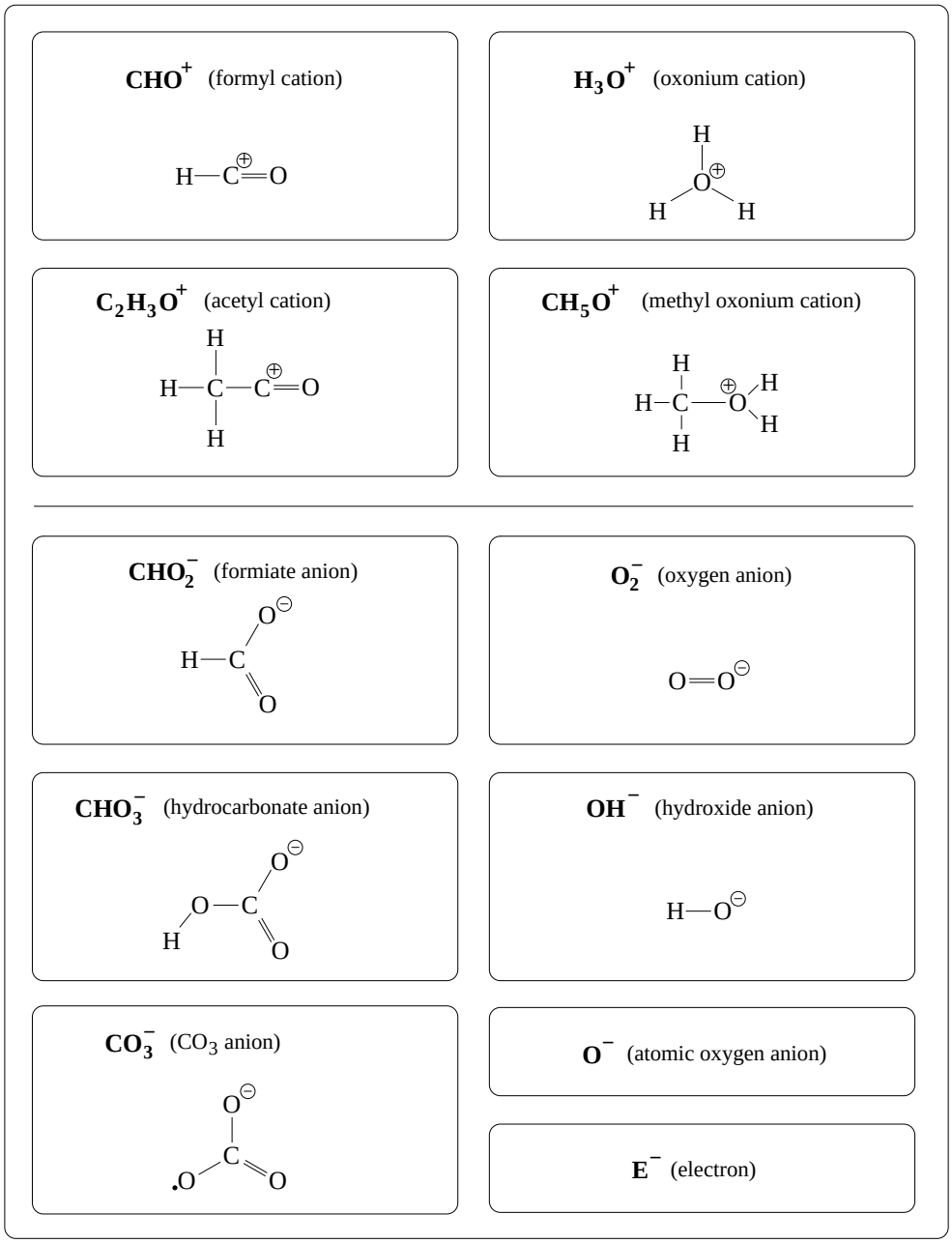

Figure 3.1: Empirical and structural formulas of the charged species in the reaction mechanism. Quantum mechanical calculations of these structures can be found in [Sch05].

Species	PA [kJ/mol]	Species	PA [kJ/mol]
CO	594.0	CH_2O	712.9
CH_3OH	754.3	C_2H_4	680.5
CH_2CO	825.3	CO_2	540.5
H_2O	691.0	CH_3CHO	768.5

Table 3.2: Proton affinities of some neutral species occurring in lean methane-oxygen flames. The data is taken from [HL98].

Chemi-ionization		Reference
$CH+O \rightleftharpoons CHO^+ + E^-$	10-1750 K	[TMM00]
Proton transfer reactions		
$CHO^+ + H_2O \rightleftharpoons H_3O^+ + CO$	10-41000 K, <25%	[TMM00]
$CHO^+ + CH_3OH \rightleftharpoons CH_5O^+ + CO$	10-41000 K, <25%	[TMM00]
$CHO^+ + CH_2CO \rightleftharpoons C_2H_3O^+ + CO$	10-41000 K, <25%	[TMM00]
$H_3O^+ + CH_2CO \rightleftharpoons C_2H_3O^+ + H_2O$	10-41000 K, <25%	[TMM00]
$H_3O^+ + CH_3OH \rightleftharpoons CH_5O^+ + H_2O$	10-41000 K, <25%	[TMM00]
$CH_5O^+ + CH_2CO \rightleftharpoons C_2H_3O^+ + CH_3OH$	-	-
Dissociative electron recombination		
$H_3O^+ + E^- \rightleftharpoons OH+H+H$	10-2400 K, <25%	[TMM00]
$H_3O^+ + E^- \rightleftharpoons H_2O+H$	10-1000 K, <25%	[TMM00]
$H_3O^+ + E^- \rightleftharpoons H_2+OH$	10-1000 K, <25%	[TMM00]
$H_3O^+ + E^- \rightleftharpoons O+H_2+H$	10-1000 K, <25%	[TMM00]
$CHO^+ + E^- \rightleftharpoons CO+H$	10-300 K, <25%	[TMM00]
$C_2H_3O^+ + E^- \rightleftharpoons CH_2CO+H$	10-300 K	[TMM00]
$C_2H_3O^+ + E^- \rightleftharpoons CO+CH_3$	10-300 K	[TMM00]
$CH_5O^+ + E^- \rightleftharpoons CH_3OH+H$	10-300 K	[TMM00]
Charge transfer with rearrangement		
$CHO^+ + CH_3 \rightleftharpoons C_2H_3O^+ + H$	-	[BE88]
$CHO^+ + C_2H_5OH \rightleftharpoons H_3O^+ + CO + C_2H_4$	300 K, 15%	[Ani03]
$H_3O^+ + C \rightleftharpoons CHO^+ + H_2$	10-41000 K, factor 2	[TMM00]
$C_2H_3O^+ + O \rightleftharpoons CHO^+ + CH_2O$	-	-

Table 3.3: Reactions involving the cations included in the reaction mechanism.

Three reactions were added to the mechanism for which no kinetic data could be found. The ADO theory is used for all of them to estimate the reaction rate coefficients. The first one is the proton transfer reaction from CH_5O^+ to produce $C_2H_3O^+$. It is included to complete the proton transfer reactions between the cations. The second reaction is the conversion of $C_2H_3O^+$ to CHO^+ by the oxygen radical,

$$C_2H_3O^+ + O \rightleftharpoons CHO^+ + CH_2O \quad . \tag{3.2}$$

Goodings et al. [GBN79a] suggested reactions like this with radicals like O, OH, and H. However, Reaction 3.2 is the only exothermic one leading to CHO^+. Finally, a third reaction was added which involves the ions CHO^+ and $C_2H_3O^+$. It was suggested by Brown et al. [BE88].

3.1.5 Anion chemistry

Even though many of the reactions between the anions in this model have been measured, the anion chemistry in flames is still not well understood. If uncertainties of the reaction rates are stated in the literature, they are much higher than in the case of cation reactions. It also has to be expected that reaction paths are still unknown. In the following Tables 3.4 and 3.5 the part of the reaction mechanism is shown which concerns the anions. If available, the uncertainty of the kinetic rate and the temperature range for which the rate has been obtained is given together with the reference.

Electron attachment to species with high electron affinity leads to the first anions. As third bodies, only the most abundant species in the lean methane-oxygen flame, O_2 and H_2O, have to be included. Electron affinities of the neutral species leading to the anions in the mechanism are shown in Table 3.6. Another important class of reactions are charge exchange reactions to species with higher electron affinity.

The third important type of reactions is associative electron detachment. This is an important loss process for the anions in flames. One reaction is included in the mechanism for which no kinetic data was available in the literature. It is the electron detachment from CHO_2^- after reaction with H atoms. A similar pathway for the consumption of CHO_2^- by H was suggested by Goodings et al. [GBN79b].

Unfortunately, only a few reactions were measured which lead to the cluster-ions CHO_3^- and CO_3^-, as can be seen in Table 3.4. In addition to the known reactions, H_2O is added as a second third body for the attachment of OH^- to carbon dioxide. In the atmospheric chemistry literature additional pathways are discussed leading to these cluster-ions. They involve species which were not observed at all or only in very low concentrations in the methane-oxygen

3-body electron attachment		Reference
$E^-+O_2+O_2 \rightleftharpoons O_2^-+O_2$	-	[CFGO00]
$E^-+O_2+H_2O \rightleftharpoons O_2^-+H_2O$	-	[CFGO00]
$E^-+O_2+N_2 \rightleftharpoons O_2^-+N_2$	-	[CFGO00]
$E^-+O_2+O \rightleftharpoons O_2^-+O$	-	[CFGO00]
$E^-+OH+M(1) \rightleftharpoons OH^-+M(1)$	factor 10	[Hay93]
$E^-+O+O_2 \rightleftharpoons O^-+O_2$	-	[CFGO00]
$E^-+O+O \rightleftharpoons O^-+O$	-	[SSZ01]
Associative electron detachment		
$O_2^-+H_2 \rightleftharpoons H_2O_2+E^-$	-	[Fil01]
$O_2^-+H \rightleftharpoons HO_2+E^-$	<factor 3	[SSZ01]
$OH^-+O \rightleftharpoons HO_2+E^-$	300 K, 50%	[GBN79b]
$OH^-+H \rightleftharpoons H_2O+E^-$	10-41000 K, factor 2	[TMM00]
$OH^-+C \rightleftharpoons CHO+E^-$	10-41000 K, factor 2	[TMM00]
$OH^-+CH \rightleftharpoons CH_2O+E^-$	10-41000 K, factor 2	[TMM00]
$OH^-+CH_3 \rightleftharpoons CH_3O+E^-$	10-41000 K, factor 2	[TMM00]
$O^-+C \rightleftharpoons CO+E^-$	10-41000 K, factor 2	[TMM00]
$O^-+H \rightleftharpoons OH+E^-$	10-41000 K, factor 2	[TMM00]
$O^-+H_2 \rightleftharpoons H_2O+E^-$	10-41000 K, factor 2	[TMM00]
$O^-+CH \rightleftharpoons CHO+E^-$	10-41000 K, factor 2	[TMM00]
$O^-+CH_2 \rightleftharpoons CH_2O+E^-$	10-41000 K, factor 2	[TMM00]
$O^-+CO \rightleftharpoons CO_2+E^-$	10-41000 K, factor 2	[TMM00]
$O^-+O \rightleftharpoons O_2+E^-$	10-41000 K, factor 2	[TMM00]
$O^-+C_2H_2 \rightleftharpoons CH_2CO+E^-$	298 K, 20%	[GBN79b]
$O^-+H_2O \rightleftharpoons H_2O_2+E^-$	-	[SSZ01]
$CHO_2^-+H \rightleftharpoons CO_2+H_2+E^-$	-	-
3-body cluster formation		
$OH^-+CO_2+O_2 \rightleftharpoons CHO_3^-+O_2$	298 K, 30%	[GBN79b]
$OH^-+CO_2+H_2O \rightleftharpoons CHO_3^-+H_2O$	-	-
$CO_3^-+H \rightleftharpoons OH^-+CO_2$	298 K, 40%	[GBN79b]
$CO_3^-+O \rightleftharpoons O_2^-+CO_2$	298 K, 50%	[GBN79b]
$O^-+CO_2+O_2 \rightleftharpoons CO_3^-+O_2$	298 K, 29%	[GBN79b]
Charge exchange reactions		
$O_2^-+OH \rightleftharpoons OH^-+O_2$	factor 10	[Hay93]
$O_2^-+O \rightleftharpoons O^-+O_2$	-	[CFGO00]

Table 3.4: Electron attachment and detachment reactions included in the reaction mechanism. In addition, the reactions leading to the cluster-ions and the charge exchange reactions are shown. If available, the temperature range as well as the uncertainties of the rate coefficients are given.

Charge transfer with rearrangement		Reference
$O_2^- + H \rightleftharpoons OH^- + O$	-	[SSZ01]
$OH^- + CHO \rightleftharpoons CHO_2^- + H$	-	-
$O^- + H_2 \rightleftharpoons OH^- + H$	10-41000 K, factor 2	[TMM00]
$O^- + CH_4 \rightleftharpoons OH^- + CH_3$	10-41000 K, factor 2	[TMM00]
$O^- + H_2O \rightleftharpoons OH^- + OH$	-	[CFGO00]
$O^- + CH_2O \rightleftharpoons OH^- + CHO$	300 K, total rate only	[BGN77]
$O^- + CH_2O \rightleftharpoons CHO_2^- + H$	300 K, total rate only	[BGN77]
$O^- + C_2H_6 \rightleftharpoons C_2H_5 + OH^-$	-	[SSTS02]
Ion-ion recombination		
$O_2^- + C_2H_3O^+ \rightleftharpoons O_2 + CH_3CO$	-	[SSTS02]
$O_2^- + C_2H_3O^+ \rightleftharpoons O_2 + CH_2CO + H$	-	-
$O_2^- + CH_5O^+ \rightleftharpoons O_2 + CH_3 + H_2O$	-	-
$O^- + C_2H_3O^+ \rightleftharpoons O + CH_3CO$	-	[SSTS02]
$O^- + C_2H_3O^+ \rightleftharpoons O + CH_2CHO$	-	-
$O^- + C_2H_3O^+ \rightleftharpoons O + CH_2CO + H$	-	-
$O^- + CH_5O^+ \rightleftharpoons O + CH_3 + H_2O$	-	-
$CHO_3^- + C_2H_3O^+ \rightleftharpoons CH_3CO^+CO_2 + OH$	-	-
$CHO_3^- + CH_5O^+ \rightleftharpoons CH_3OH + H_2O + CO_2$	-	-

Table 3.5: Charge transfer reactions and ion-ion recombination reactions involving the anions. The temperature range and error estimates are also shown, if available.

Species	EA [eV]	Species	EA [eV]
O_2	0.45	OH	1.80
CHO	0.31	CHO_2	3.50
C_2H_2	0.49	$CO_2 \cdot O$	3.26
O	1.46	$CO_2 \cdot OH$	3.67

Table 3.6: Electron affinities of some neutral species relevant for the anions in lean methane-oxygen flames. The data is taken from [Lid97], except OH which is taken from [FK04]; $CO_2 \cdot O$ and $CO_2 \cdot HO$ are taken from [Bar03].

flame and are left out of the mechanism for this reason, see the discussion in Section 5.3.2. These pathways proceed via O_3^-, O_4^-, and CO_4^-; see the review [SS95] for details.

A number of charge transfer reactions involving rearrangement could also be found. The reaction of OH^- and CHO which produces CHO_2^- was suggested by Calcote et al. [CJ66].

Finally, recombination reactions between the cations and the anions are important, since they are known to be very fast. Except for two reactions, no kinetic data could be found in the literature. In general, the recombination rates are expected to be roughly universal, see for instance [FK04]. Not all possible pairs of species are included in the mechanism for the recombination process, because only the most abundant species contribute.

3.2 Thermodynamic data

Thermodynamic properties like heat capacities, enthalpies, and entropies of neutral species occurring in combustion systems can be obtained from standard databases [CDD+85, MZG02, Bur01]. For simple hydrocarbons, as they appear in lean methane-oxygen flames, the data is almost complete and accurate. For a few charged species, the information required can be found in these references as well. However, for larger ions thermodynamic properties have to be estimated or can be calculated from spectroscopic data, if available.

The data for the species O, O_2, and N_2 is taken from [Sel02]. For all other neutral species a standard database is used [WMD97, Kar]. The complete thermodynamic information for the charged species E^-, CHO^+, H_3O^+, and O_2^- can be found in the NASA collection [MZG02]. In this work they are re-fitted into the old NASA format. The data for O^- and OH^- is obtained from [Bur01] without modification.

The thermodynamic information for the five remaining charged species is estimated in the following way: The temperature dependence of the heat capacity and, hence, the temperature dependence of the enthalpy and entropy is taken from a similar species; compare with the Equations 2.23 and 2.24. Only the enthalpy is shifted to yield the correct standard enthalpy of formation at 298 K. This information is available in the literature. The species CHO_3^- is an exception in the procedure stated above, because only the enthalpy has to be shifted. The heat capacity and entropy was found in the literature. All other information is available [LM87]. Table 3.7 lists the standard enthalpies of formation as well as the species which are used for the estimate. In the calculations an enthalpy of formation of -620 kJ/mol is used for the species CO_3^-, see the discussion in Section 5.3.2.

Species	$\Delta\overline{H}_f^0$ [kJ/mol]	Reference	$\overline{C}_p$ estimated from	Reference
CH_5O^+	586.18	[BE88]	CH_3OH	[Sel02]
$C_2H_3O^+$	659.4±1.1	[FKK+04]	CH_3CO	[Bur01]
CHO_2^-	-464.0±9.6	[Bar03]	HCOO	[Bur01]
CHO_3^-	-745.38	[Bar03]	HCO_3^-	[LM87]
CO_3^-	-480±40	[Bar03]	CO_3^{2-}	[LM87]

Table 3.7: Standard enthalpies of formation $\Delta\overline{H}_f^0(298\,\mathrm{K})$ of the charged species for which complete thermodynamic data is not available, together with the species used for the temperature-dependent heat capacities and entropies.

The uncertainties introduced by the lack of thermodynamic data only affect the calculation of the reaction rates for the backward reactions and therefore the thermodynamic equilibrium concentrations. The results for the local temperature are not affected by these uncertainties, because the ions do not contribute significantly to the mixture composition. The error in the temperature dependence of the heat capacity and, therefore, also in the values of $[\overline{H}(T)-\overline{H}(298\,\mathrm{K})]$ and $[\overline{S}(T)-\overline{S}(298\,\mathrm{K})]$ are believed to be small. For example, the maximum deviation in the heat capacities of the pair CHO/CHO^+ is 5% and for O_2/O_2^- 8% in the temperature range from 300 K to 2000 K, [MZG02]. The different standard enthalpies of formation are the most important properties which have to be adjusted. The comparably small differences in the entropies can be neglected in a first approximation. They become important only at higher temperatures when the free enthalpy $[\overline{G}(T) = \overline{H}(T) - T \cdot \overline{S}(T)]$ is evaluated.

3.3 Transport data

As described in Section 2.5, a number of input data is needed to calculate the transport properties, i. e., for the simulations of the species diffusion coefficients and the heat conductivity of the gas mixture. The advantage of the transport model used here is the utilization of so-called combination rules to calculate the interaction potentials between each pair of species, so that data is needed only for the single species and not for each pair. Only the parameter n of the $(n,6,4)$-potential, which has no direct physical meaning, and the electron collision cross sections are exceptions, because they depend on the collision partner.

If only neutral species are considered, the data needed is available and proves to yield good agreement with experiments. If charged species are to be included, not only data for the ions is required but also additional data is needed for the neutral species. The reason is the interaction between the ions and the

neutral species described by the (n,6,4)-potential. This function depends on the polarizabilities, dipole and quadrupole, and a dispersion coefficient of the neutral species.

In addition, electron momentum transfer collision cross sections are needed for all neutral species. Because of the strong energy dependence of this kind of collision, simple interaction potentials are not applicable.

Finally, some data is needed for the ions themselves. This is the dipole polarizability and a dispersion coefficient, as well as the rotational collision number. If the process of resonant charge transfer contributes significantly, additional parameters have to be provided.

For some combinations of background gas and ions, experimental data for mobilities can be found in the literature [EPM76, EMA$^+$78, ETMM84, BFL$^+$87]. Another database for ion transport in gases is maintained by Viehland [Vie04]. But in most of the cases, the diffusion coefficients have to be calculated from the mutual interaction potentials by combination rules. There are databases for the polarizabilities of the neutral species required [Lid97, TMM00, Joh04], but for charged species one has to refer to individual publications. If there is data available, in most of the cases it stems from quantum mechanical calculations. The situation is better for data on electron molecule collisions, see the reviews [BB02, Dut75].

3.3.1 Neutral species

The Lennard-Jones parameters as well as the rotational collision numbers are obtained from existing databases [Kar]. If no recent value of the electric dipole has been available in the literature [Lid97, TMM00, Joh04], the estimates found in the database were kept. Because the majority of the input data was retained from the database, the transport properties of the neutral species are unchanged. Also the heat conductivity of the gas mixture remains unchanged because the charged species occur in low concentrations only and do not contribute significantly. This guarantees that the changes made to the transport model do not influence the good results concerning the neutral flame species which had been obtained so far. The data for O and O_2 was completely taken from [Sel02].

Polarizabilities for most of the neutral species could be found in databases; only HCCO,CH_2CHO, CH_2CH_2OH, CH_3O_2H, CH_3CHOH had to be estimated. The values for C, H, CH_2CO, and C_2H_5OH were taken from [Lid97], H_2 and CH_3O_2 from [Kar]. All other polarizability data was found in the "Computational Chemistry Comparison and Benchmark DataBase" of NIST [Joh04]. This database offers a comparison of molecular properties which are obtained by different quantum mechanical calculations. If available, experimental data can also be found there. However, for most of the molecules only ab-initio calculations

Species	I_P [eV]	Species	I_P [eV]
H	13.6	CH_3OH	10.8
HCCO	9.5	CH_3CHO	10.2
HO_2	11.4	CH_3CHOH	6.7
H_2	15.4	CH_3CO	7.0
H_2O	12.6	CH_4	12.6
H_2O_2	10.6	CO	14.0
C	11.3	CO_2	13.8
CH	10.6	C_2H	11.6
CHO	8.1	C_2H_2	11.4
$^1CH_2$	10.4	C_2H_3	8.3
$^3CH_2$	10.4	C_2H_4	10.5
CH_2O	10.9	C_2H_5	8.1
CH_2OH	7.6	C_2H_5O	9.1
CH_2CO	9.6	C_2H_5OH	10.5
CH_3	9.8	C_2H_6	11.5
CH_3O	10.7	OH	13.0

Table 3.8: Ionization potentials of some neutral species occurring in methane-oxygen flames. All data is taken from [Lia03].

provide the data. Unfortunately, the values obtained depend strongly on the calculation method and basis sets used, so that an average value had to be used. This is a source of uncertainty, in most of the cases around 50%.

The dipole polarizabilities are important quantities. Because of the lack of data for the quadrupole polarizabilities α_q and dispersion coefficients C_6, they were estimated with the help of the dipole polarizabilities [Sel02]. If the ionization potential I_P of the molecule is known, the following estimates were used:

$$C_6 = \frac{3}{4}\alpha^2 I_P \qquad \text{and} \qquad \alpha_q = \frac{3}{2}\alpha^2 \frac{I_P}{e^2} \quad . \tag{3.3}$$

Otherwise the following empirical formulas were used, which give the properties as functions of the polarizability only:

$$\begin{aligned} \frac{C_6}{e^2}[\mathring{A}^5] &= \exp(1.3647 \cdot \ln(\alpha[\mathring{A}^3]) + 0.015942) \\ \alpha_q[\mathring{A}^5] &= \exp(1.42957 \cdot \ln(\alpha[\mathring{A}^3]) + 0.0317141) \quad . \end{aligned} \tag{3.4}$$

Table 3.8 shows all ionization energies which could be found. The electric dipoles were also updated from the NIST Computational Chemistry Database [Joh04].

Species	I_P [eV]	Reference I_P	α [Å^3]	Reference α
CHO^+	-	-	1.341	[Mar88]
H_3O^+	-	-	0.964	[KKS96]
O_2^-	0.451	[TS97]	1.581	same as O_2
$C_2H_3O^+$	-	-	3.036	est. from CH_2CO
CH_5O^+	18.3	[Rab84]	2.126	est. from CH_2CO
OH^-	1.83	[Lid97]	6.400	[CL90]
CO_3^-	2.69	[Lid97]	4.900	est. from NO_3^- [SCTJ03]
CHO_2^-	3.498	[Lid97]	5.100	[CDA$^+$01]
CHO_3^-	3.686	[Lid97]	5.100	same as CHO_2^-
O^-	1.46	[Lid97]	3.200	[MM73]

Table 3.9: Ionization potentials and polarizabilities of the charged species.

The following species are found there: OH, HO_2, H_2O_2, CH, $^1CH_2$, $^3CH_2$, CHO, CH_2O, CH_2OH, CH_2CO, CH_3, CH_3O, CH_3CHO, CH_3CO, CO, C_2H, C_2H_3, C_2H_5, C_2H_5O, OH. In the case of the dipoles, the uncertainties are much less than for the polarizabilities. They depend only weakly on quantum mechanical methods and basis sets. The resulting parameters are listed in Table C.3.

3.3.2 Ions

For each charged species – except the electron – four parameters are required: the polarizability, the dispersion coefficient, the rotational collision number, and the parameter n. There is no general database available, as in the case of neutral species. All data have to be found in individual journal papers. The "Quantum Chemistry Literature Database" proved to be a very valuable tool for finding the references [QCD04].

Most of the polarizabilities used in this work are obtained by quantum-mechanical calculations. Only for small and common ions, experimental data are available. The uncertainty of these calculations must be expected to be comparable to that one for neutral molecules. Dispersion coefficients could not be found, so that Equations 3.3 or 3.4 have to be used, depending on whether the ionization energies were found or not; see Table 3.9 for references. Finally, the rotational collision numbers are estimated to be equal to the neutral counterparts [Kar] or set to zero, if no such species exist. The error in the flame simulations due to this procedure is small because the rotational collision numbers are needed only for the heat conductivity of the gas mixture, and the contribution of the ions is negligible because of their low concentrations.

As the only resonant charge transfer process, the collision of the oxygen anion

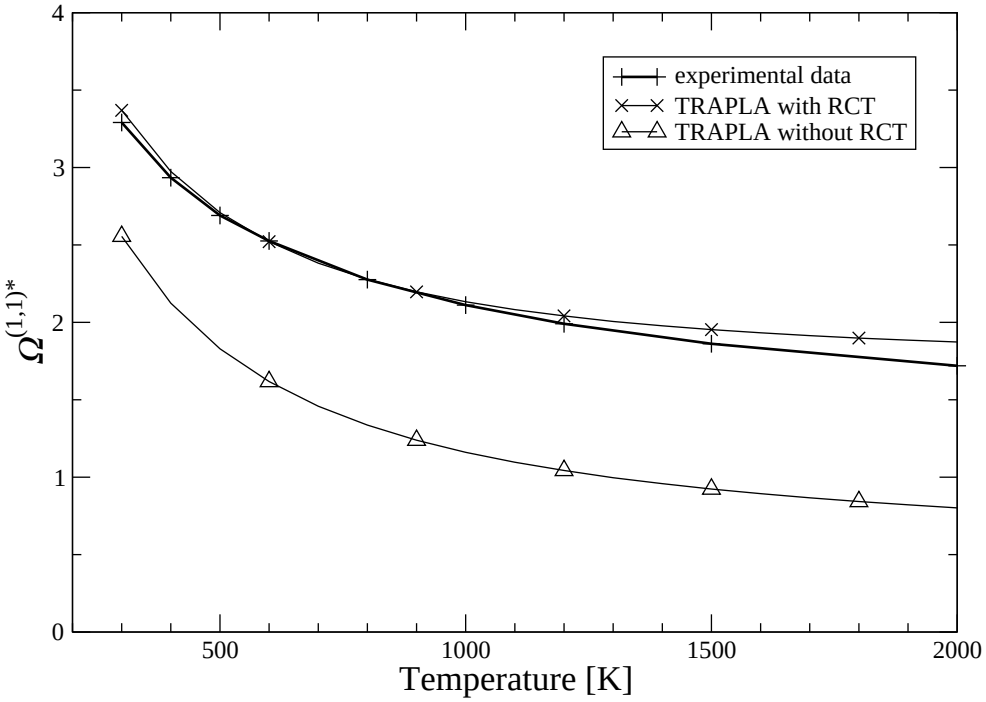

Figure 3.2: Reduced collision integral $\Omega^{(1,1)*}$ of the O_2^-/O_2 collision and its value if resonant charge transfer is neglected. The collision integral is up to a factor of two larger, if resonant charge transfer is taken into account.

with the neutral oxygen molecule is taken into account:

$$O_2^- + O_2 \rightharpoonup O_2 + O_2^- \quad .$$

The resonant charge transfer of the other possible collision pairs O/O^- and OH/OH^- can be neglected because the neutral counterparts have relatively low concentrations in the gas mixture, so that the respective binary diffusion coefficients will not contribute significantly to the effective diffusion coefficients in the mixture. In Figure 3.2 the experimentally determined reduced collision integral $\Omega^{(1,1)*}$ of the O_2^-/O_2 collision is shown [EPM76]. It is compared to the transport model if the interaction potential is used only, i. e., if resonant charge transfer is neglected. The final values used deviate from the experimental values at high temperatures, because the fit function used in the TRAPLA transport model does not describe the experiment in the whole temperature range. A higher accuracy is chosen at lower temperatures, at which the highest concentration of O_2^- is observed. As a consequence, the binary diffusion coefficient of O_2^- in oxygen is reduced by about a factor of two because of resonant charge transfer.

In Figure 3.3 the collision integrals of the O^-/O_2 and CO_3^-/O_2 collisions pre-

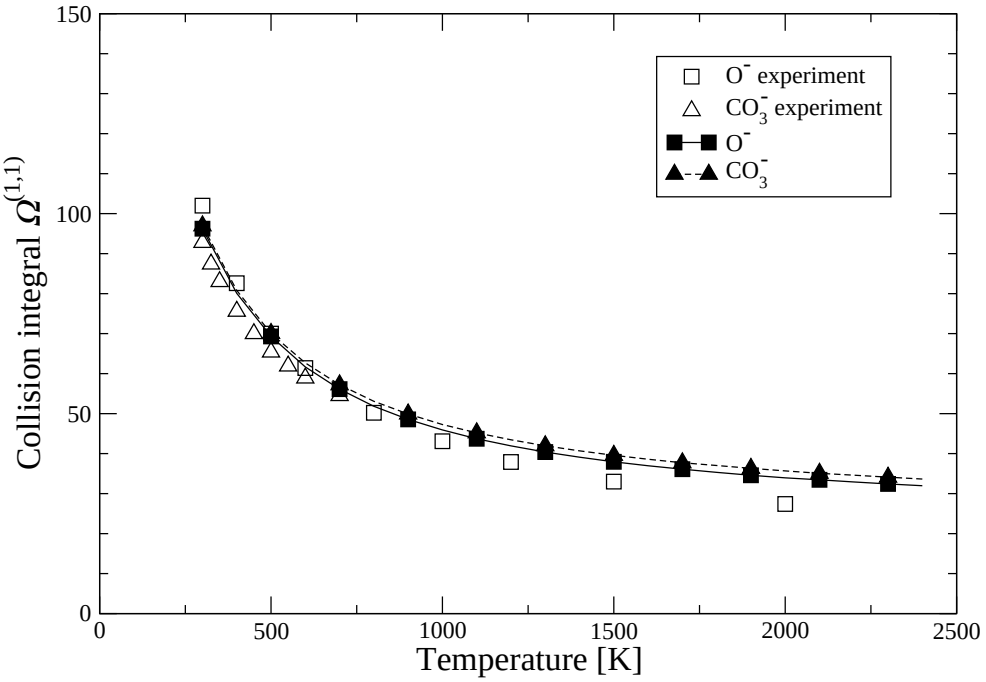

Figure 3.3: Collision integrals $\Omega^{(1,1)}$ of the O^-/O_2 and CO_3^-/O_2 collisions together with their experimental values. Open symbols show the measurements [EPM76], while lines with closed symbols show the results of the transport model.

dicted by the transport model are compared to experimental data. The agreement is quite satisfactory if one has in mind the uncertainties of the input data. The maximum error (approximately 25%) occurs at high temperature. Therefore, the corresponding binary diffusion coefficients have the same accuracy. Unfortunately, no experimental data could be found for comparison with the other collision pairs.

All resulting parameters are listed in the Appendix C in the Tables C.4 and C.5.

3.3.3 Electron collisions

In principle, detailed information about the electron collision with each neutral species is required by the transport model to calculate the diffusion coefficient of the electrons. In the best case, this would be differential collision cross sections for the elastic scattering process $q(E, \chi)$ or the transport integrals $Q^{(1)}(E)$ and $Q^{(2)}(E)$ directly, see Equation 2.29. This detailed data is not available in most of the cases.

In the literature, momentum transfer cross sections can be found, which are

equal to the first collision integrals $Q^{(1)}(E)$. Usually, the approximation

$$Q^{(2)} = Q^{(1)}$$

has to be made. However, this assumption only effects the contribution of the electrons to the heat conductivity of the mixture and the self-diffusion coefficient of the electrons D_{ee}. Because of the very low electron concentration, this error in the heat conductivity can be neglected. For the same reason, the diffusion coefficient of the electrons in the gas mixture is not affected by this approximation.

Not all possible collision partners have to be included in the database, only the most abundant ones have to be accounted for. Data for the electron scattering on O_2, H_2O, H_2, CO, CO_2, CH_4, C_2H_2, and C_2H_4 could be found in the literature and are included in the database, see Tables C.1 and C.2.

Chapter 4

Extension of the transport model

For charged species, it becomes necessary to extend the model for the calculation of their diffusion fluxes which has been used so far in flame simulations [War78a, War78b]. The extension will assure charge neutrality in every point in space which is maintained by ambipolar diffusion of charged species. A main goal of this thesis is to also include negatively charged ions into the model for the first time. For this reason the transport model for charged species, which has been applied to simulations of plasma etching etc., must be extended, because it is based on the assumption of an electropositive plasma only [Sel02, Rie03].

Up to now, the program MIXFLAME used for the flame simulations in this thesis considered neutral species only. In a spatial one-dimensional setting the following version of Fick's diffusion law is implemented for the mass diffusion flux j_i of all species i:

$$j_i = -D_i \rho \frac{\partial Y_i}{\partial x} \quad . \tag{4.1}$$

Here D_i is the diffusion coefficient of the species in the mixture, Y_i its mass fraction, the mixture density is denoted by ρ, and x represents the spatial dimension.

To maintain overall mass conservation, the sum of all diffusion fluxes has to vanish. The empirical Fick's law does not assure this automatically. Therefore the fluxes are corrected in the following way:

$$\tilde{j}_i = j_i - Y_i \sum_i j_i \qquad \text{and therefore} \qquad \sum_i \tilde{j}_i = 0 \quad . \tag{4.2}$$

This satisfies mass conservation, because the sum of the mass fractions is equal to one.

4.1 Ambipolar flow

With the inclusion of charged species, there is an additional condition to be fulfilled by the diffusion fluxes. In weakly ionized gases with a Debye length much smaller than the spatial extension of the system, the assumption of quasi-neutrality is valid. This means that in every point in space the sum of all charges is zero,

$$\sum_i \frac{Z_i e \overline{M}}{M_i} Y_i = 0 \quad . \tag{4.3}$$

This is only guaranteed, if the sum of all charge diffusion fluxes also becomes zero [Fra03b],

$$\sum_i \frac{Z_i e \overline{M}}{M_i} j_i = 0 \quad . \tag{4.4}$$

Here, $Z_i e$ is the charge of species i, M_i is its molar mass, and $\overline{M}$ denotes the mean molar mass of the mixture. The diffusion fluxes are calculated to meet this condition as shown below. Afterwards, the fluxes are corrected to assure total mass conservation as shown in Equation 4.2. This second correction does not violate the first condition because of the mixture being quasi-neutral.

The physical picture behind Equation 4.4 is that the charge separation resulting from different diffusion velocities causes an electric field, which forces the charged species back to quasi-neutrality. In general, the electrons are slowed down because of their much higher diffusion coefficients, and in the simple case of an electropositive gas, all the cations become accelerated. These processes appear on the scale of the Debye length, which is the distance at which the individual Coulomb potentials get screened by species of the opposite sign of charge.

In the new model, the diffusion of charged species is not only caused by a gradient in its mass fraction, but also by an electric field E:

$$j_i = -D_i \rho \frac{\partial Y_i}{\partial x} \pm \mu_i Y_i \rho E \quad . \tag{4.5}$$

The mobility is denoted by μ. For a positively charged ion the plus sign applies, the negative sign has to be used otherwise. After insertion into Equation 4.4 one obtains the expression for the internal electric field which causes neutrality:

$$E = \frac{\sum_i \frac{Z_i D_i}{M_i} \frac{\partial Y_i}{\partial x}}{\pm \sum_i Z_i \mu_i Y_i / M_i} = \frac{kT}{e} \frac{\sum_i \frac{Z_i D_i}{M_i} \frac{\partial Y_i}{\partial x}}{\sum_i Z_i^2 D_i Y_i / M_i} \quad . \tag{4.6}$$

For the latter expression, the Einstein relation was used in order to express the mobility of a species with the help of its diffusion coefficient. Herein, T is the

gas temperature, k the Boltzmann constant, and e the elementary unit of charge [PEAM75]:

$$\mu_i = \frac{|Z_i|e}{kT} D_i \quad . \tag{4.7}$$

It turned out to be numerically unstable to calculate the ambipolar electric field E explicitly and to insert its numerical value into the Equations 4.5. The instabilities are caused by the denominator of Equation 4.6, which also approaches zero if the ion concentrations nearly vanish. This situation occurs especially in the cold region of the flame. It is favorable to insert Equation 4.6 into Equation 4.5 for the diffusion fluxes analytically and to sort the terms according to the gradients of the species. In addition to arriving at numerically stable expressions for the fluxes, the structure of ambipolar diffusion becomes more clear. Finally, the following expression results for the mass diffusion flux of the charged species:

$$j_i = (1 - \beta_i) j_i^0 - \beta_i \sum_{j \neq i} \frac{Z_j M_i}{Z_i M_j} j_j^0 \quad . \tag{4.8}$$

Herein, j_i^0 denotes the diffusion flux of species i without ambipolar diffusion, i. e. Fick's law, β_i is its mole fraction weighted by the diffusion coefficient:

$$j_i^0 = -D_i \rho \frac{\partial Y_i}{\partial x} \tag{4.9}$$

$$\beta_i = \frac{Z_i^2 D_i X_i}{\sum_j Z_j^2 D_j X_j} = \frac{Z_i^2 D_i Y_i / M_i}{\sum_j Z_j^2 D_j Y_j / M_j} \quad . \tag{4.10}$$

This fraction is almost unity for the electrons in most situations because of their much higher diffusion coefficient. In an electropositive gas, i. e., a gas that contains only positively charged ions and electrons, this statement is always true, because in addition to the high diffusion coefficient the mole fraction of the electron is the largest of all charged species because of quasi-neutrality.

This situation changes, if negatively charged ions are included in the model. Then, in general, regions in space will exist, in which virtually all the electrons are attached to neutral species and, hence, their mole fraction becomes zero. This changes the process of ambipolar diffusion fundamentally [Fra02, Fra03a].

Equation 4.8 can be rewritten in a more convenient form, if the charge flux c_i of species i, in units of the elementary charge, is used instead of the mass flux. This results in the following expressions:

$$c_i = c_i^0 - \beta_i \sum_j c_j^0 \qquad \text{with} \qquad c_j^0 = Z_j \frac{\overline{M}}{M_j} j_j^0 \quad . \tag{4.11}$$

This equation has the same structure as the correction of the diffusion fluxes, guaranteeing overall mass conservation; compare to Equation 4.2. This leads to

the simple picture that all the charged species have to compensate for the non-vanishing total charge flux, $\sum c_j^0$, according to their ability to diffuse expressed by β_i.

4.2 Limit case: Electrons dominate the ambipolar diffusion process

The electrons dominate the ambipolar diffusion process as long as their mole fraction X_e is high enough,

$$X_\mathrm{e} D_\mathrm{e} \gg Z_j^2 X_j D_j$$

for all other charged species j. The fluxes of the heavy charged species can be simplified in this case. In the sum of Equation 4.11, the term which involves the electron diffusion dominates over all other terms, because the electron diffusion coefficient is much higher than the coefficients of the heavy charged species. The ratio $D_\mathrm{e}/D_{i\neq\mathrm{e}}$ is usually higher by a factor of a few hundreds. To see this, one can use the neutrality condition to express the gradient of the electron mass fraction in the gradients of all other charged species. Expressed in terms of diffusion fluxes this yields

$$c_\mathrm{e}^0 = -\sum_{j\neq\mathrm{e}} \frac{D_\mathrm{e}}{D_j} c_j^0 \quad . \tag{4.12}$$

After inserting this expression into Equation 4.11, one can see that the electron contribution dominates, because $\frac{D_\mathrm{e}}{D_j} \gg 1$. The following diffusion fluxes of the heavy charged species result, if the electrons dominate the diffusion process:

$$c_i \approx c_i^0 - \beta_i c_\mathrm{e}^0 \quad \text{for} \quad i \neq \mathrm{e} \quad . \tag{4.13}$$

This shows that the non-vanishing charge flux is mostly caused by the electrons, and that the heavy charged species have to compensate for this, depending on their ability to diffuse. In the limit of dominating electrons, β_i can also be approximated. Finally, the following expression results for the heavy charged species:

$$\beta_i \approx Z_i^2 \frac{X_i D_i}{X_\mathrm{e} D_\mathrm{e}} \quad , \quad c_i \approx c_i^0 - \frac{Z_i^2 X_i D_i}{X_\mathrm{e} D_\mathrm{e}} c_\mathrm{e}^0 \quad \text{for} \quad i \neq \mathrm{e} \quad . \tag{4.14}$$

As long as the electron concentration is high enough, the compensation term in the diffusion fluxes of the charged species depends on the gradient of the electron concentration. This compensation is larger for species with a high mole fraction and high mobility. In terms of mass fluxes instead of charge fluxes, one can see

that this compensation term is added for cations and subtracted for anions. In simple words, cations have to follow the electrons and anions have to diffuse in opposite direction to assure quasi-neutrality.

No such simple relation can be found for the electron in this limit, because all terms in Equation 4.11 become important if $\beta_\mathrm{e} \approx 1$. On the one hand, the free diffusion of the electron almost cancels itself, $1 - \beta_\mathrm{e} \approx 0$, and on the other hand, the fluxes of the heavy charged species become important. In the special case that all heavy charged species diffuse approximately with the same coefficients, i. e. $D_j \approx \overline{D}$, and that there are only singly charged ions ($|Z_j| = 1$), one obtains a simple expression for the electron diffusion. If Equation 4.13 is used to eliminate the diffusion fluxes of all heavy species from Equation 4.11, the following expression is obtained for the electrons:

$$c_\mathrm{e} = \left((1 - \beta_\mathrm{e}) + \beta_\mathrm{e} \frac{\overline{D}}{D_\mathrm{e}} \right) c_\mathrm{e}^0 \quad . \tag{4.15}$$

In the limit of dominating electrons, the expression for β_e can be simplified:

$$\beta_\mathrm{e} \frac{\overline{D}}{D_\mathrm{e}} \approx \frac{\overline{D}}{D_\mathrm{e}} \qquad \text{and} \qquad (1 - \beta_\mathrm{e}) \approx \frac{\overline{D}}{D_\mathrm{e}} \quad . \tag{4.16}$$

This means that in this case the electrons diffuse with an effective ambipolar diffusion coefficient D_a, which is approximately twice the diffusion coefficient of the charged heavy species,

$$c_\mathrm{e} \approx \frac{D_\mathrm{a}}{D_\mathrm{e}} c_\mathrm{e}^0 \qquad \text{with} \qquad D_\mathrm{a} = 2\overline{D} \quad . \tag{4.17}$$

To summarize, one finds that, as long as the mole fraction of the electrons is not lower than a factor of a few hundreds of the mole fractions of all other charged species, the electrons diffuse according to Fick's law with a diffusion coefficient of roughly twice that of the heavy charged species. They, in turn, have to compensate the charge separation caused by the diffusion of the electrons. The resulting diffusion flux differs significantly from Fick's law, so that in general the ambipolar diffusion of the heavy charged species cannot be described by a simple effective diffusion coefficient.

4.3 Electrical conductivity

Following the procedure of Murphy [Mur93], the expression for the electrical conductivity is derived here for the new model of ambipolarity. The charged species are exposed to an additional external electric field E^e and the ambipolar

field E^{a}, which has been discussed above. The diffusion flux of species i is changed accordingly:

$$j_i = -D_i \rho \frac{\partial Y_i}{\partial x} + \frac{Z_i e}{kT} D_i Y_i \rho \left(E^{\mathrm{e}} + E^{\mathrm{a}}\right) \quad . \tag{4.18}$$

Only the external field causes a global charge flux, where the electrical conductivity σ_{e} is the constant of proportionality:

$$\sum_i Z_i e \frac{N_{\mathrm{A}}}{M_i} j_i = \sigma_{\mathrm{e}} E^{\mathrm{e}} \quad . \tag{4.19}$$

If Equation 4.18 is inserted into Equation 4.19, and the terms containing the external electric field are collected, the following expression results for the electrical conductivity:

$$\sigma_{\mathrm{e}} = \frac{e^2 N_{\mathrm{A}}}{kT} \sum_i \frac{Z_i^2 \rho}{M_i} D_i Y_i \quad . \tag{4.20}$$

If one has in mind, that Y_i/M_i is proportional to the mole fraction of species i, the equation shows that species with high diffusion coefficients and concentrations will cause the electrical conductivity. This will usually be the electrons.

4.4 Analysis of ambipolar diffusion in a simplified flame

The assumption that the electrons dominate the diffusion process cannot be made in general. The reason for this is that the electrons get attached to neutral species forming anions, which are not as mobile as the electrons because of their higher mass. In flames this happens on the cold side, because the electrons detach more easily as the temperature increases.

It is not possible to obtain simple limiting expressions in this general case, for instance in terms of the local electronegativity, not even if there are only three kinds of charged species (electrons, one type of anions/cations) [Rog85]. Therefore, the numerical result of a simplified problem will be presented here, which exhibits the main features of the flame simulations presented in Chapter 5. All the conditions and parameters are exactly like in these simulations, but only four charged species are considered. In addition to electrons, the cations CHO^+, H_3O^+, and the anion O_2^- are included. The reaction mechanism consists only of the ion inception reactions (positive and negative) together with the reaction forming the main charged product:

$$\begin{aligned} \mathrm{CH} + \mathrm{O} &\rightleftharpoons \mathrm{CHO}^+ + \mathrm{e}^- \\ \mathrm{e}^- + \mathrm{O}_2 + \mathrm{O}_2 &\rightleftharpoons \mathrm{O}_2^- + \mathrm{O}_2 \\ \mathrm{CHO}^+ + \mathrm{H}_2\mathrm{O} &\rightleftharpoons \mathrm{H}_3\mathrm{O}^+ + \mathrm{CO} \quad . \end{aligned}$$

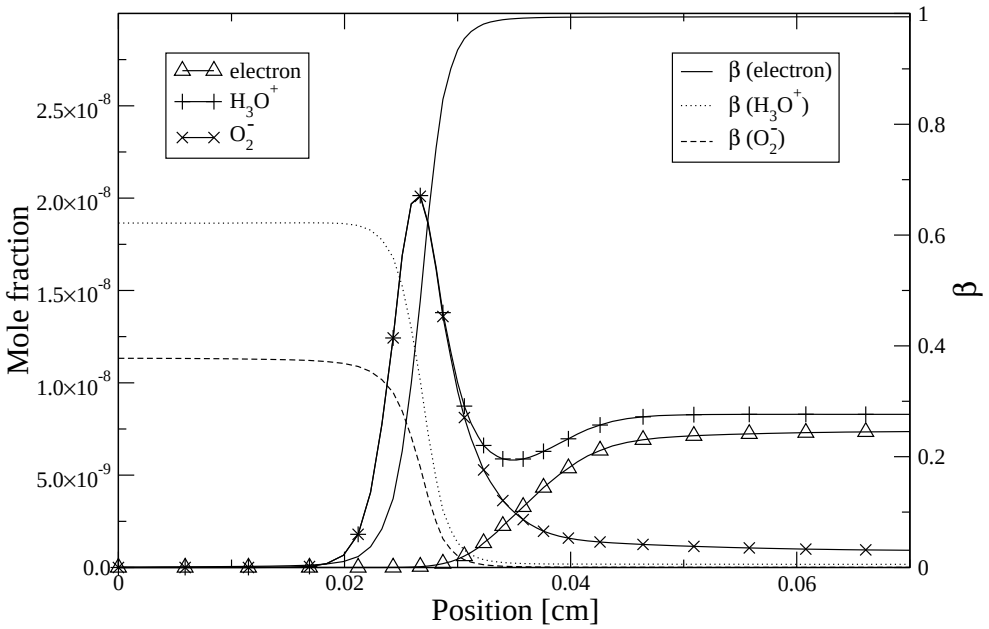

Figure 4.1: Species profiles and β_i for all charged species. Lean methane-oxygen flame as in Chapter 5, but only a reduced ion reaction mechanism is used.

In Figure 4.1 the species mole fractions are shown with their β values. The cold and unburnt side of the flame is on the left side, while the hot downstream zone is on the right.

The electrons occur in the reaction zone of the flame, where sufficient amounts of CH and O radicals are produced. These electrons get effectively attached to oxygen molecules in the cold zone of the flame. In the hot part, the electrons get detached again, leading to the maximum in the O_2^- profile. The CHO^+ ion produced reacts immediately to H_3O^+, so that its mole fraction remains very low. Therefore, it will not be discussed here.

The ion mole fractions in this lean methane-oxygen flame are relatively low, but high enough to keep the Debye length smaller than the typical structures of the species profiles. Therefore, the assumption of ambipolar diffusion is valid in this system, as shown in Figure 4.2.

As soon as the electron mole fraction increases to the level of the negative species, it starts to dominate the ambipolar diffusion process, as outlined in the previous section. In the simulation, this is the case for $x > 0.03$ cm, as β_e approaches one. Even though the electrons vanish almost completely for 0.02 cm $< x <$ 0.03 cm, they still contribute considerably to the diffusion fluxes of the other two species. This can be observed in the Figures 4.3 to 4.5, in which the ambipolar fluxes are compared to Fick's law for all species. The single

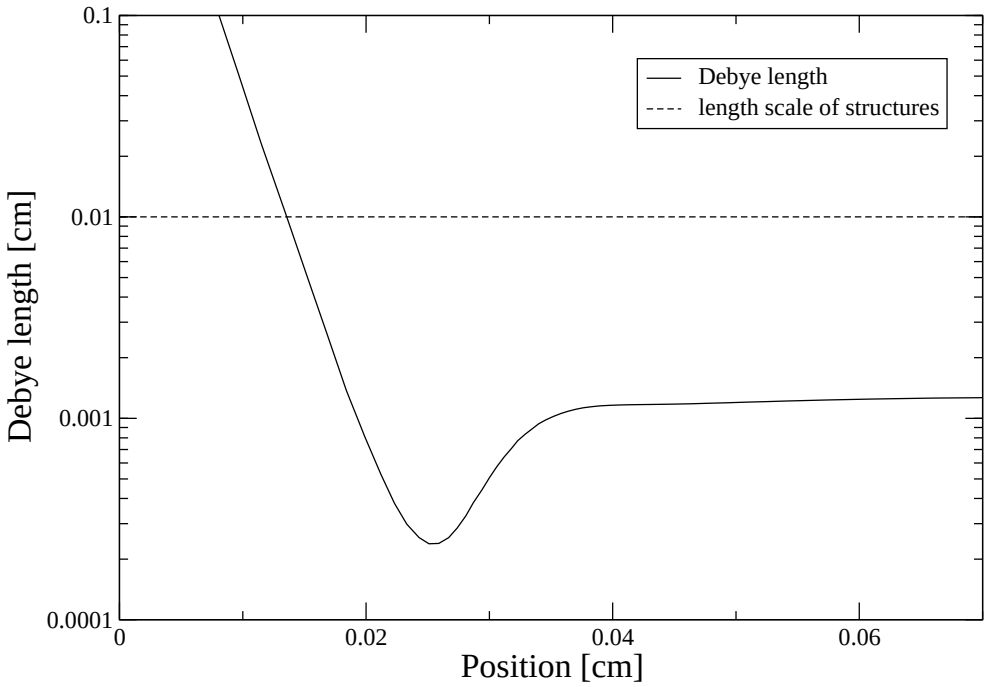

Figure 4.2: The Debye length is smaller than the typical structures of the species profiles at all relevant positions in the flame. The assumption of ambipolar diffusion is valid.

contributions to the ambipolar flux in Equation 4.11 are also shown.

Concerning the electrons, two features are striking. First, the free diffusion flux is much larger than the ambipolar flux; thus, the electrons get decelerated to approximately meet the diffusion fluxes of the other charged species. Secondly, the term $(1 - \beta_e)c_e^0$ is the main contribution to the ambipolar flux in the entire flame. At positions $x > 0.03$ cm, where the electrons dominate, the ambipolar flux is increased to a certain amount according to Equation 4.17. In this simplified flame, the ambipolar diffusion of the electrons could be described by an effective diffusion coefficient $D_a \approx (1 - \beta_e)D_e$.

The situation is completely different for the ion H_3O^+, see Figure 4.4. Its ambipolar flux differs completely from Fick's law. In particular, there are regions in which the diffusion even has the opposite direction. The largest contribution to the flux is again caused by the electrons for $x > 0.025$ cm. Only for $x < 0.025$ cm, the electrons lose their importance, so that the flux of O_2^- contributes significantly. This is a minor effect in this sample problem, but in other situations, in which the concentrations of all charged species do not vanish together with the electrons, it becomes an important feature of the transport model.

The ambipolar flux of O_2^- has the same qualitative features as the free dif-

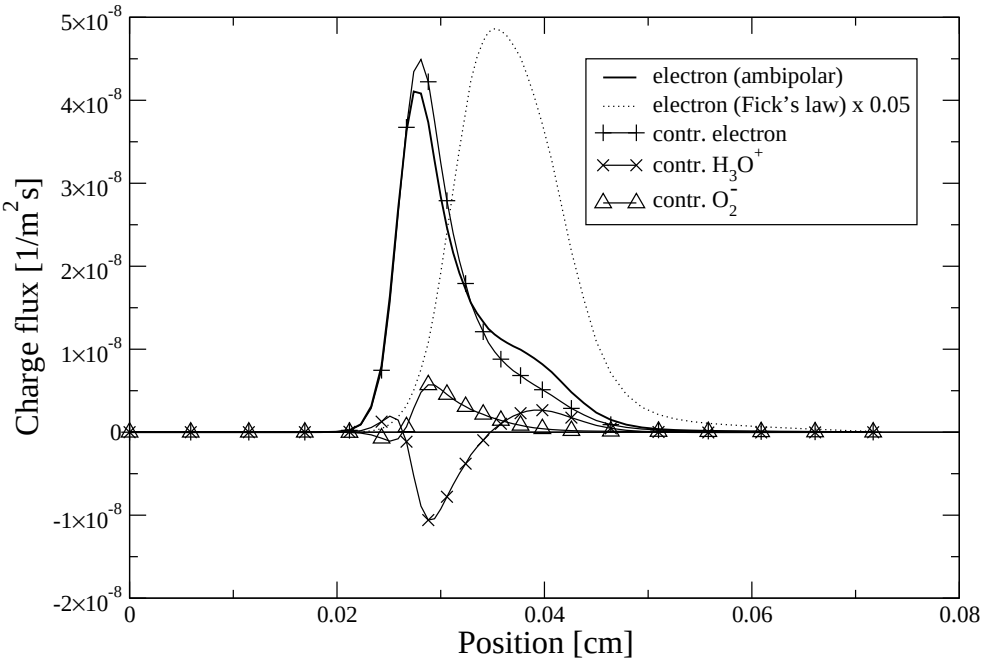

Figure 4.3: Ambipolar flux of the electrons, their flux following Fick's law c^0, and the single contributions in Equation 4.11, i. e. $(1 - \beta_\mathrm{e})c^0_\mathrm{e}$ and $\beta_\mathrm{e} c^0_j$.

fusion law, see Figure 4.5. The electrons dominate again for $x > 0.025$ cm, as expected. The correction term due to ambipolarity leads to diffusion into the same direction as determined by Fick's law, so that the qualitative diffusion behavior of O_2^- remains the same while the diffusion speed increases.

Overall, the following qualitative picture results for the simplified stationary flame, see also the local chemical production rates in Figure 4.6: The first ions, i. e. electrons and CHO^+, are produced in the region between 0.04 cm and 0.05 cm. CHO^+ immediately reacts to H_3O^+, so that it does not reach a significant concentration. The electrons diffuse to the cold side of the flame, where they get attached to oxygen molecules to form O_2^- with a high rate. This attachment/detachment balance strongly depends on the local temperature, leading to a maximum of the O_2^- concentration. Most notably, the cation H_3O^+ has to follow the electron diffusion to the cold side of the flame, where it finally reaches a maximum far upstream from the place of its production. This feature would be absent without the extension of the transport model to include ambipolar diffusion.

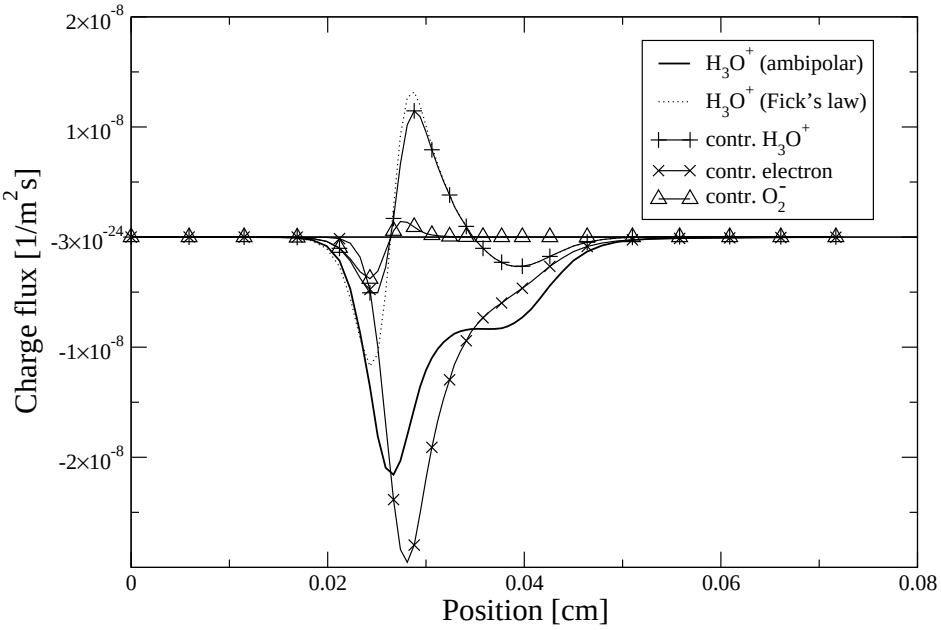

Figure 4.4: Ambipolar flux of H_3O^+, its flux following Fick's law c^0, and the single contributions in Equation 4.11, i. e., $(1-\beta_i)c_i^0$ for H_3O^+ and $\beta_i c_j^0$ for the other species.

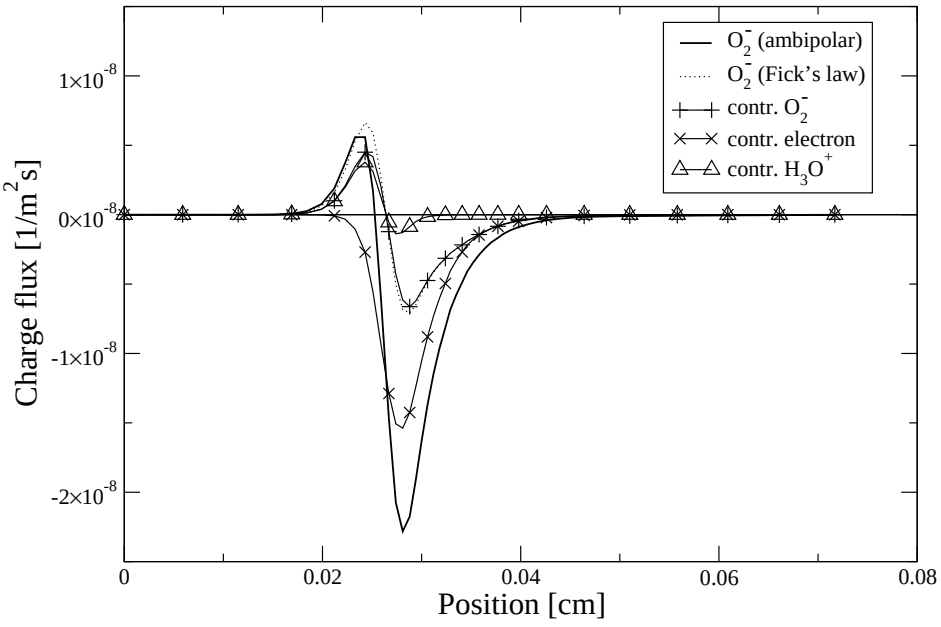

Figure 4.5: Ambipolar flux of O_2^-, its flux following Fick's law c^0, and the single contributions in Equation 4.11, i. e., $(1-\beta_i)c_i^0$ for O_2^- itself and $\beta_i c_j^0$ for the other species.

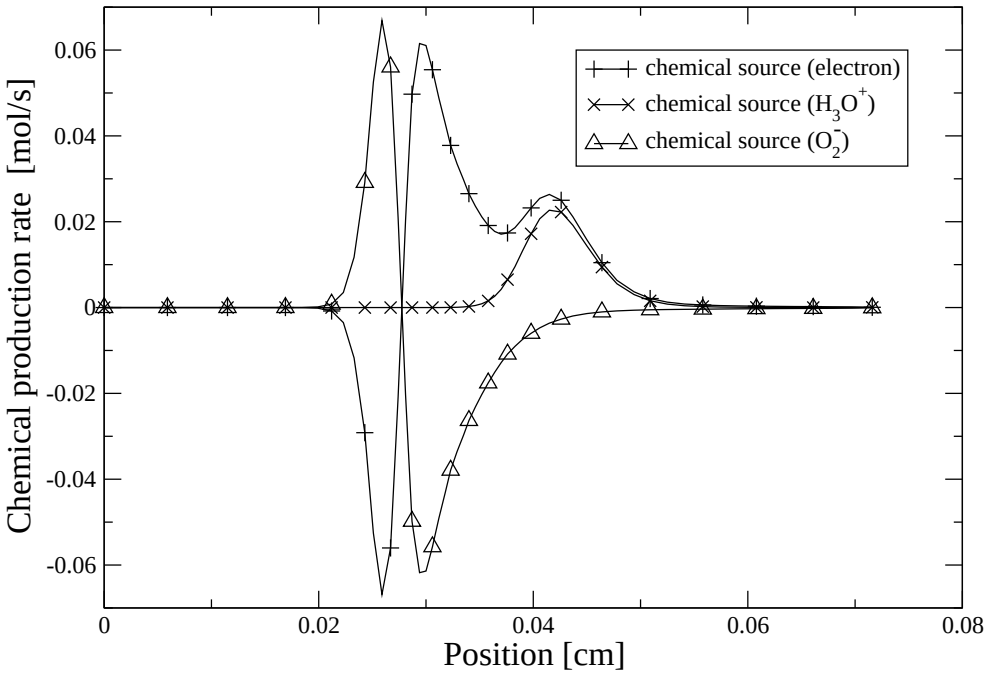

Figure 4.6: Profiles of the chemical production rates for the electrons, H_3O^+, and O_2^-. Two regions can be identified: First, the electron attachment/detachment region 0.02 cm $< x <$ 0.035 cm, and the ion production region around 0.045 cm.

Chapter 5

One-dimensional flame simulations

In this chapter, the simulation results for a one-dimensional flat methane-oxygen flame are presented and compared to the experimental data of Goodings et al. [GBN79a, GBN79b]. The program which has been utilized for these calculations is MIXFLAME, described in Section 2.1.

In the first section, the necessary extensions to the program are presented. Afterwards, the experiments used for validation are introduced. In the following part, the simulation results are presented: First, as a starting point, the neutral species profiles are compared to experimental data, then total ion concentrations are shown followed by a discussion of the single species profiles. The reaction mechanism for the cations and anions is analyzed. With this mechanism, the main reaction channels are identified. A discussion of the influence of the new ambipolar diffusion model on the concentration profiles of the charged species is following. Finally, the sensitivities of the simulation results to the temperature profile in the flame and to uncertainties in the input data of the transport model are studied.

5.1 Adaptation of the numerical scheme

In addition to several changes in MIXFLAME due to the fact that all species properties, like thermodynamical data, heat conductivities, diffusion coefficients etc., have to be provided by the TRAPLA library, also the numerical part of the program itself had to be adapted to the new scheme of ambipolar diffusion of the charged species, as introduced in Chapter 4.

As can be seen from Equation 4.8, the diffusion flux of all charged species does no longer only depend on the gradient of its mass fraction. However, the

numerical scheme, applied so far, depends on this assumption, because the differential equations for the mass fractions are put into the standard form shown in Equation 2.12.

To cope with this, the diffusion flux is split into one part depending directly on the gradient of the species i itself and a second one containing all other contributions:

$$j_i = -(1-\beta_i) D_i \rho \frac{\partial Y_i}{\partial x} - \beta_i \sum_{j \neq i} \frac{Z_j M_i}{Z_i M_j} j_j^0 \quad . \tag{5.1}$$

After inserting this expression into the differential Equation 2.5 and putting this into the standard form mentioned above, one obtains the following four new coefficients for a charged species i:

$$\begin{aligned} A &= A^0 \\ B_i &= (1-\beta_i) B_i^0 \\ C &= C^0 \\ D_i &= D_i^0 + A \frac{\partial}{\partial \phi} \left(-\beta_i \sum_{j \neq i} \frac{Z_j M_i}{Z_i M_j} j_j^0 \right) \quad . \end{aligned}$$

Here, the superscript "0" denotes the coefficients without ambipolar diffusion. The equations for the neutral species remain unchanged.

In addition to these changes, it became necessary to reduce the relative time step size because of the higher reaction rates of ion-molecule reactions.

5.2 Comparison with experimental data

5.2.1 Experiments

The most detailed measurements of charged species profiles in premixed methane flames were conducted at York University, Canada. In these experiments, a simple conical methane-oxygen flame burns at atmospheric pressure surrounded by a shielding argon flow. The flame can be moved relative to a pinhole, through which the gas mixture is sampled into an ion mass spectrometer. In this way, spatial species profiles of positive and negative ions can be measured along the flame axis. Measurements were done on fuel-lean and rich flames (equivalence ratios Φ=0.216 and Φ=2.15) [BGN77, GBN79a, GBN79b, Boh79]. All positive flame ions below 55 and all negative ones below 100 atomic mass units could be detected. A disadvantage of these measurements is the lack of information about the local temperature and the neutral species profiles in the flame. This would be important, since these conical flames are expected to differ from flat ones simulated in this work. The measurements do not give absolute values of single

ion concentrations, but the maximum positive ion concentration is estimated. Moreover, it has to be kept in mind that the mass-spectrometric sampling of ions can lead to deviations from the actual species concentrations because of fast reactions possibly occurring in the vacuum chamber. Electrons can also diffuse to the metallic sampling cone, see for instance [Hay93]. The experiment of Goodings was chosen here, because it offers high resolution measurements of 11 cations, but also of 30 anions in the lean flame.

As a second experiment, the measurements of Wortberg are used to compare the simulation results for the total positive ion concentration with [Wor65]. In this experiment, a flat premixed methane-air flame burns at atmospheric pressure. The mixture is fuel-lean, $\Phi = 0.513$. The positive ion concentration is measured by a Langmuir probe. Absolute values of the total ion concentration as well as the local temperature are given.

5.2.2 Neutral species

Because of the low concentrations of ions in these flames, the neutral species serve as a bath of species for the production and conversion of the ions due to ion-molecule reactions. Therefore, a well established reaction mechanism for the neutral species, which reproduces their concentration profiles well, is a necessary precondition for modeling ion concentration profiles.

In Figure 5.1 the simulation results are compared to experimental data of a flame [PM73] which is similar to the one examined by Goodings et al. This methane-oxygen flame has almost the same stoichiometry ($\Phi = 0.2$), but it has a flat geometry and burns at a lower pressure of 5.3 kPa. For this qualitative comparison, the distance scale has been converted to atmospheric pressure by assuming an inversely proportional dependence on pressure [GBN79a]. Afterwards, the experimental data is shifted by 0.048 cm to correct the different origin of the coordinate system compared to the simulation.

The agreement is very good for the major combustion reactants; also the shape and position of minor chemical species is satisfactory, while small deviations up to a factor of two are observed in the maximum mole fractions. Overall, the reaction mechanism for neutral species seems to offer a good basis for the examination of the ion chemistry in this lean methane-oxygen flame.

5.2.3 Total ion concentration

The total ion concentration, as a global property of the flame, determines the electrical conductivity of the flame. Especially the ratio between negatively charged ions and electrons is important, because effectively the electron concentration

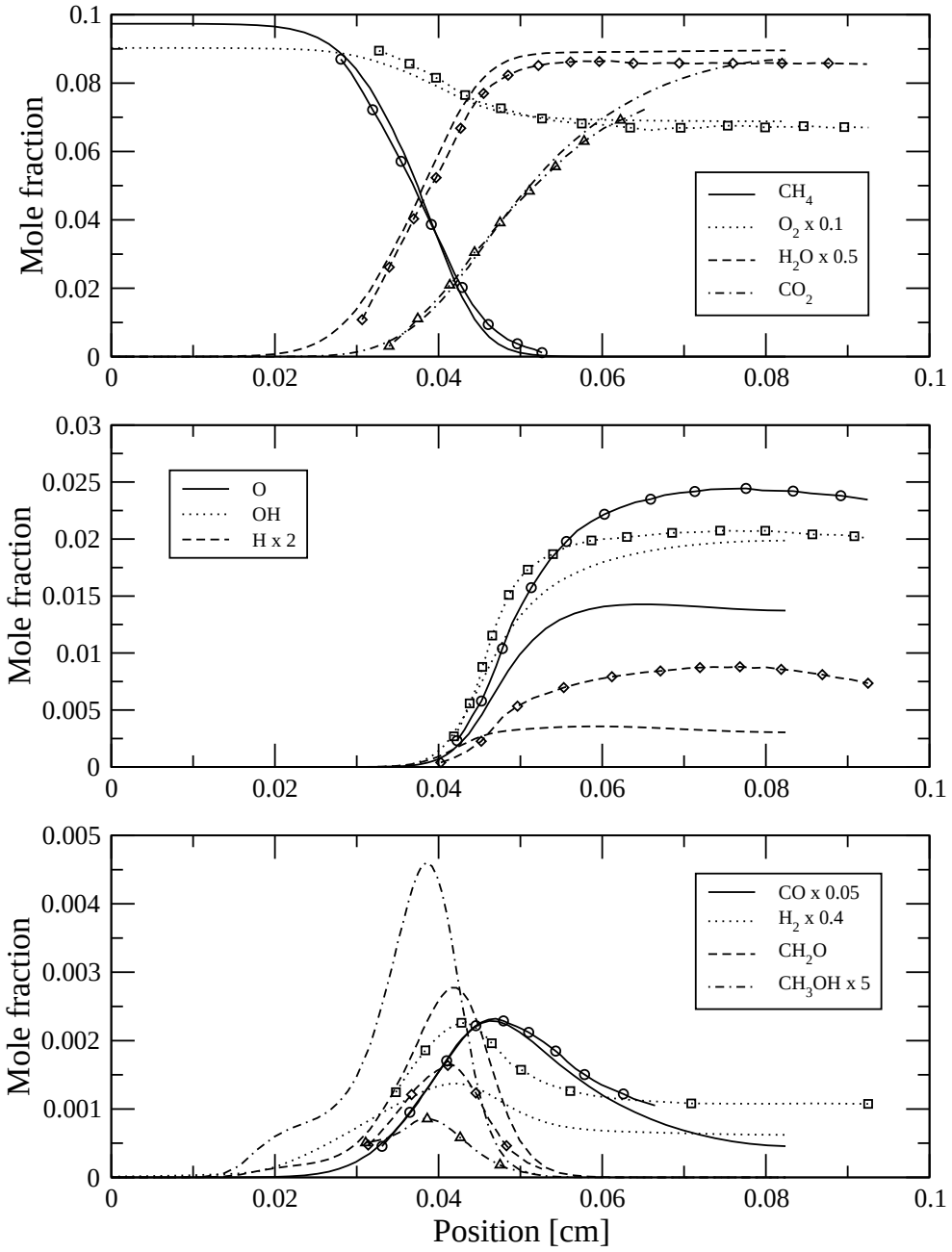

Figure 5.1: Mole fractions of major neutral species and radicals in a premixed flat methane-oxygen flame ($\Phi = 0.2$) measured by Peeters et al. [PM73]. The experimental data (symbols) are compared to the simulation results of this work. The experimental space coordinate has been transformed to atmospheric pressure by assuming reciprocal pressure dependence [GBN79b] and shifted by 0.048 cm.

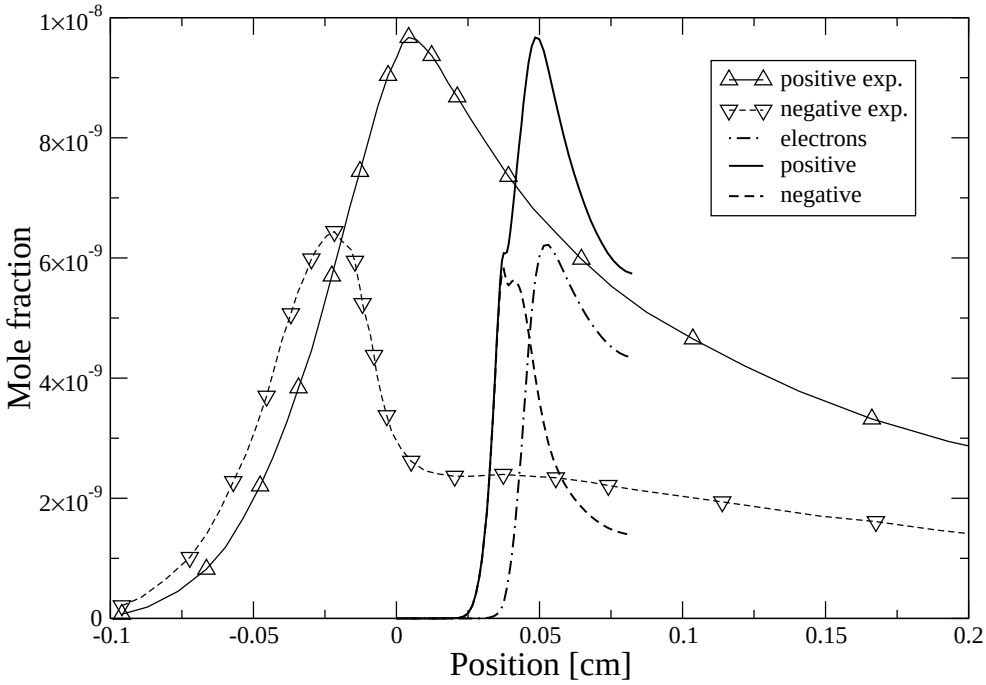

Figure 5.2: Total mole fractions of positive and negative ions in comparison to the experiment of Goodings et al. [GBN79b]. Also shown is the resulting mole fraction of the electrons. The experimental data (symbols) has been scaled to give the same maximum positive ion mole fraction. The different space coordinates are kept for visibility reasons. Except for the different widths of the ion profiles, the simulation results agree well with the experimental data.

alone is responsible for the electrical conductivity, as will be discussed in Section 5.2.6. For most of the applications, it is important that the model predicts this feature accurately.

In Figure 5.2 the simulation results for the total concentrations of cations and anions are compared to the experimental data. The experimental data is scaled, so that the maximum positive ion mole fractions are matched. The same scaling factor is used for the negative ions. Because of the lack of data for the local temperature or the neutral species profiles, the offset in the position coordinate between experiment and simulation cannot be determined and is not shifted.

The general shape of the profiles as well as the ratio between positive and negative ions compare well to the experiment. In the simulation, the maximum positive ion mole fraction corresponds to 1.7×10^{10} ions/cm^3, which agrees to the experimental findings of Goodings, who gives values between 1.3 and 4×10^{10} ions/cm^3 [GBN79b, Boh79].

Figure 5.2 shows clearly that the experimental profiles are stretched com-

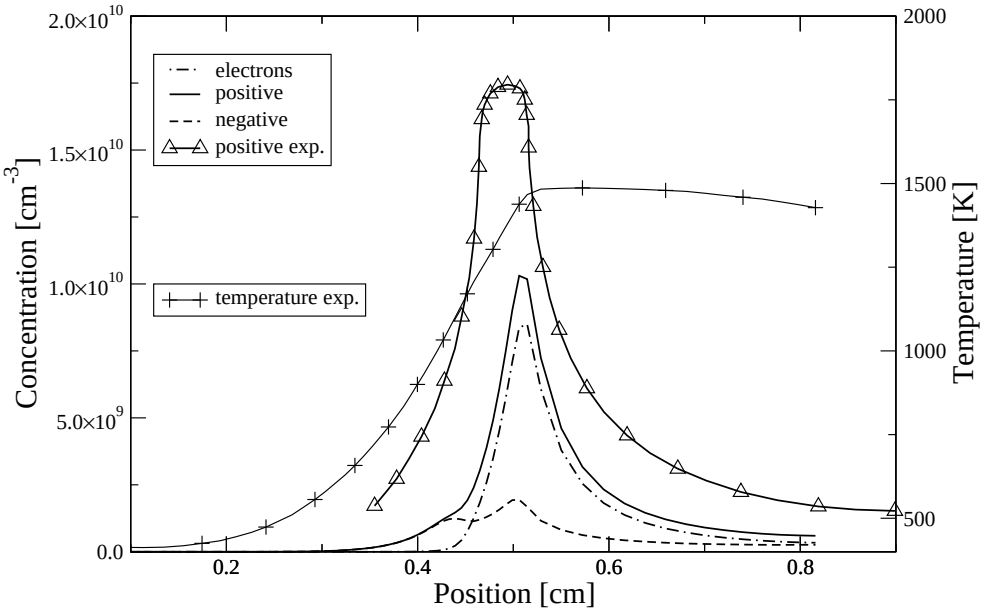

Figure 5.3: Total concentration of positive ions in comparison to the experiment of Wortberg [Wor65]. The measured temperature profile is also shown. The position and width of the ion peak is in good agreement with the experiment, while the total amount of positive ion concentration is underpredicted by a factor of 1.7.

pared to the simulation results. In their paper, Goodings et al. state that the upstream profiles would be broadened because of experimental issues, but do not estimate the amount of the broadening [GBN79b]. To get some more confidence in the simulation results, the flame of Wortberg [Wor65] is calculated and compared to the experimental data. In Figure 5.3 the experimental total positive ion concentration is shown. The advantage of this experiment is the availability of information about the local temperature. Here, the position and the width of the ion profile compares well to the experimental data. The absolute amount of positive ions is underpredicted by a factor of 1.7 similar to the findings for the experiment of Goodings.

Also, because the neutral species profiles agree well to the measurements, it is assumed that the species profiles of the ions in the experiment of Goodings are broadened to some extent. Therefore, the space coordinate will be scaled by a factor of 0.5 in the following figures to fit the numerical simulations better.

Overall, the simulations successfully predict the global concentration of charge carriers in the lean methane-oxygen flame studied.

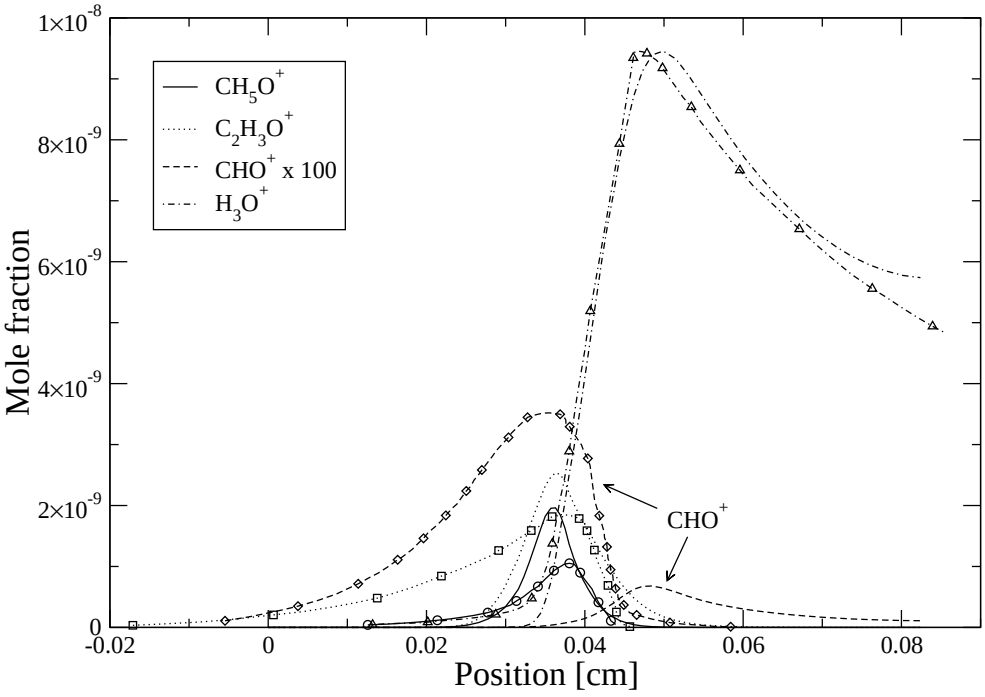

Figure 5.4: Mole fractions of the cations compared to the experimental results of Goodings et al. [GBN79a]. The data points (symbols) have been scaled to yield the same maximum H_3O^+ mole fraction. The space coordinate has been scaled by a factor of 0.5 to compensate the experimentally broadend profiles and shifted by 0.042 cm.

5.2.4 Species profiles

In Figures 5.4, 5.5, and 5.6 the individual species profiles are compared to the experiment of Goodings et al. Because ion currents are measured in the experiment instead of concentrations or mole fractions, the species profiles for the cations and anions are scaled by a common factor to yield the same maximum mole fraction of the main ion H_3O^+. The space coordinate cannot be compared to the simulation results, because the experimental origin of the coordinate system is chosen to be the local minimum in the pressure, while one of the model assumptions for the simulation is constant pressure. Moreover, the experimental species profiles are broadened to some extent as discussed above. For these reasons, the experimental data is scaled by a factor of 0.5 and shifted 0.042 cm to fit the simulation results best. This procedure is the same for the electrons, cations, and anions.

The results for the four cations CHO^+, CH_5O^+, $C_2H_3O^+$, and H_3O^+ are shown in Figure 5.4. With the exception of the ion CHO^+, all species profiles

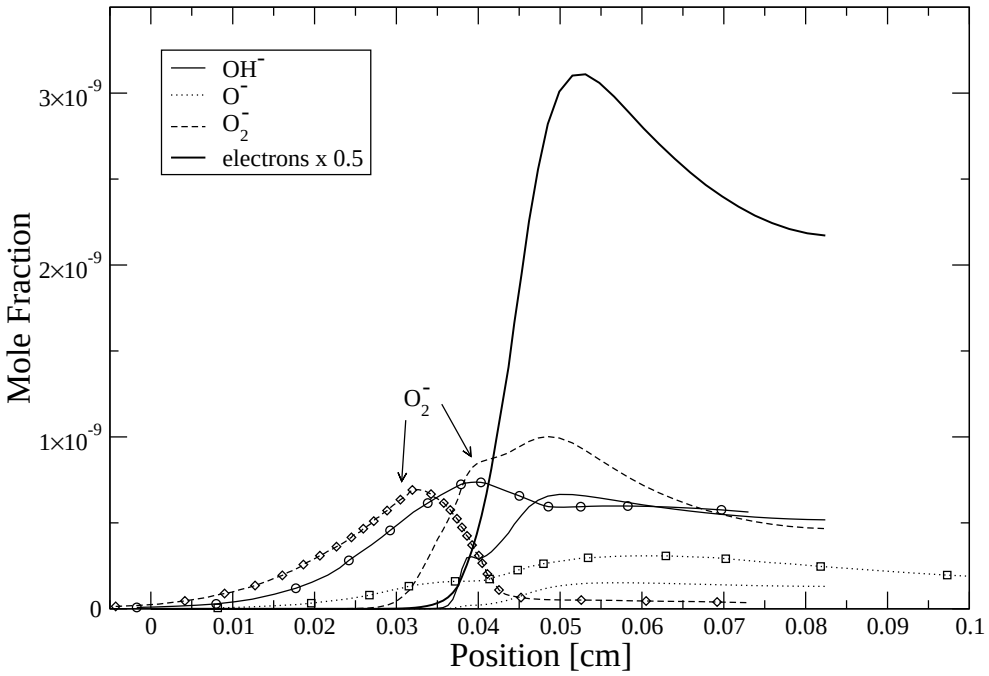

Figure 5.5: Mole fractions of the first group of anions compared to the experimental results of Goodings et al. [GBN79b]. The data points (symbols) have been scaled with the same factor and shifted the same way as discussed in Section 5.2.3.

agree well with the experimental results. One can clearly distinguish two regions in the flame: The species CH_5O^+ and $C_2H_3O^+$ maximize upstream but close to the reaction zone, while the burnt gas region is dominated by H_3O^+. The general behavior of this ion is reproduced well; its rise starts a bit later in the simulations, and its decrease in the hot gas is a bit slower. The maximum mole fraction of CH_5O^+ is overestimated by a factor of 1.8. Also in this case, the experimental profile starts earlier in the cold gas region; the situation is similar for the ion $C_2H_3O^+$. The simulation overestimates its maximum by a factor of 1.3, while its mole fraction in the upstream region is too small. Its decrease in the reaction zone is a bit too slow. Even though the mole fraction of the ion CHO^+ is very small, it is the species which initiates the whole pathway to the cations. Its abundance is smaller by a factor of five compared to the experiment. It also shows a maximum as in the experiment, but in the downstream region of the reaction zone. Overall, the results for the cations are satisfying, since the main features can be reproduced. Only the CHO^+ ion needs further investigations.

In Figure 5.5 the first group of anions is compared to the experiment. In addition to the electrons, the species O_2^-, O^-, and OH^- are shown. While the electron mole fraction is reproduced well, as shown in Section 5.2.3, the agreement

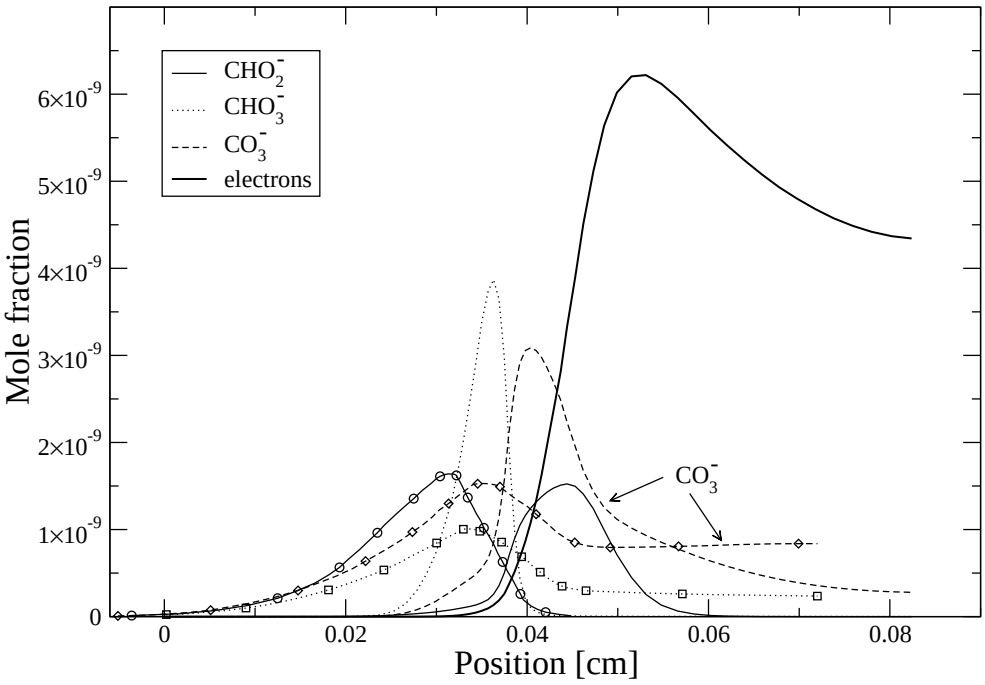

Figure 5.6: Mole fractions of the second group of anions compared to the experimental results of Goodings et al. [GBN79b]. The data points (symbols) have been scaled with the same factor and shifted the same way as discussed in Section 5.2.3.

for these anions with the experimental data is not as good as for the cations. In general, the abundances are reproduced well. O_2^- is predicted a factor of 1.4 too high, OH^- 9% too low, and O^- deviates around 50%. The general shape of the profiles is approximately reproduced for O^- and OH^-. In the case of the latter one, the rise in its mole fraction is too late, but the behavior in the burnt gas is reproduced well. The O_2^- profile rises a bit too late and persists in the burnt gas region, while the experimental data shows a sharp decrease in the reaction zone.

The results for the second group of anions (CHO_2^-, CHO_3^-, CO_3^-) are shown in Figure 5.6. While the maximum of CHO_2^- fits the experimental results, the maxima of CHO_3^- and CO_3^- are overestimated by a factor of 3.8 and 2, respectively. The CHO_3^- peak is at the right position, but it vanishes in the burnt gas region in contrast to the experiment, where it is still observed far downstream. The species CHO_2^- has a maximum with the proper mole fraction, but it occurs too late in the flame. Finally, the maximum of CO_3^- appears too late in the flame, and its mole fraction also decreases too fast in the burnt gas region compared to the experimental data, where it is the most abundant anion.

The simulation yields lower concentrations in the upstream region for all six

anions, as it was the case for the cations. Overall it becomes clear that the reaction mechanism of the anions has to be improved further. Unfortunately, especially for the most abundant negative ions in this flame, CHO_2^-, CHO_3^-, and CO_3^-, there is only little information available in the literature. This includes reaction pathways as well as the lack of quantitative kinetic data.

5.2.5 Variation of the temperature profile

In the experiments of Goodings et al., a simple cylindrical quartz burner is used. The flame has a conical shape with a base diameter of 4 mm and a height of 6.5 mm. The simulations instead solve the model equations for a flat flame. These flames have such an extended burner surface that edge effects can be neglected if measurements are done at the center perpendicular to the burner surface, so that a one-dimensional model can be used in the numerical simulations.

The main qualitative difference between the simulated flat flame and the conical one will be a different temperature profile caused by heat losses. If no temperature profile is provided, the simulations solve the conservation equation for the enthalpy of an adiabatic system. The resulting temperature profile is an upper limit of the expected experimental one. Unfortunately, no temperature measurement has been done in the experiment, so that the direct comparison with the simulation results have to be expected to deviate to some extent.

However, it can be seen in Figure 5.7 that most of the observed features of the ionic flame structure do not depend strongly on variations of the temperature profile.

The temperature profile which is obtained by assuming adiabatic conditions is reduced up to 13% in the burnt gas for this calculation, as is shown in the first subfigure, and kept fixed in the simulation. One finds some small changes at the cold side of the reaction zone, which are caused there by diffusion processes from the hot region where the temperature is varied. More H_3O^+ ions are produced in this hot region, even at this lowered temperature, because the electrons which would recombine with it remain bound to negative ions, especially to CO_3^-. The most sensitive property is the mole fraction of CO_3^- in the hot gas. The lowered temperature favors a higher mole fraction on the hot side of the flame. If one has in mind the high uncertainty in the thermodynamic data of this species, it turns out to be the species profile with the highest uncertainty if one compares the simulated flat flame results with a conical flame.

5.2.6 Influence of negative ions

In the lean flame of Goodings, negative ions occur in almost the same concentrations as the cations, especially in the cold regions of the flame. To discuss

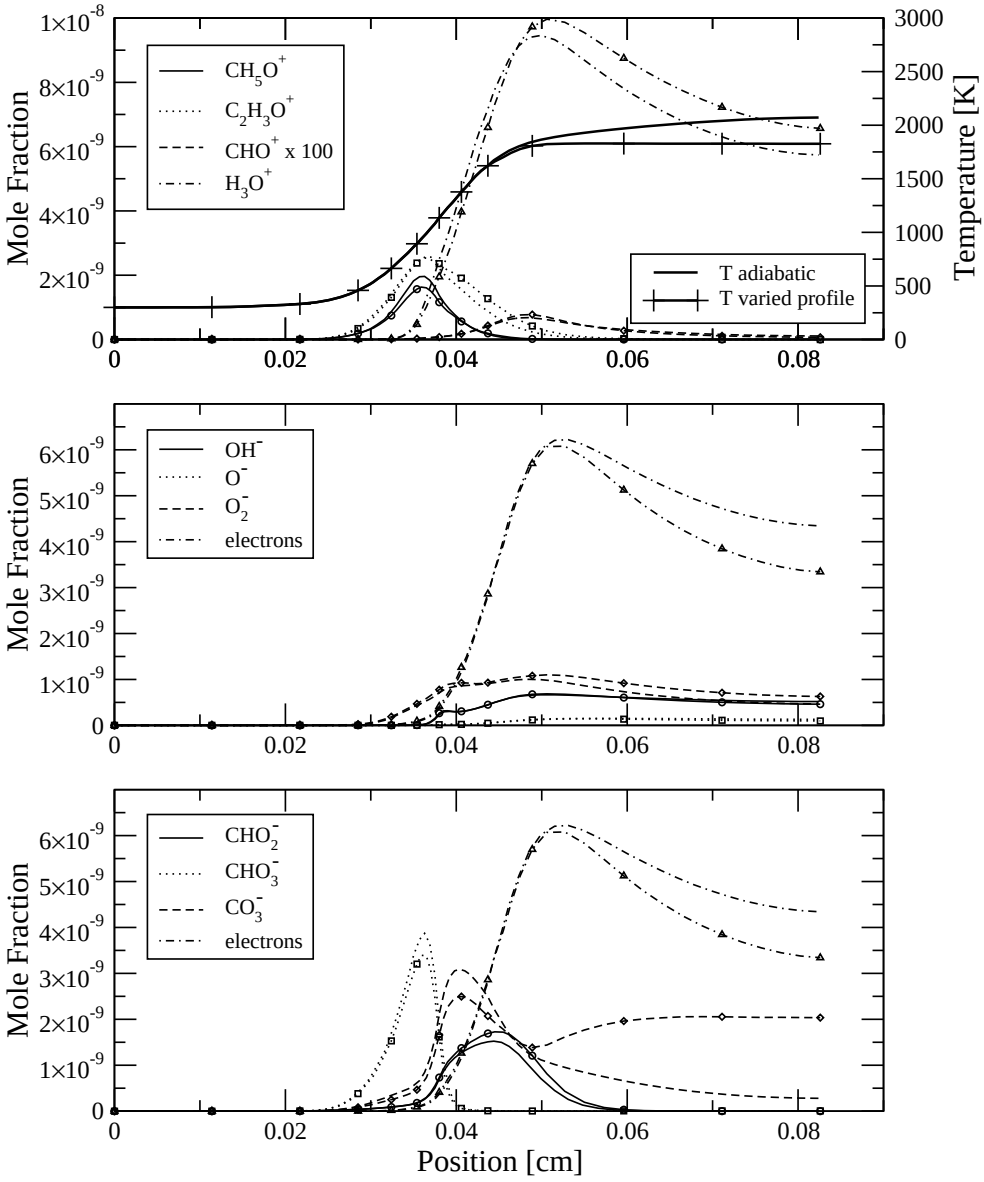

Figure 5.7: Changes in the simulated ion mole fractions if a varied temperature profile is used for the calculations. In the first figure, the calculated temperature (adiabatic assumption) and the varied temperature profiles are shown. The symbols are used for the mole fractions resulting for the changed temperature profile. The burnt gas abundance of CO_3^- is the most sensitive feature. The influence on the varied local temperature is small in the upstream region of the reaction zone.

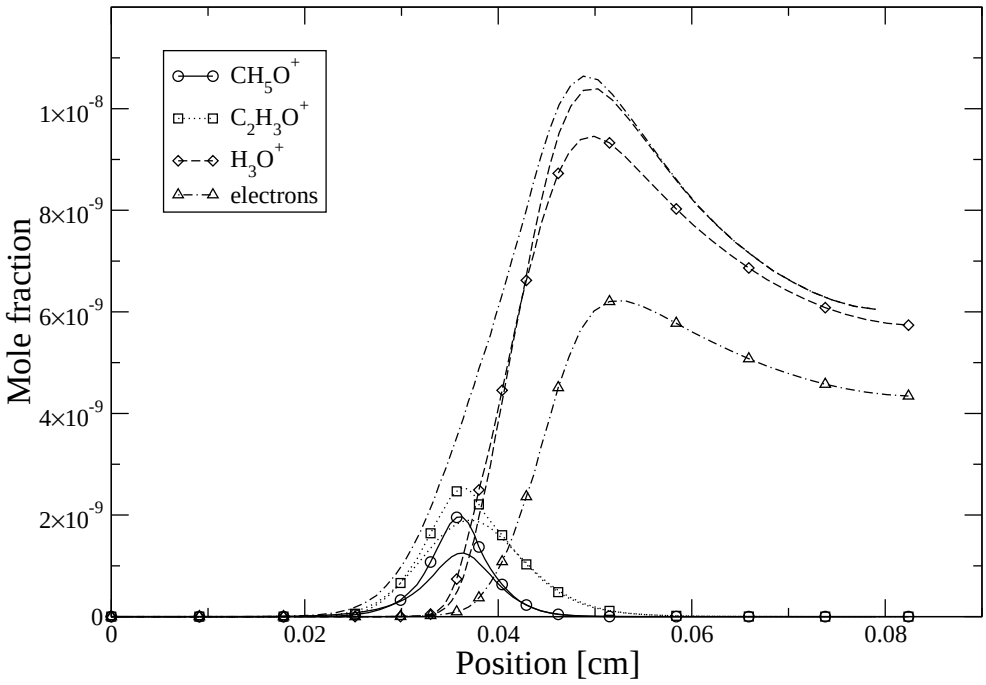

Figure 5.8: Species profiles of the important cations and the electrons in the flame of Goodings (with symbols) compared to a calculation (without symbols) in which all negative ions are excluded. When anions are included, the ratio between positive ion concentrations in the hot part of the flame compared to the cold part decreases. Shape and position of the cation profiles do not change significantly.

their influence on the profiles of the positive ions, simulation results are shown in which the anion part of the reaction mechanism is deactivated. This also helps to compare the obtained results with the simulations of Pedersen et al. [PB93], who neglect the anions in their work.

In Figure 5.8 the species profiles resulting, if only the three main cations and the electrons are included, are compared to the results when using the complete reaction mechanism. The most obvious difference concerns the electron mole fraction, which is increased by the amount of anions which would built up in the complete model. Therefore, the electrons occur earlier in the flame and are equal to the amount of H_3O^+ in the hot gas region. The profile of H_3O^+ is almost unchanged, only its maximum is increased by 10%. The position and shape of the other two cation profiles, which show a maximum in the reaction zone, change only slightly. Their maxima decrease by about 25% and 40%, respectively. The species CHO^+, which is not shown, changes only slightly.

Even though the cation profiles do not depend strongly on the inclusion of

negative ions in the model, they play an important role, because they bind the free electrons. This changes the electrical conductivity of the flame, see Equation 4.20. In the simulations it is found that only the electron term in the sum of Equation 4.20 contributes to the conductivity, even in the regions of the flame where the anions dominate and the electrons vanish. The situation is the same as for ambipolar diffusion, in which the electrons dominate the process because of their much higher diffusion coefficients. So the difference in the electron mole fractions in Figure 5.8 directly reflects the changes in the electrical conductivity, if the negative ions are neglected. The maximum local conductivity is about 2×10^{-3} A/Vm.

5.3 Chemical processes

The developed reaction mechanism consists mostly of reactions found in literature. If possible, only measured reaction rates are used. As could be seen from the results for the species profiles, parts of it need further improvement. This strongly depends on the availability of additional kinetic data.

The reaction mechanism is discussed is this section: First, the main reaction pathways are analyzed and compared to the qualitative picture given in the literature, followed by a discussion of reactions suggested in the literature, but for which no kinetic data is available.

5.3.1 Positive ions

It is widely accepted that the cation chemistry in the lean methane flame starts with the chemiionization reaction leading to the CHO^+ ion and an electron:

$$CH + O \rightharpoonup CHO^+ + E^- \quad . \tag{5.2}$$

Following Goodings et al., this first cation undergoes proton transfer reactions leading to the other most abundant ions observed in the flame. Sorted with respect to proton affinity, the following neutral species are relevant for the positive ions observed, see Table 3.2:

$$CO < H_2O < CH_3OH < CH_2CO \ .$$

According to this order, the ion CHO^+, i. e. protonated CO, is the least favorable, while $C_2H_3O^+$ is the thermodynamically most stable cation. This explains the relative abundances of the cations qualitatively, with the exception of the high H_3O^+ concentration in the burnt gas.

The reaction mechanism contains all possible proton transfer reactions between the cations. With the exception of the direct proton transfer from CH_5O^+ to CH_2CO, all these reactions are measured with an error of less than 25%. The kinetic rate is estimated according to the ADO theory for this missing reaction. However, it turns out that the results are not sensitive to this reaction in the flame.

The second important type of reactions is a number of electron recombination reactions leading to the dissociation of the cations. In the case of H_3O^+, these reactions have been measured in detail up to at least 1000 K. Measurements can also be found, but only up to 300 K, in the case of the other three cations. However, the temperature dependency is relatively small for the known reactions; the kinetic rate is reduced less than a factor of 2.6 at 2000 K compared to 300 K. These electron recombination reactions are supposed to be responsible for the slow decay of the H_3O^+ concentration in the burnt gas.

The third kind of reactions involve rearrangements of the cations. The most important one is the reaction of $C_2H_3O^+$ with the O atom to CHO^+. This reaction was suggested by Goodings [GBN79a] to explain the observed decrease of this ion in the reaction zone and the following rise of the H_3O^+ concentration. Proton transfer reactions alone are not able to reproduce this behavior, because the proton affinity of CH_2CO is much higher than that of H_2O.

Finally, there are ion-ion recombination reactions in the mechanism. Recombination of O_2^- and O^- with $C_2H_3O^+$ was already suggested in the literature [SSTS02]. No measurements could be found for these reactions. On the other hand, they are highly exothermic and are supposed to proceed almost with an universal rate constant. The inclusion of additional ion-ion recombination reactions is found to be important for the total amount of ions at the cold side of the reaction zone. Especially the reaction between $C_2H_3O^+$ and CHO_3^- reduces the magnitudes of the ion profiles in this region. Without these reactions, the ion peak at the cold side would be larger than the H_3O^+ peak downstream. But this is not observed in the experiments.

Reaction Flow

The simulation permits a quantitative discussion of the reaction mechanism. In Figure 5.9 the reaction flow between the cations resulting from the calculations is shown schematically. The arrows denote the main reaction pathways. Species symbols next to it represent the reaction partners, and the numbers close to the cations show the percentage of production resp. consumption of the ion. One has to keep in mind that this reaction flow analysis results from the spatially integrated chemical source terms, i. e. the kinetic rates, in the stationary flame. Additionally, the chemical rates of the forward and respective backward reactions

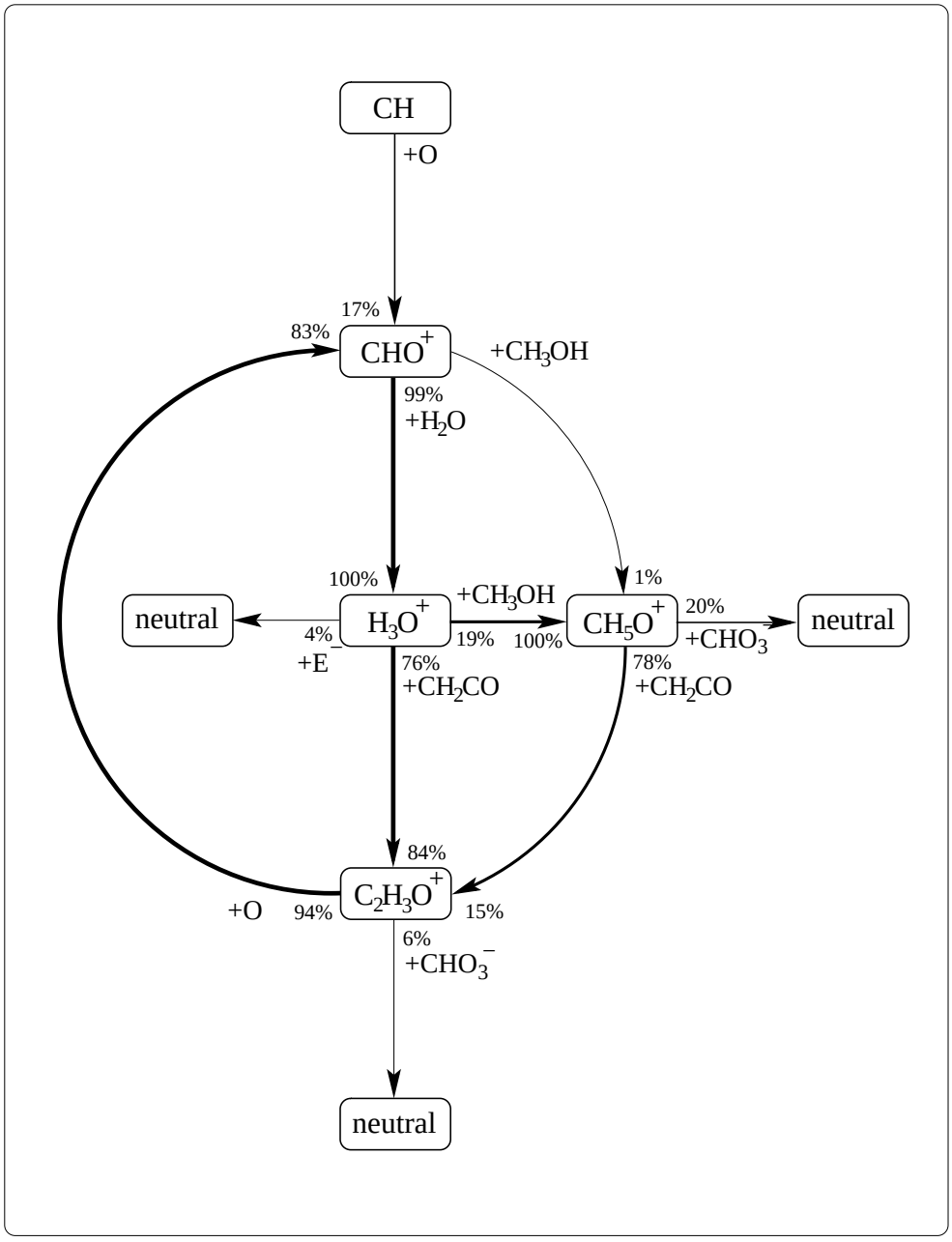

Figure 5.9: Schematic reaction flow for the cations in the lean methane-oxygen flame. The species symbols next to the arrows denote the reaction partners. The number close to the ion symbol gives the percentage of production resp. consumption of the particular species in this reaction. After the chemiionization reaction, the reaction flow is dominated by proton transfer reactions to neutral species with higher proton affinity.

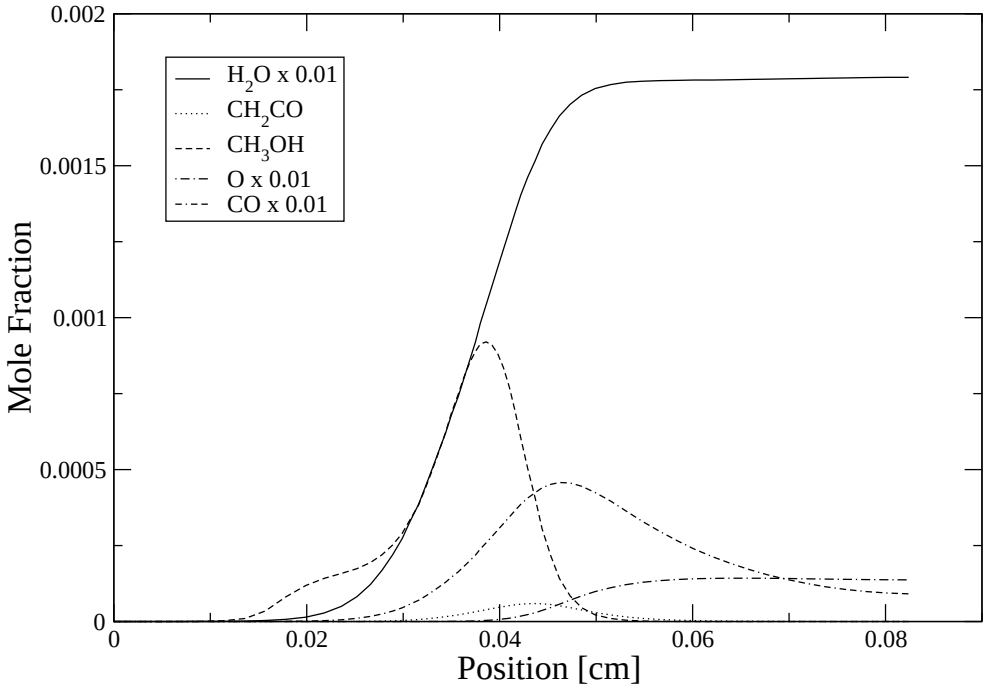

Figure 5.10: Mole fraction profiles of the neutral species relevant for the proton transfer reactions. The profile of the oxygen atom is shown in addition.

are summed to give an effective importance of a reaction.

The reaction flow analysis leads to the following picture of the chemical processes, see also Figure 5.10 showing the profiles of the relevant neutral species for this discussion: The chemiionization Reaction 5.2 leads to the first cation CHO^+ and free electrons. Goodings et al. suggest that this ion is produced where they observe the CHO^+ maximum in the experiment, i. e., on the cold side of the reaction zone, see Figure 5.4. But instead, the local reaction rates show that it is produced where the CHO^+ peak is located in the simulation, on the hot side of the reaction zone. The product of the CH and O concentrations has a maximum at this position. The H_2O concentration is already large in this region of the flame, so that CHO^+ transfers a proton immediately to it to yield H_3O^+.

The H_3O^+ ion starts to diffuse also to the cold side of the flame. On the way it transfers a proton to CH_2CO and CH_3OH. Both species profiles show a maximum in the reaction zone, see Figure 5.4. Even though the concentration of CH_3OH is the larger one, the majority of H_3O^+ is consumed to $C_2H_3O^+$. This is caused by the larger proton affinity of CH_2CO, so that the backward reaction is negligible in contrast to the situation for the proton transfer to CH_3OH. On the cold side of the reaction zone, CH_5O^+ also transfers a proton to CH_2CO, which increases the concentration of $C_2H_3O^+$ even more.

But proton transfer reactions alone are not able to completely explain the species profiles observed in the experiment. Because $C_2H_3O^+$ is the most stable protonated species, it would also be observed in the burnt gas region in high concentrations, while the experiments show that H_3O^+ is virtually the only cation in this region. Because of this reason, Goodings suggested reactions involving radicals of the reaction zone like O, H, or OH leading to H_3O^+ directly, or indirectly via CHO^+. The reaction flow shows that the reaction

$$C_2H_3O^+ + O \rightharpoonup CHO^+ + CH_2O \tag{5.3}$$

is an effective possibility for such a pathway. Similar reactions involving CH_5O^+, which have been suggested as well, do not seem to be necessary.

As can be seen from the reaction flow, the recombination reactions are important. For the H_3O^+ ion it is the recombination with electrons that dominates, while for the other two major cations the ion-ion recombination with CHO_3^- locally reduces the amount of ions in the flame.

Discussion

The discrepancy between the simulation results and the experimental data concerning the CHO^+ profile cannot be explained by simple proton transfer reactions between the cations in the model. As can be seen in Figure 5.1, the important neutral species CO and H_2O are well reproduced in the simulations. Furthermore, the important proton transfer reaction rates are measured with an error less than 25%. The thermodynamic data for the cations are also well known, especially for CHO^+ and H_3O^+. This leads to the conclusion that a pathway is missing in the mechanism which produces CHO^+ at the cold side of the reaction zone. This reaction has to have a high kinetic rate, since it has to compete with the very fast proton transfer reaction to H_2O,

$$CHO^+ + H_2O \rightharpoonup H_3O^+ + CO \quad . \tag{5.4}$$

The simulation results for the same flame obtained by Pedersen et al. [PB93] can be compared to the results in this work: The species profiles are also narrower than the experimental data in their calculations. The model includes the charged species H_3O^+, $C_2H_3O^+$, CH_3^+, C_3H_3, and CHO^+. The species profiles of H_3O^+ and $C_2H_3O^+$ are qualitatively similar to the results of this work. The main difference is that, in their model, the CHO^+ profile has a maximum at the same position compared to the experiment. The species CH_3^+ is included in their reaction mechanism, because it is the precursor of $C_3H_3^+$, which becomes important in rich flames. Both species occur in only very low concentrations in the lean flame of Goodings and were therefore not included in the model presented

in this thesis. But the proton transfer reaction from CH_3^+ to CO might explain the occurrence of CHO^+ in the cold region of the reaction zone, as observed in the experiment.

Following the recent compilation of ion-molecule reaction rates of Anicich [Ani03], the charge transfer from H_3O^+ to C_2H_2 does not occur with a rate higher than $6{\times}10^{12}$ cm^3/(mol s):

$$H_3O^+ + C_2H_2 \rightharpoonup C_2H_3O^+ + H_2 \qquad \text{with} \qquad k < 6 \times 10^{12} \text{ cm}^3/(\text{mol s}) \quad . \tag{5.5}$$

Therefore, this reaction is left out of the reaction mechanism in this work, but Pedersen et al. concluded that its backward reaction is the rate-limiting step in their overall ion reaction mechanism. As seen in this thesis, direct proton transfer from H_3O^+ to CH_2CO can also explain the species profile of $C_2H_3O^+$.

5.3.2 Negative ions

In comparison to the cation chemistry, much less is known about the reactions of the anions in flames. As can be seen in Section 3.1, most of the measured reaction rates stem from atmospheric chemistry and astrochemistry databases. If error estimates are available, they are much larger than for the cation reactions. A number of reactions are measured only at a temperature of 300 K. Only little information can be found especially on the ions CO_3^-, CHO_2^-, and CHO_3^-.

It is widely excepted that the first anion in a flame is O_2^-. Following the chemiionization Reaction 5.2, the electron is attached to oxygen molecules, which exist in high concentration even in the burnt-gas region of the lean flame. This is also the reason why a significant amount of anions exists even in the hot part of the flame. Following the discussion of Goodings et al., this oxygen anion leads to the other anions due to charge transfer reactions to neutral species with higher electron affinity. The relevant neutral species are listed here, sorted by increasing electron affinity; see Table 3.6:

$$O_2 < O < OH < CO_3 \leq CHO_2 \leq CHO_3 \ .$$

In addition, the following reactions of O_2^- with H or CH_4 were suggested to produce some secondary anions:

$$\begin{aligned} O_2^- + H &\rightharpoonup O^- + OH \\ O_2^- + H &\rightharpoonup OH^- + O \\ O_2^- + CH_4 &\rightharpoonup OH^- + CH_3 \quad . \end{aligned}$$

As in the case of the cations, proton transfer reactions were discussed as possibilities for the conversion of negative species. In this process a neutral molecule

HX donates a proton to an anion forming a new anion X^-. This reaction is exothermic if the new anion has a lower proton affinity than the old one. The expected order of anions with respect to proton affinity is shown here, see Goodings [GBN79b]. Also listed are the protonated counterparts:

$$OH^-/H_2O > O^-/OH > O_2^-/HO_2 > CHO_2^-/CHOOH \ .$$

This scheme shows, for instance, that the following reaction could be a direct way to the production of CHO_2^- from O_2^-:

$$O_2^- + CHOOH \rightharpoonup CHO_2^- + HO_2 \quad . \tag{5.6}$$

The pair of anions CHO_3^-/CO_3^- plays a special role, because they are not produced by charge-transfer reactions. Goodings suggests their formation by a reaction with HO_2 and their conversion by the species O_2, O, OH, or H:

$$CHO_2^- + HO_2 \rightharpoonup CHO_3^- + OH \tag{5.7}$$
$$CHO_2^- + HO_2 \rightharpoonup CO_3^- + H_2O \tag{5.8}$$
$$CHO_3^- + OH \rightleftharpoons CO_3^- + H_2O \quad . \tag{5.9}$$

In the burnt gas region, it is believed that CHO_3^- and CO_3^- are produced by three-body attachment of O^- and OH^- to CO_2 only:

$$O^- + CO_2 + M \rightleftharpoons CO_3^- + M \tag{5.10}$$
$$OH^- + CO_2 + M \rightleftharpoons CHO_3^- + M \quad . \tag{5.11}$$

Some of the species vanish in the reaction zone. This is believed to occur due to electron detachment after collision with a third body or after radical attachment.

The reaction mechanism used in this work is a compilation from many sources, see Section 3.1. If possible, only measured reactions are taken into account and, only in a few cases, reactions suggested in the literature are added with an estimated kinetic rate. The main reactions which were discussed by Goodings are included.

Primarily, the mechanism contains the electron attachment reactions to the electronegative species O_2, O, and OH. Especially for the most important one in the lean flame, the attachment to the oxygen molecule, there are many references which agree on the kinetic rate. This reaction is responsible for the amount of anions compared to electrons in the flame. Therefore it can be expected that this ratio is reproduced well.

If one has in mind that O_2^- is the first anion in the flame, the main charge-transfer reactions to OH and O are included. Respective reactions for the other anions are neglected, because no corresponding neutral species are included in

the reaction mechanism of the neutral species. Reactions leading from O^- to the more stable OH^- are included as charge-transfer reactions with rearrangement, most of them as proton transfer reactions as shown above.

As discussed by Goodings, collisional or associative detachment processes are supposed to consume the anions in the reaction zone and in the hot gas region. Collisional detachment, as the reverse reaction of the three-body electron attachment, is therefore also included for the species O_2^-, O, and OH. In addition, a large number of associative electron detachment reactions could be found in the literature. Most of them have been measured. They involve attachment of the radicals H, O, CH, and other main neutral species.

The situation is more complicated for the species CHO_2^-, CHO_3^-, and CO_3^-. For direct electron attachment and charge transfer reactions, the corresponding neutral species are not included in the reaction mechanism, because they are not important for the chemistry of neutral species in a methane flame. The proton transfer Reaction 5.6 is omitted for the same reason. Instead, CHO_2^- is produced as suggested by Calcote from OH^-, and from O^- by rearrangement reactions. As proposed, its consumption is done by electron detachment after reaction with the H atom. CO_3^- and CHO_3^- are built by three-body attachment of O^-, resp. OH^- to carbon dioxide. Moreover, two reactions were measured which consume CO_3^- by radical attack of H and O.

Finally, it is necessary to include ion-ion recombination reactions between the most abundant charged species in the flame. Otherwise the amount of ions on the cold side of the reaction zone would be too high compared to the experimental results.

Reaction flow

In this section, the reaction mechanism of the anions is analyzed to see which reactions are important and which pathways are taken in this lean methane-oxygen flame. Even if the anion species profiles have to be improved, as could be seen in Section 5.2.4, this analysis gives important information for the discussions.

In Figure 5.11 the results of the reaction flow analysis are shown. Only reactions which contribute more than 10% to the production or consumption of a species are included. As for the cations, the number close to the species symbols gives this contribution, while the reaction partner is shown along the arrow. Some reactions act as production and consumption channels depending on the position in the flame.

The reaction flow leads to the following picture: The electrons are produced by the chemiionization Reaction 5.2 in a small region on the hot side of the reaction zone, afterwards they diffuse in the upstream and downstream direction. On their way, they are attached to O_2. In this process, water is more effective as

a third-body than the very abundant oxygen molecule. Attachment to OH and O is not important. On the cold side of the reaction zone, associative detachment reactions of O_2^- with H and H_2 are active.

In the reaction zone and the hot gas, the oxygen anion O_2^- leads to the formation of O^- by charge transfer and OH^- by reaction with H atoms. These two species mainly undergo associative electron detachment reactions. While O^- reacts with CO, OH^- is attacked by H and O in the reaction zone and in the burnt gas region. OH^- is also consumed in the reaction zone by OH to form O^-. The channel to CO_3^- is the second consumption process for O^- and the only way in which this species is produced. CO_3^- is mainly consumed by O attack to O_2^-, but partly also by H attack to OH^-.

The two remaining species, CHO_2^- and CHO_3^-, couple weakly to the anion chemistry. They are products of O^- and OH^-, respectively. CHO_2^- is produced in the reaction zone by CH_2O and partly by CHO. Both species maximize there, but CH_2O has a much higher concentration. It is consumed in the reaction with H in which an electron is detached. The species CHO_3^- originates from attachment of OH^- to carbon dioxide. As third bodies, the oxygen molecule and water are considered. This fast reaction is responsible for the production as well as for the consumption of CHO_3^- depending on the position in the flame. In the cold part it is produced, while after its maximum it is consumed by collisions with a third body. Finally, because of the high concentration of CHO_3^- at the cold side of the reaction zone, it is consumed by ion-ion recombination with the most abundant cations in this region, which are $C_2H_3O^+$ and CH_5O^+.

Discussion

As can be seen from the simulation results of the anion profiles, see Figure 5.5 and Figure 5.6, the reaction mechanism of the anions needs further improvement. The species O^- and OH^- agree qualitatively with the experimental data. In the following discussion, the upstream region including the reaction zone will be considered first, and the species profiles in the burnt gas will be discussed afterwards. The reaction paths for the species CHO_2^-, CHO_3^-, and CO_3^- which were suggested in the literature are shown in Figure 5.12. Thick lines denote the reactions included in the reaction mechanism. In addition, the reactions which are tested and discussed are shown with dotted lines.

The species CHO_3^- has a maximum at the correct position. CO_3^- reaches its maximum too late in the flame. A possible solution would be a pathway from CHO_3^- to CO_3^-, because their profiles behave almost identically in the experiment. Some proton transfer reactions with OH, O, and O_2 have been suggested, but no measurements are available, see Reaction 5.9. If this reaction is added to the model using the ADO theory for the kinetic rate, it leads to a high CO_3^-

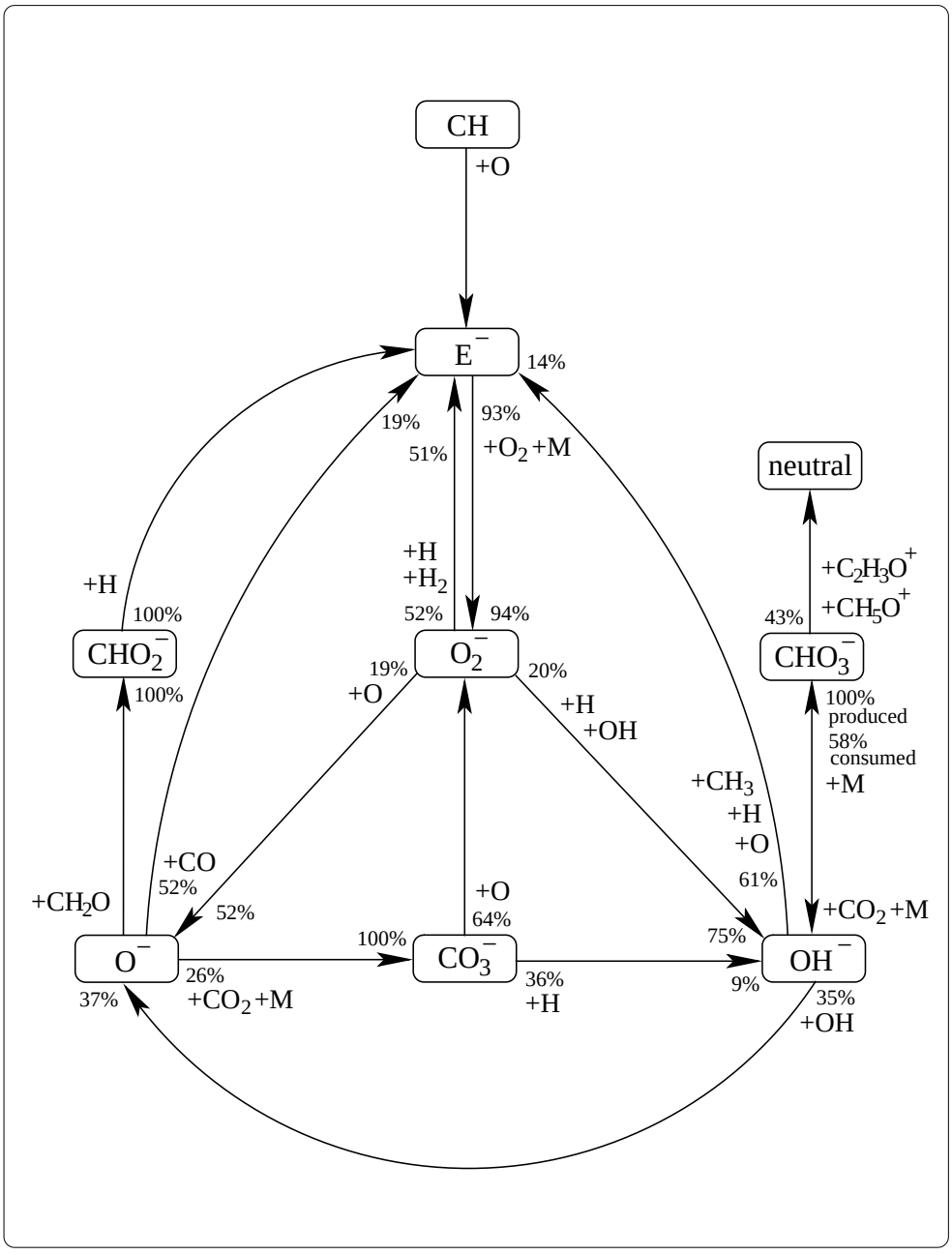

Figure 5.11: Schematic reaction flow of the anions in the lean methane-oxygen flame. The species symbols next to the arrows denote the reaction partners. The numbers close to the ion symbols give the percentage of production resp. consumption of the particular species in this reaction.

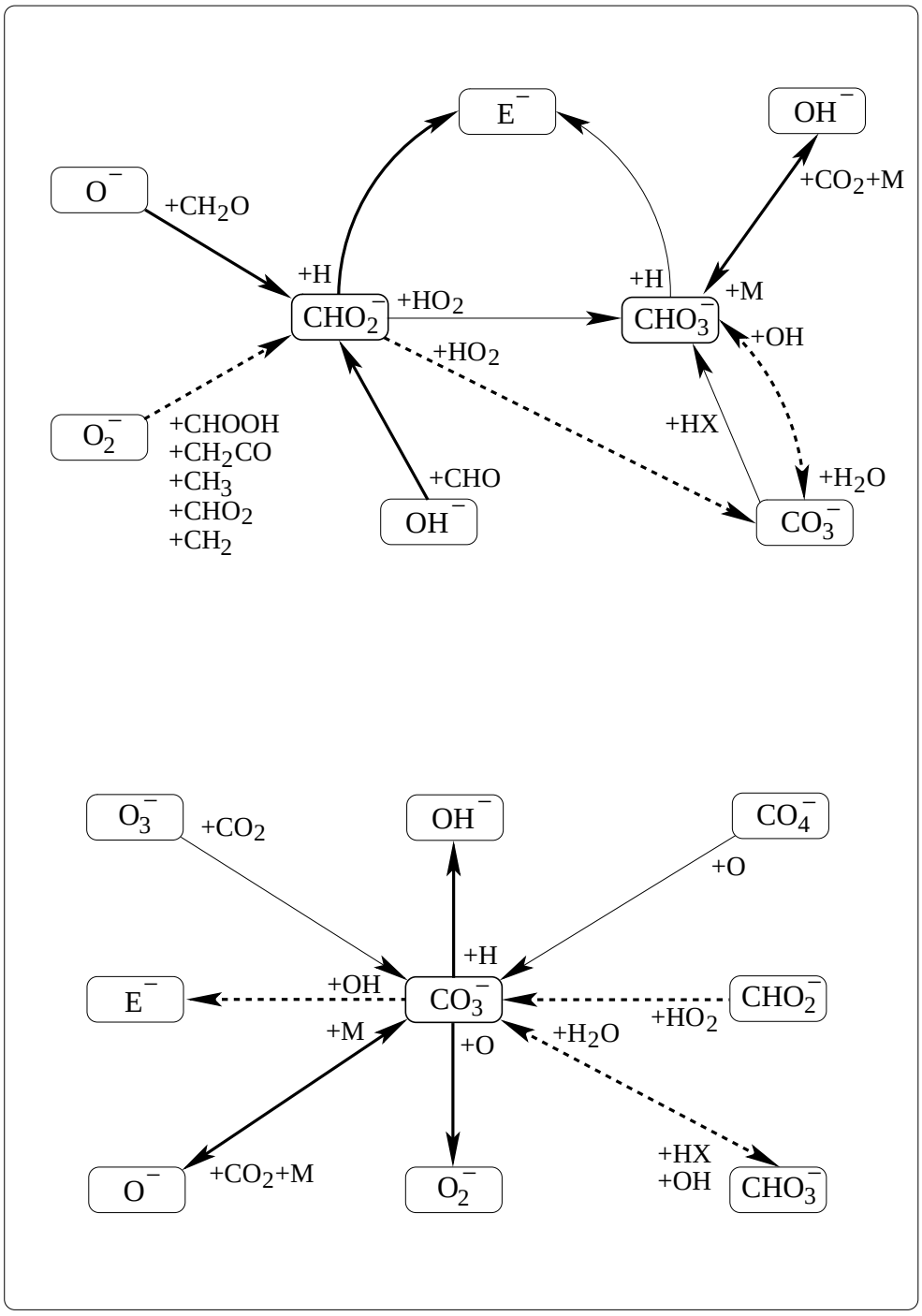

Figure 5.12: Schematic chart of the suggested reactions leading to the formation of CHO_2^-, CHO_3^-, and CO_3^-. The reactions included in the reaction mechanism are marked by solid lines. The reactions which are tested are designated by dotted lines; see the discussion in the text.

peak at the position of CHO_3^- which is reduced to 30%. On the other hand, the pathway from O^- to CO_3^-, which is responsible for the late CO_3^- peak, has been measured, so that it is likely that an additional consumption reaction for CO_3^- is missing. Associative electron detachment has been suggested to achieve this. As an example, the following reaction has been suggested to proceed with a rate coefficient of 3×10^{11} cm^3/(mol s):

$$CO_3^- + OH \rightharpoonup CO_2 + HO_2 + E^- \quad . \tag{5.12}$$

However, the calculation shows that it does not reduce the CO_3^- concentration significantly.

The species profile of CHO_2^- has a maximum, but much too late in the flame. In the experiment, it appears as the first anion in the upstream region. In the reaction mechanism, it is produced from O^- but this reaction is uncertain in its rate coefficient, because it has also another channel and no branching ratio is given. Only the total rate was measured. However, a variation of this branching ratio does not influence the position of the CHO_2^- significantly. A number of other reactions were suggested that produce CHO_2^- from O_2^-. They include reactions with CH_3, CH_2, CHO_2, CH_2CO, and HCOOH. Among them, only the reaction with HCOOH has been measured. The two neutral species CHO_2 and HCOOH are not included in the reaction mechanism, so that these two pathways cannot be tested. The simulations show that all other reactions produce CHO_2^- in high concentrations, but the position downstream of CHO_3^- remains. The pathway from OH^-, which is responsible for the CHO_3^- profile, does not contribute because of the low CHO concentration.

The ion chemistry in the burnt gas region is supposed to be simpler because only the main neutral combustion products persist there. The simulations show that the total amount of charges decreases correctly, but the contributions of the individual anions only agree for O^-, OH^-, and CHO_2^-. Compared to the experimental results, O_2^- still remains in the burnt gas at the expense of the species CHO_3^- and mostly CO_3^- which were measured in higher concentrations in this region.

As suggested by Goodings, the three-body attachment of O^- and OH^- to carbon dioxide does not explain the high CO_3^- and CHO_3^- concentrations in the experiment. Instead, the backward reactions consume these species at the high temperatures in this region. This can be seen in the reaction flow diagram, but also from calculations of the chemical equilibrium for the single reactions: All following values are obtained with a standard enthalpy of formation for CO_3^- of -480 kJ/mol. The attachment of O^- to carbon dioxide is exothermal with a reaction enthalpy of -188 kJ/mol:

$$O^- + CO_2 + O_2 \rightharpoonup CO_3^- + O_2 \quad . \tag{5.13}$$

The ratio between the concentrations of CO_3^- and O^- is very large in thermodynamic equilibrium at the conditions in the upstream region of the flame, but approximately $6{\times}10^{-4}$ at the hot boundary of the calculations. In the experiment this ratio is roughly 0.5,

$$\frac{[CO_3^-]}{[O^-]} = [CO_2] \left(\frac{A}{A^{-1}}\right) \exp\left(+\frac{182.6\,\mathrm{kJ/mol}}{RT}\right) \quad , \tag{5.14}$$

where the concentration of CO_2 has the unit mol/cm^3. The situation is similar for the attachment of OH^- to carbon dioxide. The ratio of CHO_3^- to OH^- reaches its minimum value of $3{\times}10^{-3}$ at the hot boundary of the flame simulation. At this position, the experiment gives a value of 0.4.

Other direct pathways, like the reaction with carbon dioxide from O_2^- to CO_3^- and CHO_3^-, involving species which exist in the hot gas do not seem to be possible. Reactions connecting CHO_3^- and CO_3^- have been suggested in the literature. Some examples are

$$\begin{aligned} CHO_3^- + OH &\rightharpoonup CO_3^- + H_2O \\ CO_3^- + HX &\rightharpoonup CHO_3^- + X \quad , \end{aligned}$$

with OH and HO_2 as HX. These three reactions consume CO_3^- in the hot gas region. Thus, some additional pathway to CHO_3^- could lead to higher concentrations of both ions in the burnt gas. In the case of CO_3^-, electron attachment reactions could be important.

In atmospheric chemistry it is known that CO_3^- is produced from O_2^- and O^- through the intermediate species O_3^- and CO_4^-. However, from the thermodynamic point of view, these pathways should again rather consume these species at the high temperatures in the burnt gas region.

All these discussed reactions could lead to higher concentrations of CO_3^- and CHO_3^- in the burnt gas, but they have to compete with the very fast collisional detachment reactions. Therefore, the enthalpy of formation for CO_3^- is lowered in the simulations to examine, if the uncertainty in this value could explain the low concentrations in the burnt gas. However, the results show that this is not the case.

Finally, it has been shown in Section 5.2.5 that variations in the temperature profile have the highest influence on the CO_3^- concentration in the burnt gas. The local flame temperature and other differences between the conical flame in the experiment and the simulated flat flame could also be responsible for the deviations of the charged species profiles in the burnt gas region.

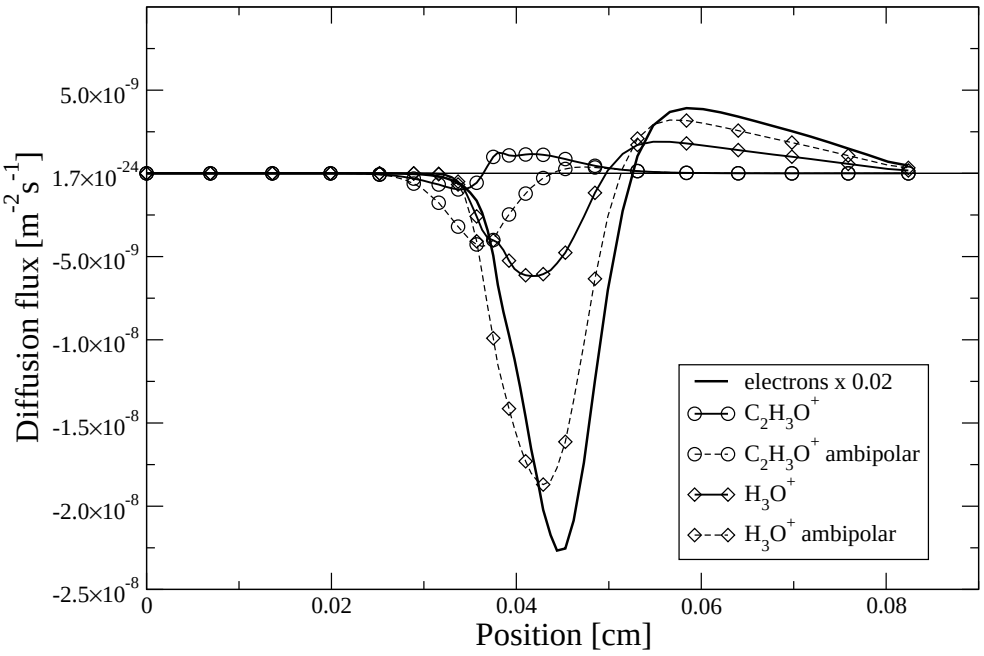

Figure 5.13: Diffusion fluxes of important cations in the flame of Goodings et al. Results following Fick's law (lines) are compared with ambipolar diffusion fluxes (dotted). In addition, the free electron diffusion flux is shown.

5.4 Influence of charged species diffusion

In order to understand the role of ambipolar diffusion, the diffusion fluxes of some important ions resulting from the simulation of the flame of Goodings are shown in the Figures 5.13 and 5.14. For each species, the results of the model including ambipolarity, as discussed in Chapter 4, are compared to that of Fick's law of diffusion, which is used for the uncharged species. Because of the dominating role of the electrons, their diffusion flux is shown in both figures. It is important to notice the different scales for the electrons.

As expected, the electrons would diffuse much faster without ambipolarity. The shape of the flux along the flame reflects the gradient of the electron mole fraction, which has a maximum at approximately 0.053 cm. As is shown in Chapter 4, ambipolarity can be viewed as a correction of the diffusion fluxes in which the total charge flux is compensated by all charged species to become zero, depending on their concentrations and abilities to diffuse (see Equation 4.11). Because the electrons have a diffusion coefficient which is two to three orders of magnitude larger than for the heavy ions, effectively they alone are responsible for the non-vanishing total charge flow.

This can be seen in the Figures 5.13 and 5.14, if one compares the free dif-

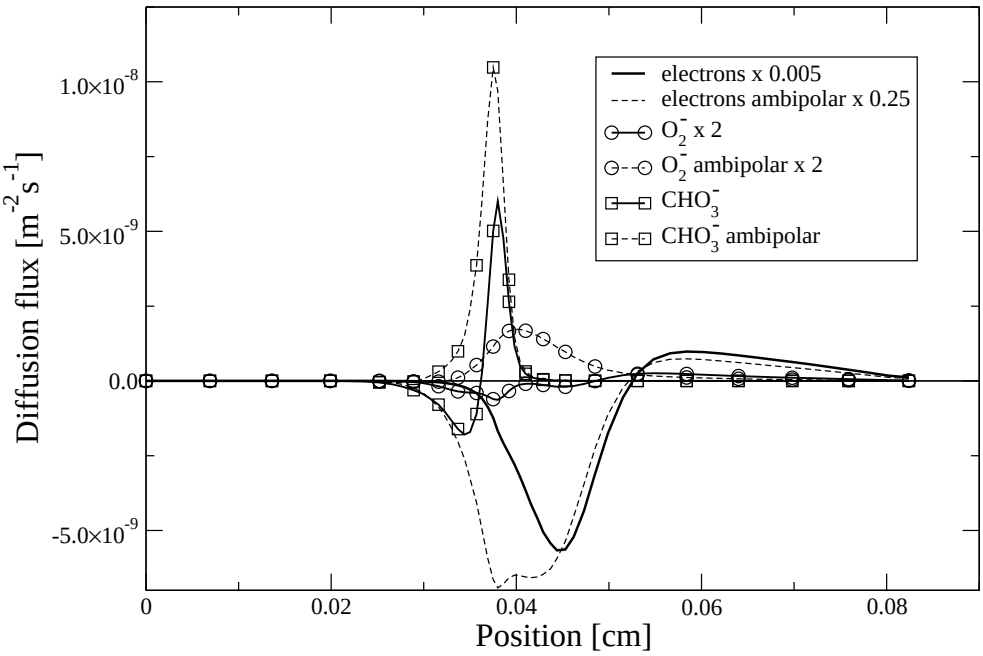

Figure 5.14: Diffusion fluxes of important anions in the flame of Goodings et al. Results following Fick's law (lines) are compared with ambipolar diffusion fluxes (dotted).

fusion fluxes and the ambipolar fluxes. The correction to the free fluxes has the same direction as the electron diffusion for the cations, i. e., they follow them to maintain charge neutrality. The same holds for the anions, which diffuse opposite to the electrons. In general, the correction is comparable or even larger than the free diffusion itself. Furthermore, the qualitative features are changed, so that diffusion is not related to the gradient of the individual species mole fractions anymore. This shows clearly the significance of ambipolar diffusion.

Figure 5.13 shows the diffusion fluxes of the two cations $C_2H_3O^+$ and H_3O^+. The concentration of $C_2H_3O^+$ has a maximum at 0.036 cm. Therefore, its free diffusion flux changes its sign at this position. Ambipolarity leads to a completely different behavior; diffusion is highest at the point of the maximum concentration.

Like a convection term, ambipolar diffusion pushes the complete $C_2H_3O^+$ profile to the cold side of the flame to follow the electrons. The situation is different for H_3O^+. Because it has a similar concentration profile as the electrons, the ambipolar correction has the same qualitative behavior as the free diffusion expression. Effectively, the diffusion of H_3O^+ still follows Fick's law, but with a higher diffusion coefficient. This observation can be shown to be true in general, if only electrons and one type of positive ions are regarded in the model. In

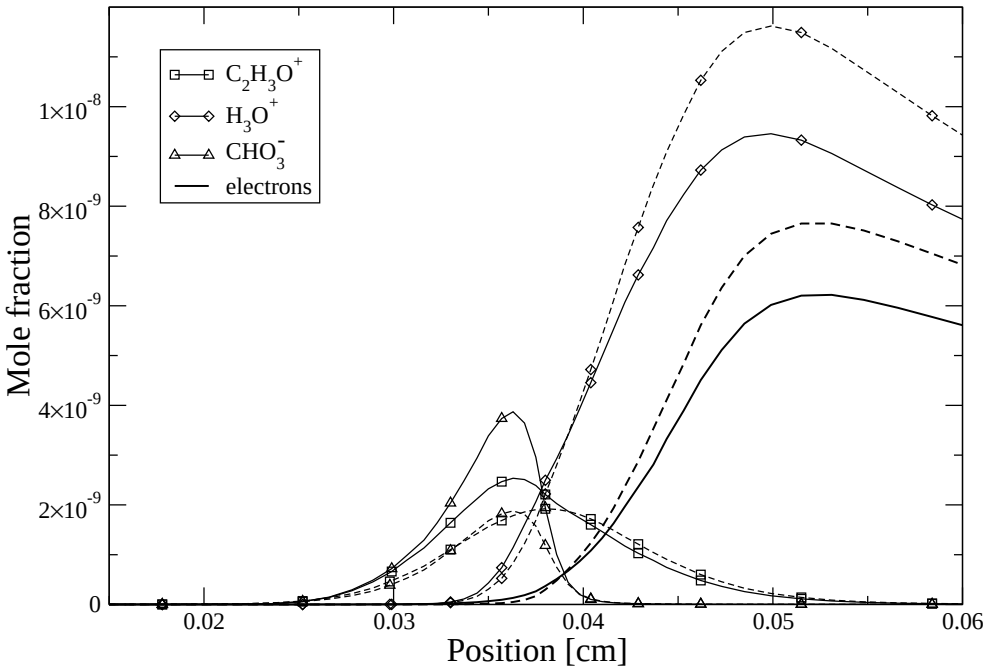

Figure 5.15: Comparison of major species profiles for the flame of Goodings after changing the way in which ambipolar diffusion is calculated. Solid lines show the results for the complete model, while dotted lines are used for the simplified model. The main effects of the complete model are the transport of ions to the cold side of the flame and the steepening of the species profiles there.

this situation, one can show that the cations diffuse with an effective ambipolar diffusion coefficient twice that one without ambipolarity; see for instance [MM73]. This special case is included in the model equations, as can be seen from H_3O^+ in the hot gas region, where it is the only dominating cation.

As for the cations, Figure 5.14 shows the diffusion fluxes for two important anions, i. e., CHO_3^- and O_2^-. The results for the electrons are shown again, this time also with their ambipolar diffusion fluxes. Ambipolarity slows the electrons down, while the qualitative diffusion behavior remains. The different scaling factors in the figure should be noticed. The two anions CHO_3^- and O_2^- behave qualitatively in the same way. Very similar to the cation $C_2H_3O^+$, their free diffusion is altered in a way that ambipolar diffusion acts like a convection process. Both species are pulled towards the hot side of the flame. The usual diffusion behavior, which would broaden the species profiles, is slowed down.

To obtain some more insight into the role played by the ambipolar diffusion, a calculation is performed in which a simplified diffusion model is used. Following this, the diffusion coefficients of the heavy ions are multiplied by two. But except

from this change, they diffuse like they would without ambipolarity, depending on the gradient of their mass fractions. The diffusion flux of the electrons is then calculated to compensate the charge separation caused by the diffusion of the heavy ions. This model is not valid in general, but it is approximately applicable in the hot region of the flame. It is used here for the discussion only, because it preserves charge neutrality, and the heavy charged species diffuse following Fick's law. The outcome of this comparison is shown in Figure 5.15. It gives the species profiles of the major ions obtained with both models of diffusion.

First of all, it is surprising that the rough changes in the diffusion model lead to relatively small changes in the species profiles. This suggests that the ion distribution along the flame is mostly determinded by the chemical processes rather than by the details of diffusion.

The most obvious difference is the increased ion concentration in the hot part of the flame. The diffusion flux shows that less electrons diffuse into the cold region. Also the H_3O^+ ions do not have to follow the electrons in the changed model so that – overall – these two species reach higher concentrations in the hot part of the flame. The species $C_2H_3O^+$ occurs in lower concentration than before. This is caused by the reduced amount of H_3O^+ reaching the cold region, having in mind that $C_2H_3O^+$ is a product of H_3O^+. It is more interesting that its position is also shifted to the hot side of the flame. This is caused by the changed diffusion process, because diffusion only broadens the species profiles in the simplified model, while in the complete model diffusion is directed to the cold side of the flame. Also the amount of CHO_3^- is reduced. This is partly because less electrons reach the cold side, but also because the diffusion towards the hot side is missing in the simplified model.

Sensitivity to diffusion coefficients

The comparison between the two diffusion models also suggests that the results of the simulations will not be very sensitive to the uncertainties in the diffusion coefficients of the ions resulting from the estimations in lack of measured data, as discussed in Section 3.3.

To investigate the dependence of the species profiles on the diffusion coefficients, a number of calculations are performed in which the diffusion coefficient of one charged species in the gas mixture is doubled, while all other coefficients are unchanged. These simulations show that the variation of the diffusion coefficients of the electron, CHO^+, and O_2^- has virtually no effect on the species profiles. The electrons are slowed down to the speed of diffusion of the heavy charged species, and CHO^+ reacts very fast to H_3O^+ so that diffusion can be neglected. The diffusion coefficient of the most abundant ion H_3O^+ has by far the highest sensitivity. The species profiles resulting after doubling the diffusion

coefficient are shown in Figure 5.16. The main effect is an increase in all ion concentrations at the cold side of the reaction zone at the cost of the ion concentrations in the hot part, which are decreased. This is the result of the increased diffusion of H_3O^+ and electrons into the cold part, from which all other ions are produced. The increased diffusion flux of H_3O^+ results from the free diffusion part in accordance to Fick's law, but also because of ambipolarity, as this species can follow the electrons more easily, if its diffusion coefficient is increased. As shown in Chapter 4, the electrons have roughly an effective diffusion coefficient twice that one of H_3O^+ as the dominating cation in the hot gas region; see Equation 4.17. Doubling of the other diffusion coefficients causes no changes in the species mole fractions larger than 10%.

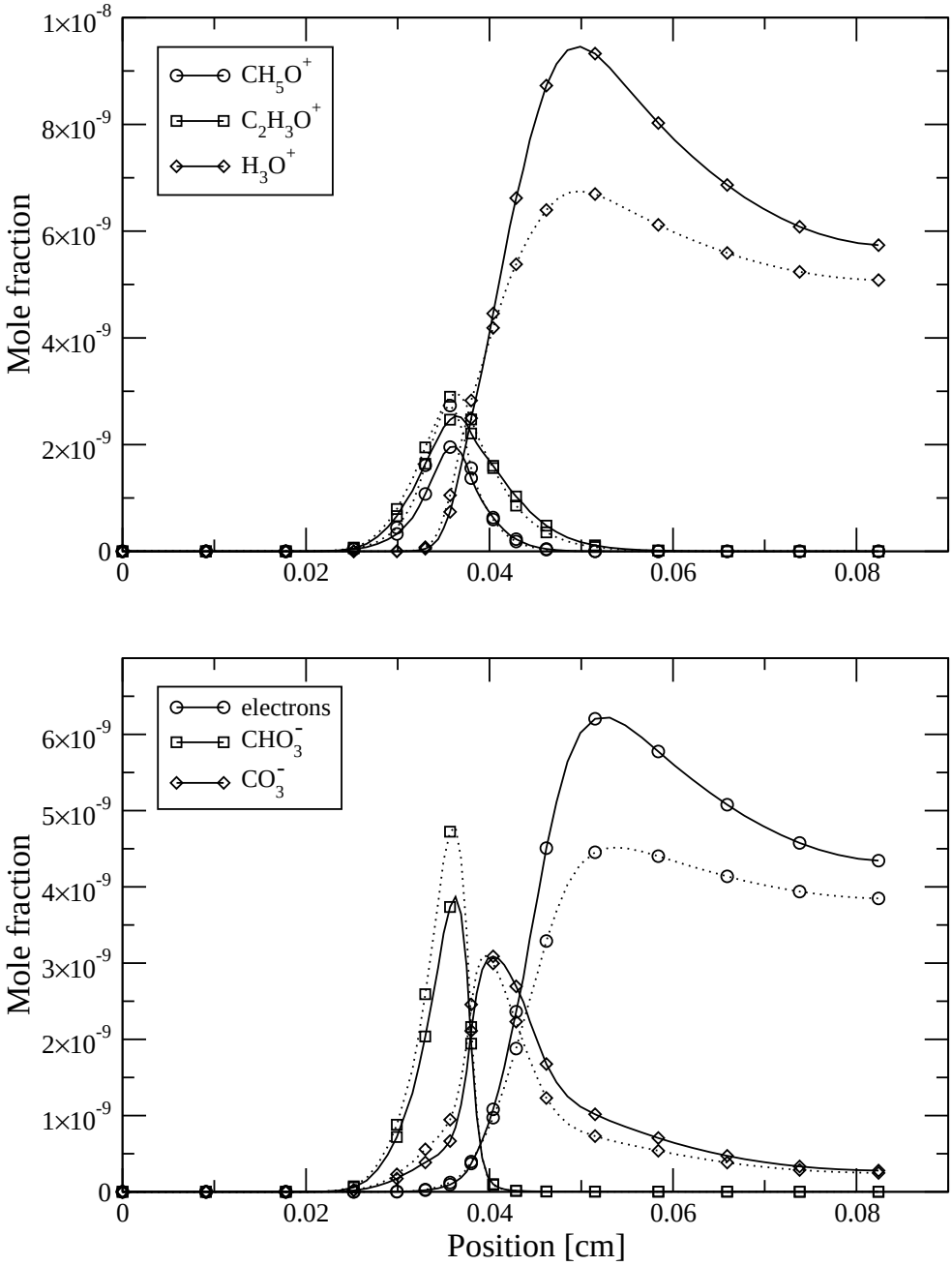

Figure 5.16: Comparison of major species profiles for the flame of Goodings after increasing the diffusion coefficient of H_3O^+ by a factor of two. Same symbols correspond to the same species. Dotted lines show the results with changed diffusion coefficient. This diffusion coefficient has the highest influence on the species profiles. An increase leads to an increase of charge concentrations at the cold side of the reaction zone at the expense of a decrease in the burnt-gas region.

Chapter 6

Conclusions

In this work, numerical simulations of charged species concentrations along a premixed flat methane-oxygen flame have been presented and compared to experimental results. For the first time, negative ions were also included in the model. Species diffusion and chemical reactions were considered by detailed submodels.

To achieve this, a reaction mechanism for ion-molecule and ion-ion reactions had to be developed. Moreover, the model for the diffusion processes needed to be extended to take into account the ambipolarity of charged species diffusion, if negative ions are present. Molecular data for species collisions and thermodynamic properties had to be provided. Finally, the simulation tool MIXFLAME, which has been used for the numerical calculations, was modified to be able to include charged species in the model. This implied changes to the differential equations because of the diffusion processes, but also its coupling to the TRAPLA program, which calculates the properties of all species and of the ionized gas mixture, i. e., thermodynamic values, heat conductivities, and diffusion coefficients. This has been implemented as a flexible library.

The reaction mechanism has been obtained from different sources from the literature. As charged species, the 11 most abundant ions observed in the experiment were included. As far as possible, only measured reactions were accepted in the database. The main aim was the discussion and quantitative evaluation of the reaction mechanism, as it was available in the literature. Reaction pathways suggested in previous publications were tested, and reaction flow analyses were shown. The comparison with experimental data showed that the overall charge distribution along the flame can be reproduced well. This includes positive ions, the electrons, as well as the negative ions, which prove to be important in fuel-lean flames. It is confirmed that they occur in concentrations equal to positive ions in the cold side of the reaction zone and still in a significant amount in the burnt gas. Their inclusion in the reaction mechanism has only little influence on

the cation distributions in the flame, but negative ions are found to be important, because they reduce the amount of free electrons. Therefore, the electrical conductivity, which is of high importance for applications, would be overestimated considerably without negative ions in the model.

The simulated species profiles of the cations agree reasonably well with the experimental data. Only the position of the CHO^+ occurrence has to be improved by adding additional charged species and reaction pathways to the mechanism. The calculations also show that the reaction mechanism of the anions is still not complete and has to be further improved. Even though qualitative agreement is found for many features of the species profiles, certain properties cannot be explained by the measured reactions only. Furthermore, some suggested reactions were ruled out. The reaction flow analysis showed the pathways taken by the chemical system.

The second focus of this work was the extension of the model for diffusion of charged species in the flame. The concept of ambipolarity, which leads to a vanishing total charge flux, was formulated in a general way for a gas mixture containing electrons, several positive and negative ions. The equations were discussed in the limit of dominating electron diffusion, which was shown to be valid in the flame even in the regions where negative ions occur in much higher concentrations.

In the third part, the influence of ambipolar diffusion on the charged species profiles was studied for the methane-oxygen flame. It was shown that the contribution of ambipolarity to the total diffusion flux is significant; often it even exceeds the free-diffusion flux following Fick's law. Because the electrons, with their high mobility dominate the diffusion process, the cations and anions have to compensate the charge separation caused by electron diffusion. Therefore, the cations diffuse in the upstream direction, while the anions diffuse in the downstream direction of the flame. This is the reason why ambipolarity mainly increases the ion concentrations on the cold side of the reaction zone, while the ion concentrations on the hot side are decreased. Moreover, it was found that the charge distributions do not depend strongly on the details of the diffusion model. This is caused by the high reaction rates of ion-molecule reactions so that diffusion becomes less important. This is also the reason why the simulation results are not very sensitive to uncertainties in the diffusion coefficients of the charged species. Only the diffusion coefficient of H_3O^+ has a considerable influence on the distribution of charges along the flame. But again, only the amount of ions in the cold region is influenced. The sequence and relative abundances of the ions are not changed.

A major problem for the simulations of ions in flames is to provide the necessary input data for the calculations. First of all, this concerns the chemical reactions together with their temperature-dependent kinetic rate coefficients. Also,

the thermodynamic properties of the species have to be found. Finally, molecular data for each single species is needed in order to calculate diffusion coefficients, the viscosity and the heat conductivity. Most of this species data is not available from measurements.

Quantum mechanical calculations provide a valuable tool for obtaining some of this information. For instance, electric dipoles and polarizabilities of species are already obtained by these methods. It should be possible to utilize quantum mechanical ab-initio calculations also to derive the other missing data like activation energies, quadrupole polarizabilities, dispersion coefficients, or the interaction potentials between two species directly.

The resulting model, especially the reaction system, forms a system of differential equations with a high number of parameters like the reaction rate coefficients. These parameters can be varied in the limits of their experimental uncertainty to obtain a better agreement with the measured species profiles. Parameter estimation approaches could be very valuable tools for this task.

Future research should extend the reaction mechanism to enable simulations of rich flames and other fuels. Also, additives to the fuel-oxidizer mixture are of interest. For the applications, simplified models which only predict the global charge distributions will be of interest. The aim of these models could be the reliable prediction of the electrical conductivity in a variety of systems like car engines or gas turbines.

Bibliography

[Ani03] V. G. Anicich. An index of the literature for bimolecular gas phase cation-molecule reaction kinetics. *JPL Publication*, 03-19, 2003.

[Bar03] J. E. Bartmess. Negative ion energetics data. In P. J. Linstrom and W. G. Mallard, editors, *NIST Chemistry WebBook, NIST Standard Reference Database Number 69*. National Institute of Standards and Technology, Gaithersburg MD, 20899, March 2003. http://webbook.nist.gov.

[BB02] M. J. Brunger and S. J. Buckman. Electron-molecule scattering cross-sections. I. Experimental techniques and data for diatomic molecules. *Physics Reports*, 357:215–458, 2002.

[BE88] R. C. Brown and A. N. Eraslan. Simulation of ionic structure in lean and close-to-stoichiometric acetylene flames. *Combustion and Flame*, 73:1–21, 1988.

[BFL$^+$87] H. Boehringer, D. W. Fahey, W. Lindinger, F. Howorka, F. C. Fehsenfeld, and D. L. Albritton. Mobilities of several mass-identified positive and negative ions in air. *International Journal of Mass Spectrometry and Ion Processes*, 81:45–65, 1987.

[BGN77] D. K. Bohme, J. M. Goodings, and Chun-Wai Ng. In situ chemical ionization as a probe for neutral constituents upstream in a methane-oxygen flame. *International Journal of Mass Spectrometry and Ion Physics*, 24:335–354, 1977.

[Boh79] D. K. Bohme. Chemical ionization in flames. In P. Ausloos, editor, *Kinetics of Ion-Molecule Reactions*, pages 323–343. Plenum Press, New York & London, 1979.

[BP85] S. J. Buckman and A. V. Phelps. Vibrational excitation of D_2 by low energy electrons. *Journal of Chemical Physics*, 82:4999–5011, 1985.

[BSL02] R. B. Bird, W. E. Stewart, and E. N. Lightfoot. *Transport phenomena*. John Wiley, New York, 2nd edition, 2002.

[Bur01] A. Burcat. Third millennium ideal gas and condensed phase thermochemical database for combustion. *Technion Aerospace Engineering (TAE) Report # 867*, 2001. Alexander Burcat's Ideal Gas Thermochemical Database http://garfield.chem.elte.hu/Burcat/burcat.html.

[CC94] S. Chapman and T. G. Cowling. *The Mathematical Theory of Non-Uniform Gases*. Cambridge University Press, 3rd edition, 1994.

[CDA+01] C. Chipot, F. Dehez, J. Angyan, C. Millot, M. Orozco, and F. J. Luque. Alternative approaches for the calculation of induction energies: Characterization, effectiveness, and pitfalls. *Journal of Physical Chemistry A*, 105:11505–11514, 2001.

[CDD+85] M. W. Chase, Jr., C. A. Davies, J. R. Downey, Jr., D. J. Frurip, R. A. McDonald, and A. N. Syverud. JANAF thermochemical tables third edition. *Journal of Physical and Chemical Reference Data, Supplement No. 1*, 14, 1985.

[CFGO00] M. Capitelli, C. M. Ferreira, B. F. Gordiets, and A. I. Osipov. *Plasma Kinetics in Atmospheric Gases*. Springer, 2000.

[CJ66] H. F. Calcote and D. E. Jensen. Ion-molecular reactions in flames. *Advances in Chemistry Series*, 58:291, 1966.

[CL90] D. P. Chong and S. R. Langhoff. Theoretical study of polarizabilities and hyperpolarizabilities of Ne, HF, F^-, and OH^-. *Journal of Chemical Physics*, 93:570–578, 1990.

[COK88] H. F. Calcote, D. B. Olson, and D. G. Keil. Are ions important in soot formation? *Energy and Fuels*, 2:494–504, 1988.

[Dut75] J. Dutton. A survey of electron swarm data. *Journal of Physical and Chemical Reference Data*, 4:577–856, 1975.

[EB88] A. N. Eraslan and R. C. Brown. Chemiionization and ion-molecule reactions in fuel-rich acetylene flames. *Combustion and Flame*, 74:19–37, 1988.

[EMA+78] H. W. Ellis, E. W. McDaniel, D. L. Albritton, L. A. Viehland, S. L. Lin, and E. A. Mason. Transport properties of gaseous ions over a wide energy range. Part II. *Atomic Data and Nuclear Data Tables*, 22:179–217, 1978.

[EPM76] H. W. Ellis, R. Y. Pai, and E. W. McDaniel. Transport properties of gaseous ions over a wide energy range. *Atomic Data and Nuclear Data Tables*, 17:177–210, 1976.

[ETMM84] H. W. Ellis, M. G. Thackston, E. W. McDaniel, and E. A. Mason. Transport properties of gaseous ions over a wide energy range. Part III. *Atomic Data and Nuclear Data Tables*, 31:113–151, 1984.

[FGKW99] J. Foerster, A. Guenther, M. Ketterer, and K.-J. Wald. Ion current sensing for spark ignition engines. *SAE Technical Paper Series*, 1999-01-0204:21–32, 1999.

[Fia97] A. B. Fialkov. Investigations on ions in flames. *Progress in Energy and Combustion Science*, 23:399–528, 1997.

[Fil01] E. Filimonova, 2001. Private communication.

[FK04] A. Fridman and L. A. Kennedy. *Plasma Physics and Engineering*. Taylor & Francis, New York, 2004.

[FKK+04] E. A. Fogleman, H. Koizumi, J. P. Kercher, B. Sztaray, and T. Baer. Heats of formation of the acetyl radical and ion obtained by threshold photoelectron photoion coincidence. *Journal of Physical Chemistry A*, 108:5288–5294, 2004.

[Fra02] R. N. Franklin. Electronegative plasmas – why are they so different? *Plasma Sources Science and Technology*, 11:31–37, 2002.

[Fra03a] R. N. Franklin. Ambipolar diffusion is a misnomer. *Journal of Physics D: Applied Physics*, 36:828–831, 2003.

[Fra03b] R. N. Franklin. Basic relationships in electronegative plasmas with a multiplicity of negative and positive ion species. *Journal of Physics D: Applied Physics*, 36:823–827, 2003.

[GBN79a] J. M. Goodings, D. K. Bohme, and Chun-Wai Ng. Detailed ion chemistry in methane-oxygen flames. I. Positive ions. *Combustion and Flame*, 36:27–43, 1979.

[GBN79b] J. M. Goodings, D. K. Bohme, and Chun-Wai Ng. Detailed ion chemistry in methane-oxygen flames. II. Negative ions. *Combustion and Flame*, 36:45–62, 1979.

[GM71] S. Gordon and B. J. McBride. Computer program for calculation of complex chemical equilibrium composition, rocket performance, incident and reflected shocks and Chapman-Jouguet detonations. *NASA SP-273*, 1971.

[Hay90] M. Hayashi. Electron collision cross sections determined from beam and swarm data by Boltzmann analysis. In M. Capitelli and J. N. Bardsley, editors, *Nonequilibrium Processes in Partially Ionized Gases*. Plenum Press, New York, 1990.

[Hay93] A. N. Hayhurst. The mass spectrometric sampling of ions from atmospheric pressure flames as exemplified by the reactions of OH^- and O_2^- in O_2-rich flames. *Pure and Applied Chemistry*, 65:285–295, 1993.

[HCB64] J. O. Hirschfelder, C. F. Curtiss, and R. B. Bird. *Molecular Theory of Gases and Liquids*. John Wiley, New York, 2nd edition, 1964.

[HL98] E. P. L. Hunter and S. G. Lias. Evaluated gas phase basicities and proton affinities of molecules: An update. *Journal of Physical and Chemical Reference Data*, 27:413–656, 1998.

[Joh04] R. D. Johnson. NIST computational chemistry comparison and benchmark database. http://srdata.nist.gov/cccbdb, May 2004. NIST Standard Reference Database Number 101, Release 10.

[Kar] V. Karbach. PhD thesis, Universität Heidelberg. In preparation.

[KKS96] S. Klein, E. Kochanski, and A. Strich. Electric properties of the oxonium ion in its ground and two lowest excited states. *Chemical Physics Letters*, 260:34–42, 1996.

[Lan78] J. E. Land. Electron scattering cross sections for momentum transfer and inelastic excitation in carbon monoxide. *Journal of Applied Physics*, 49:5716–5721, 1978.

[LCW+04] M. Lackner, S. Charareh, F. Winter, K. F. Iskra, D. Rüdisser, T. Neger, H. Kopecek, and E. Wintner. Investigation of the early stages in laser-induced ignition by Schlieren photography and laser-induced fluorescence spectroscopy. *Optics Express*, 12:4546 – 4557, 2004.

[Lia03] S. G. Lias. Ionization energy evaluation. In P. J. Linstrom and W. G. Mallard, editors, *NIST Chemistry WebBook, NIST Standard Reference Database Number 69*. National Institute of Standards and Technology, Gaithersburg MD, 20899, March 2003. http://webbook.nist.gov.

[Lid97] D. R. Lide. *CRC Handbook of Chemistry and Physics*. CRC Press Boca Raton, 78th edition, 1997.

[LM87] A. Loewenschuss and Y. Marcus. Standard thermodynamic functions of gaseous polyatomic ions at 100-1000 K. *Journal of Physical and Chemical Reference Data*, 16:61–89, 1987.

[LP78] S. A. Lawton and A. V. Phelps. Excitation of the $b\Sigma_g^+$ state of O_2 by low energy electrons. *Journal of Chemical Physics*, 69:1055–1068, 1978.

[Mar88] G. Maroulis. Electrical properties for HCO^+ and NNH^+ from fourth-order Moller-Plesset pertubation theory. *Zeitschrift für Naturforschung A*, 43(5):419–429, 1988.

[MG96] B. J. McBride and S. Gordon. Computer program for calculation of complex chemical equilibrium compositions and applications: II. Users manual and program description. *NASA Reference Publication 1311*, 1996.

[MHL95] T. D. Mark, Y. Hatano, and F. Linder. Atomic and molecular data for radiotherapy and radiation research. *IAEA-TECDOC-799*, 1995.

[MM73] E. W. McDaniel and E. A. Mason. The mobility and diffusion of ions in gases. John Wiley, New York, 1973.

[MSF+05] P. Mehresh, J. Souder, D. Flowers, U. Riedel, and R. W. Dibble. Combustion timing in HCCI engines determined by ion-sensor: experimental and kinetic modeling. *Proceedings of the Combustion Institute*, 30:2701–2709, 2005.

[Mur93] A. B. Murphy. Diffusion in equilibrium mixtures of ionized gases. *Physical Review E*, 48:3594–3603, 1993.

[MZG02] B. J. McBride, M. J. Zehe, and S. Gordon. NASA Glenn coefficients for calculating thermodynamic properties of individual species. *NASA report TP-2002-211556*, 2002. http://cea.grc.nasa.gov.

[PB93] T. Pedersen and R. C. Brown. Simulation of electric field effects in premixed methane flames. *Combustion and Flame*, 94:433–448, 1993.

[PEAM75] R. Y. Pai, H. W. Ellis, G. R. Akridge, and E. W. McDaniel. Generalized Einstein relation: Application to ions in molecular gases. *Physical Review A*, 12:1781–1784, 1975.

[Phe03] A. V. Phelps. ftp://jila.colorado.edu, 2003.

[PM73] J. Peeters and G. Mahnen. Reaction mechanisms and rate constants of elementary steps in methane-oxygen flames. *Proceedings of the Combustion Institute*, 14:133–146, 1973.

[QCD04] QCDB Group. Quantum chemistry literature database. http://qcldb2.ims.ac.jp, 2004.

[Rab84] M. Rabrenovic. Ionization energies of ions formed by ion/molecule reactions. *International Journal of Mass Spectrometry and Ion Processes*, 56:85–91, 1984.

[Rie03] U. Riedel. Simulation nicht-thermischer Prozessplasmen mit detaillierten physikalisch-chemischen Modellen. Habilitation thesis, Universität Heidelberg, 2003.

[Rog85] G. L. Rogoff. Ambipolar diffusion coefficients for discharges in attaching gases. *Journal of Physics D: Applied Physics*, 18:1533–1545, 1985.

[RSM97] R. Reinmann, A. Saitzkoff, and F. Mauss. Local air-fuel ratio measurements using the spark plug as an ionization sensor. *SAE Technical Paper Series*, SP-1236:175–185, 1997.

[SB73] T. Su and M. T. Bowers. Theory of ion-polar molecule collisions. Comparison with experimental charge transfer reactions of rare gas ions to geometric isomers of difluorobenzene and dichloroethylene. *Journal of Chemical Physics*, 58:3027–3037, 1973.

[Sch05] P. J. Schupf. Computational chemistry laboratory, department of chemistry, Colby college.
www.colby.edu/chemistry/webmo/mointro.html, 2005.

[SCTJ03] P. Salvador, J. E. Curtis, D. J. Tobias, and P. Jungwirth. Polarizability of the nitrate anion and its solvation at the water/air interface. *Physical Chemistry, Chemical Physics*, 5:3752–3757, 2003.

[Sel02] S. Selle. *Transportkoeffizienten ionisierter Spezies in reaktiven Strömungen*. PhD thesis, Universität Heidelberg, 2002.

[SR99] S. Selle and U. Riedel. Transport properties of ionized species. In P. Fauchais, J. van der Mullen, and J. Heberlein, editors, *Heat and Mass Transfer under Plasma Conditions*, volume 891 of *Annals of the New York Academy of Sciences*, pages 72–80. The New York Academy of Sciences, 1999.

[SRM97] A. Saitzkoff, R. Reinmann, and F. Mauss. In-cylinder pressure measurements using the spark plug as an ionization sensor. *SAE Technical Paper Series*, 970857:187–197, 1997.

[SRW98] S. Selle, U. Riedel, and J. Warnatz. Reaction rates and transport coefficients of ionized species in high temperature air. *Proceedings of the Third European Symposium on Aerothermodynamics for Space Vehicles*, pages 327–332, 1998.

[SS95] D. Smith and P. Spanel. Ions in the terrestrial atmosphere and in interstellar clouds. *Mass Spectrometry Reviews*, 14:255–278, 1995.

[SSB78] T. Su, E. C. F. Su, and M. T. Bowers. Ion-polar molecule collisions. conservation of angular momentum in the average dipole orientation theory. The AADO theory. *Journal of Chemical Physics*, 69:2243–2250, 1978.

[SSTS02] A. M. Starik, A. M. Savelev, N. S. Titova, and U. Schuhmann. Modeling of sulfur gases and chemiions in aircraft engines. *Aerospace Science and Technology*, 6:63–81, 2002.

[SSZ01] S. M. Starikovskaia, A. Yu Starikovskii, and D. V. Zatsepin. Hydrogen oxidation in a stoichiometric hydrogen-air mixture in the fast ionization wave. *Combustion Theory and Modelling*, 5:97–129, 2001.

[SVM03] A. Sorokin, X. Vancassel, and P. Mirabel. Emission of ions and charged soot particles by aircraft engines. *Atmospheric Chemistry and Physics*, 3:325–334, 2003.

[TMM00] Y. H. Le Teuff, T. J. Millar, and A. J. Markwick. The UMIST database for astrochemistry 1999. *Astronomy and Astrophysics Supplement*, 146:157–168, 2000. http://www.rate99.co.uk.

[TS97] G. S. Tschumper and H. F. Schäfer. Predicting electron affinities with density functional theory: Some positive results for negative ions. *Journal of Chemical Physics*, 107:2529–2541, 1997.

[TSR+00] M. Thiele, S. Selle, U. Riedel, J. Warnatz, and U. Maas. Numerical simulation of spark ignition including ionization. *Proceedings of the Combustion Institute*, 28:1177–1185, 2000.

[UR98] D. Upadhyay and G. Rizzoni. AFR control on a single cylinder engine using the ionization current. *SAE Technical Paper Series*, 980203:1–7, 1998.

[Vie04] L. A. Viehland. http://www.chatham.edu/undergraduate/chem/Viehland/viehland.html, 2004.

[War78a] J. Warnatz. Calculation of the structure of laminar flat flames I: Flame velocity of freely propagating ozone decomposition flames. *Berichte der Bunsengesellschaft für Physikalische Chemie*, 82:193–200, 1978.

[War78b] J. Warnatz. Calculation of the structure of laminar flat flames II: Flame velocity and structure of freely propagating hydrogen-oxygen and hydrogen-air-flames. *Berichte der Bunsengesellschaft für Physikalische Chemie*, 82:643–649, 1978.

[WMD97] J. Warnatz, U. Maas, and R. W. Dibble. *Verbrennung.* Springer Verlag, Heidelberg, 2nd edition, 1997.

[Wor65] G. Wortberg. Ion-concentration measurements in a flat flame at atmospheric pressure. *Proceedings of the Combustion Insitute*, 10:651–655, 1965.

[YKT+02] T. Yuasa, S. Kadota, M. Tsue, M. Kono, H. Nomura, and Y. Ujiie. Effects of energy deposition schedule on minimum ignition energy in spark ignition of methane/air mixtures. *Proceedings of the Combustion Institute*, 29:743–750, 2002.

Appendix A

Reaction mechanism

The chemical reaction rate coefficients for the uncharged species were taken from [Kar]. This mechanism consists of 39 species and 417 elementary reactions. The reactions involving charged species are listed in the Tables A.2, A.3, A.4, and A.5. The ion mechanism consists of 11 species and 67 reactions. The reaction rate coefficients k are calculated in the usual way according to the Arrhenius law:

$$k = AT^n \exp\left(-\frac{E_\mathrm{a}}{RT}\right) \quad . \tag{A.1}$$

The temperature T is in Kelvin, and the gas constant R is in kJ/(mol K). The unit of the activation energy E_a is kJ/mol, the resulting reaction rate has the unit mol/(cm^3 s). Thus, the pre-exponential factor A has the unit of cm^3/(mol s) for bimolecular and cm^6/(mol^2 s) for trimolecular reactions.

A reaction in the mechanism containing a third body represents 7 individual reactions which result, if one substitutes the third body by the species names in Table A.1. The rate coefficients of these reactions are calculated by multiplying the collision efficiencies by the common rate coefficient resulting from the Arrhenius expression. The collision efficiencies used for the four third bodies M(1) to M(4) are taken from [Kar], see Table A.1.

	H_2	H_2O	O_2	N_2	CO	CO_2	CH_4
M(1)	1.0	6.5	0.4	0.4	0.75	1.5	3.0
M(2)	1.0	2.55	0.4	0.4	0.75	1.5	3.0
M(3)	1.0	6.5	0.4	0.67	0.75	1.5	3.0
M(4)	1.0	6.5	0.4	0.4	0.75	1.5	0.66

Table A.1: Collision efficiencies and definition of third bodies.

Reaction					A	n	E_a	Ref.
CH	+ O	$\rightleftharpoons$ CHO^+	+ E^-		2.512×10^{11}	0.000	7.118	[Sel02]
CHO^+	+ E^-	$\rightleftharpoons$ CO	+ H		7.400×10^{18}	-0.680	0.000	[TMM00]
CHO^+	+ H_2O	$\rightleftharpoons$ H_3O^+	+ CO		1.506×10^{15}	0.000	0.000	[TMM00]
CHO^+	+ C_2H_5OH	$\rightleftharpoons$ H_3O^+	+ CO	+ C_2H_4	6.000×10^{14}	0.000	0.000	[Ani03]
H_3O^+	+ E^-	$\rightleftharpoons$ H_2O	+ H		2.291×10^{18}	-0.500	0.000	[TMM00]
H_3O^+	+ E^-	$\rightleftharpoons$ OH	+ H	+ H	7.949×10^{21}	-1.370	0.000	[TMM00]
H_3O^+	+ E^-	$\rightleftharpoons$ H_2	+ OH		1.253×10^{19}	-0.500	0.000	[TMM00]
H_3O^+	+ E^-	$\rightleftharpoons$ O	+ H_2	+ H	6.000×10^{17}	-0.300	0.000	[TMM00]
H_3O^+	+ C	$\rightleftharpoons$ CHO^+	+ H_2		6.022×10^{12}	0.000	0.000	[TMM00]
CHO^+	+ CH_2CO	$\rightleftharpoons$ $C_2H_3O^+$	+ CO		1.259×10^{15}	-0.048	0.000	[TMM00]
CHO^+	+ CH_3	$\rightleftharpoons$ $C_2H_3O^+$	+ H		7.763×10^{14}	-0.006	0.000	[BE88]
$C_2H_3O^+$	+ E^-	$\rightleftharpoons$ CH_2CO	+ H		2.291×10^{18}	-0.500	0.000	[TMM00]
H_3O^+	+ CH_2CO	$\rightleftharpoons$ $C_2H_3O^+$	+ H_2O		1.204×10^{15}	0.000	0.000	[TMM00]
$C_2H_3O^+$	+ E^-	$\rightleftharpoons$ CO	+ CH_3		2.403×10^{17}	-0.050	0.000	[TMM00]
$C_2H_3O^+$	+ O	$\rightleftharpoons$ CHO^+	+ CH_2O		2.000×10^{14}	0.000	0.000	
CHO^+	+ CH_3OH	$\rightleftharpoons$ CH_5O^+	+ CO		8.710×10^{14}	-0.056	0.000	[TMM00]
H_3O^+	+ CH_3OH	$\rightleftharpoons$ CH_5O^+	+ H_2O		1.506×10^{15}	0.000	0.000	[TMM00]
CH_5O^+	+ E^-	$\rightleftharpoons$ CH_3OH	+ H		2.403×10^{17}	-0.050	0.000	[TMM00]
CH_5O^+	+ CH_2CO	$\rightleftharpoons$ $C_2H_3O^+$	+ CH_3OH		1.486×10^{15}	-0.077	-0.347	
O_2^-	+ H_2	$\rightleftharpoons$ H_2O_2	+ E^-		6.022×10^{14}	0.000	0.000	[Fil01]
O_2^-	+ H	$\rightleftharpoons$ HO_2	+ E^-		7.226×10^{14}	0.000	0.000	[SSZ01]
O_2^-	+ OH	$\rightleftharpoons$ OH^-	+ O_2		6.022×10^{13}	0.000	0.000	[Hay93]
O_2^-	+ H	$\rightleftharpoons$ OH^-	+ O		1.084×10^{15}	0.000	0.000	[SSZ01]
OH^-	+ O	$\rightleftharpoons$ HO_2	+ E^-		1.204×10^{14}	0.000	0.000	[GBN79b]
OH^-	+ H	$\rightleftharpoons$ H_2O	+ E^-		1.084×10^{15}	0.000	0.000	[TMM00]
OH^-	+ C	$\rightleftharpoons$ CHO	+ E^-		3.001×10^{14}	0.000	0.000	[TMM00]

Table A.2: Reaction mechanism of the charged species for lean to stoichiometric methane-air flames: Bimolecular reactions.

Reaction					A	n	E_a	Ref.
OH^-	$+ CH$	$\rightleftharpoons CH_2O$	$+ E^-$		3.001×10^{14}	0.00	0.000	[TMM00]
OH^-	$+ CH_3$	$\rightleftharpoons CH_3OH$	$+ E^-$		6.022×10^{14}	0.00	0.000	[TMM00]
CO_3^-	$+ H$	$\rightleftharpoons OH^-$	$+ CO_2$		1.020×10^{14}	0.00	0.000	[GBN79b]
CO_3^-	$+ O$	$\rightleftharpoons O_2^-$	$+ CO_2$		4.600×10^{13}	0.00	0.000	[GBN79b]
CHO_2^-	$+ H$	$\rightleftharpoons CO_2$	$+ H_2$	$+ E^-$	1.159×10^{14}	0.00	0.000	
OH^-	$+ CHO$	$\rightleftharpoons CHO_2^-$	$+ H$		2.959×10^{15}	-0.14	-0.441	
O^-	$+ C$	$\rightleftharpoons CO$	$+ E^-$		3.011×10^{14}	0.00	0.000	[TMM00]
O^-	$+ H_2$	$\rightleftharpoons OH^-$	$+ H$		1.987×10^{13}	0.00	0.000	[TMM00]
O^-	$+ CH_4$	$\rightleftharpoons OH^-$	$+ CH_3$		6.022×10^{13}	0.00	0.000	[TMM00]
O^-	$+ H_2O$	$\rightleftharpoons OH^-$	$+ OH$		8.431×10^{14}	0.00	0.000	[CFGO00]
O^-	$+ CH_2O$	$\rightleftharpoons OH^-$	$+ CHO$		5.601×10^{14}	0.00	0.000	[BGN77]
O^-	$+ CH_2O$	$\rightleftharpoons CHO_2^-$	$+ H$		1.307×10^{15}	0.00	0.000	[BGN77]
O^-	$+ C_2H_6$	$\rightleftharpoons C_2H_5$	$+ OH^-$		6.130×10^{15}	-0.50	0.000	[SSTS02]
O^-	$+ H$	$\rightleftharpoons OH$	$+ E^-$		3.011×10^{14}	0.00	0.000	[TMM00]
O^-	$+ H_2$	$\rightleftharpoons H_2O$	$+ E^-$		4.215×10^{14}	0.00	0.000	[TMM00]
O^-	$+ CH$	$\rightleftharpoons CHO$	$+ E^-$		3.011×10^{14}	0.00	0.000	[TMM00]
O^-	$+ 1CH_2$	$\rightleftharpoons CH_2O$	$+ E^-$		3.011×10^{14}	0.00	0.000	[TMM00]
O^-	$+ CO$	$\rightleftharpoons CO_2$	$+ E^-$		3.914×10^{14}	0.00	0.000	[TMM00]
O^-	$+ O$	$\rightleftharpoons O_2$	$+ E^-$		8.431×10^{13}	0.00	0.000	[TMM00]
O^-	$+ C_2H_2$	$\rightleftharpoons CH_2CO$	$+ E^-$		7.226×10^{14}	0.00	0.000	[GBN79b]
O^-	$+ H_2O$	$\rightleftharpoons H_2O_2$	$+ E^-$		3.613×10^{11}	0.00	0.000	[SSZ01]
O_2^-	$+ O$	$\rightleftharpoons O^-$	$+ O_2$		1.987×10^{14}	0.00	0.000	[CFGO00]

Table A.3: Reaction mechanism of the charged species for lean to stoichiometric methane-air flames: Bimolecular reactions. Continued from Table A.2.

Reaction					A	n	E_a	Ref.
O_2^-	$+ C_2H_3O^+$	$\rightleftharpoons O_2$	$+ CH_3CO$		2.090×10^{18}	-0.50	0.000	[SSTS02]
O_2^-	$+ C_2H_3O^+$	$\rightleftharpoons O_2$	$+ CH_2CO$	$+ H$	1.000×10^{18}	0.00	0.000	
O_2^-	$+ CH_5O^+$	$\rightleftharpoons O_2$	$+ CH_3$	$+ H_2O$	1.000×10^{18}	0.00	0.000	
O^-	$+ C_2H_3O^+$	$\rightleftharpoons O$	$+ CH_3CO$		2.090×10^{18}	-0.50	0.000	[SSTS02]
O^-	$+ C_2H_3O^+$	$\rightleftharpoons O$	$+ CH_2CO$	$+ H$	1.000×10^{18}	0.00	0.000	
O^-	$+ C_2H_3O^+$	$\rightleftharpoons O$	$+ CH_2CHO$		1.000×10^{18}	0.00	0.000	
O^-	$+ CH_5O^+$	$\rightleftharpoons O$	$+ CH_3$	$+ H_2O$	1.000×10^{18}	0.00	0.000	
CHO_3^-	$+ C_2H_3O^+$	$\rightleftharpoons CH_3CO$	$+ CO_2$	$+ OH$	2.000×10^{18}	0.00	0.000	
CHO_3^-	$+ CH_5O^+$	$\rightleftharpoons CH_3OH$	$+ H_2O$	$+ CO_2$	2.000×10^{18}	0.00	0.000	

Table A.4: Reaction mechanism of the charged species for lean to stoichiometric methane-air flames: Bimolecular reactions. Continued from Table A.3.

Reaction					A	n	E_a	Ref.
O_2	$+ E^-$	$+ O$	$\rightleftharpoons O_2^-$	$+ O$	3.627×10^{16}	0.00	0.000	[CFGO00]
O_2	$+ E^-$	$+ O_2$	$\rightleftharpoons O_2^-$	$+ O_2$	1.523×10^{21}	-1.00	4.989	[CFGO00]
O_2	$+ E^-$	$+ H_2O$	$\rightleftharpoons O_2^-$	$+ H_2O$	5.077×10^{18}	0.00	0.000	[CFGO00]
O_2	$+ E^-$	$+ N_2$	$\rightleftharpoons O_2^-$	$+ N_2$	3.590×10^{21}	-2.00	0.582	[CFGO00]
E^-	$+ OH$	$+ M(1)$	$\rightleftharpoons OH^-$	$+ M(1)$	1.088×10^{17}	0.00	0.000	[Hay93]
OH^-	$+ CO_2$	$+ O_2$	$\rightleftharpoons CHO_3^-$	$+ O_2$	2.760×10^{20}	0.00	0.000	[GBN79b]
OH^-	$+ CO_2$	$+ H_2O$	$\rightleftharpoons CHO_3^-$	$+ H_2O$	1.104×10^{21}	0.00	0.000	
E^-	$+ O$	$+ O_2$	$\rightleftharpoons O^-$	$+ O_2$	3.627×10^{16}	0.00	0.000	[CFGO00]
E^-	$+ O$	$+ O$	$\rightleftharpoons O^-$	$+ O$	3.021×10^{17}	0.00	0.000	[SSZ01]
O^-	$+ CO_2$	$+ O_2$	$\rightleftharpoons CO_3^-$	$+ O_2$	1.123×10^{20}	0.00	0.000	[GBN79b]

Table A.5: Reaction mechanism of the charged species for lean to stoichiometric methane-air flames: Trimolecular reactions.

Appendix B

Thermodynamic data

The following database has been used to calculate the thermodynamic properties of the single species. The information obtained is the temperature-dependent molar heat capacity $\overline{C}_p$, the molar enthalpy $\overline{H}$, and the molar entropy $\overline{S}$ of each species. It is assumed that the ideal gas law is valid.

The data format follows the old NASA standard [GM71]. Each data set consists of two sets of polynomial coefficients a_1, a_2, ... , a_7 used to fit the temperature-dependent properties in a low and a high temperature range, respectively. The first line contains the species name, followed by optional comments, and its elementary composition. Then, the temperature ranges are specified: first the low and the high limits are given, followed by the temperature which separates the lower from the higher temperature range of the two fits. The next three lines consist of the 14 coefficients, first for the high then for the low temperature range. Finally, the thermodynamic properties are calculated by the following formulas, see also Section 2.4:

$$\begin{aligned}
\frac{\overline{C}_p}{R} &= a_1 + a_2 T + a_3 T^2 + a_4 T^3 + a_5 T^4 \\
\frac{\overline{H}}{R} &= a_1 T + \frac{a_2}{2} T^2 + \frac{a_3}{3} T^3 + \frac{a_4}{4} T^4 + \frac{a_5}{5} T^5 + a_6 \\
\frac{\overline{S}}{R} &= a_1 \ln T + a_2 T + \frac{a_3}{2} T^2 + \frac{a_4}{3} T^3 + \frac{a_5}{4} T^4 + a_7 \quad .
\end{aligned}$$

References for the new species are given in Section 3.2. All other data is taken from [Sel02].

```
H               120186H   1              G  0300.00   5000.00  1000.00
 0.02500000E+02 0.00000000E+00 0.00000000E+00 0.00000000E+00 0.00000000E+00
 0.02547162E+06-0.04601176E+01 0.02500000E+02 0.00000000E+00 0.00000000E+00
 0.00000000E+00 0.00000000E+00 0.02547162E+06-0.04601176E+01
```

```
HCCO               32387H   1C   2O   1     G  0300.00   4000.00  1000.00
 0.06758073E+02 0.02000400E-01-0.02027607E-05-0.10411318E-09 0.01965164E-12
 0.01901513E+06-0.09071262E+02 0.05047965E+02 0.04453478E-01 0.02268282E-05
-0.14820945E-08 0.02250741E-11 0.01965891E+06 0.04818439E+01
HO2                20387H   1O   2          G  0300.00   5000.00  1000.00
 0.04072191E+02 0.02131296E-01-0.05308145E-05 0.06112269E-09-0.02841164E-13
-0.15797270E+03 0.03476029E+02 0.02979963E+02 0.04996697E-01-0.03790997E-04
 0.02354192E-07-0.08089024E-11 0.01762273E+04 0.09222724E+02
H2                 121286H   2               G  0300.00   5000.00  1000.00
 0.02991423E+02 0.07000644E-02-0.05633828E-06-0.09231578E-10 0.15827519E-14
-0.08350340E+04-0.13551101E+01 0.03298124E+02 0.08249441E-02-0.08143015E-05
-0.09475434E-09 0.04134872E-11-0.10125209E+04-0.03294094E+02
H2O                20387H   2O   1          G  0300.00   5000.00  1000.00
 0.02672145E+02 0.03056293E-01-0.08730260E-05 0.12009964E-09-0.06391618E-13
-0.02989921E+06 0.06862817E+02 0.03386842E+02 0.03474982E-01-0.06354696E-04
 0.06968581E-07-0.02506588E-10-0.03020811E+06 0.02590232E+02
H2O2               120186H   2O   2          G  0300.00   5000.00  1000.00
 0.04573167E+02 0.04336136E-01-0.14746888E-05 0.02348903E-08-0.14316536E-13
-0.01800696E+06 0.05011369E+01 0.03388753E+02 0.06569226E-01-0.14850125E-06
-0.04625805E-07 0.02471514E-10-0.01766314E+06 0.06785363E+02
C                  121086C   1               G  0300.00   5000.00  1000.00
 0.02602087E+02-0.01787081E-02 0.09087041E-06-0.11499333E-10 0.03310844E-14
 0.08542154E+06 0.04195177E+02 0.02498584E+02 0.08085776E-03-0.02697697E-05
 0.03040729E-08-0.11066518E-12 0.08545878E+06 0.04753459E+02
CH                 121286C   1H   1          G  0300.00   5000.00  1000.00
 0.02196223E+02 0.02340381E-01-0.07058201E-05 0.09007582E-09-0.03855040E-13
 0.07086723E+06 0.09178373E+02 0.03200202E+02 0.02072875E-01-0.05134431E-04
 0.05733890E-07-0.01955533E-10 0.07045259E+06 0.03331587E+02
CH*                121286C   1H   1          G  0300.00   5000.00  1000.00
 0.02196223E+02 0.02340381E-01-0.07058201E-05 0.09007582E-09-0.03855040E-13
 0.07086723E+06 0.09178373E+02 0.03200202E+02 0.02072875E-01-0.05134431E-04
 0.05733890E-07-0.01955533E-10 0.07045259E+06 0.03331587E+02
CHO      HCO       121286H   1C   1O   1     G  0300.00   5000.00  1000.00
 0.03557271E+02 0.03345572E-01-0.13350060E-05 0.02470572E-08-0.01713850E-12
 0.03916324E+05 0.05552299E+02 0.02898329E+02 0.06199146E-01-0.09623084E-04
 0.10898249E-07-0.04574885E-10 0.04159922E+05 0.08983614E+02
1CH2     CH2(S)     31287C   1H   2          G  0300.00   4000.00  1000.00
 0.03552888E+02 0.02066788E-01-0.01914116E-05-0.11046733E-09 0.02021349E-12
 0.04984975E+06 0.01686570E+02 0.03971265E+02-0.01699088E-02 0.10253689E-05
 0.02492550E-07-0.01981266E-10 0.04989367E+06 0.05753207E+00
3CH2     CH2       120186C   1H   2          G  0250.00   4000.00  1000.00
 0.03636407E+02 0.01933056E-01-0.01687016E-05-0.10098994E-09 0.01808255E-12
 0.04534134E+06 0.02156560E+02 0.03762237E+02 0.11598191E-02 0.02489585E-05
 0.08800836E-08-0.07332435E-11 0.04536790E+06 0.01712577E+02
CH2O               121286C   1H   2O   1     G  0300.00   5000.00  1000.00
 0.02995606E+02 0.06681321E-01-0.02628954E-04 0.04737153E-08-0.03212517E-12
-0.15320369E+05 0.06912572E+02 0.16527311E+01 0.12631439E-01-0.01888168E-03
 0.02050031E-06-0.08413237E-10-0.14865404E+05 0.13784820E+02
CH2OH              120186H   3C   1O   1     G  0250.00   4000.00  1000.00
 0.06327520E+02 0.03608270E-01-0.03201547E-05-0.01938750E-08 0.03509704E-12
-0.04474509E+05-0.08329365E+02 0.02862628E+02 0.10015273E-01-0.05285435E-05
-0.05138539E-07 0.02246041E-10-0.03349678E+05 0.10397938E+02
CH2CHO   CH2HCO    120186O   1H   3C   2     G  0300.00   5000.00  1000.00
 0.05975670E+02 0.08130591E-01-0.02743624E-04 0.04070304E-08-0.02176017E-12
 0.04903218E+04-0.05045251E+02 0.03409062E+02 0.10738574E-01 0.01891492E-04
-0.07158583E-07 0.02867385E-10 0.15214766E+04 0.09558290E+02
CH2CH2OHH5C2O      T 4/83H   5C   2O   1    0G   300.000  5000.    1000.00
 0.75944014E+01 0.93229339E-02-0.30303854E-05 0.43216319E-09-0.21970039E-13
-0.57727852E+04-0.13968735E+02 0.14019508E+01 0.21543175E-01-0.22326512E-05
-0.14464092E-07 0.80488420E-11-0.38464519E+04 0.19135818E+02           1606
CH2CO              121686C   2H   2O   1     G  0300.00   5000.00  1000.00
 0.06038817E+02 0.05804840E-01-0.01920953E-04 0.02794484E-08-0.14588676E-13
-0.08583402E+05-0.07657581E+02 0.02974970E+02 0.12118712E-01-0.02345045E-04
-0.06466685E-07 0.03905649E-10-0.07632636E+05 0.08673553E+02
```

```
CH3               121286C   1H   3          G  0300.00   5000.00  1000.00
 0.02844051E+02 0.06137974E-01-0.02230345E-04 0.03785161E-08-0.02452159E-12
 0.16437809E+05 0.05452697E+02 0.02430442E+02 0.11124099E-01-0.01680220E-03
 0.16218288E-07-0.05864952E-10 0.16423781E+05 0.06789794E+02
CH3O               121686C   1H   3O   1     G  0300.00   4000.00  1000.00
 0.03770799E+02 0.07871497E-01-0.02656384E-04 0.03944431E-08-0.02112616E-12
 0.12783252E+03 0.02929575E+02 0.02106204E+02 0.07216595E-01 0.05338472E-04
-0.07377636E-07 0.02075610E-10 0.09786011E+04 0.13152177E+02
CH3OH              121686C   1H   4O   1     G  0300.00   5000.00  1000.00
 0.04029061E+02 0.09376593E-01-0.03050254E-04 0.04358793E-08-0.02224723E-12
-0.02615791E+06 0.02378195E+02 0.02660115E+02 0.07341508E-01 0.07170050E-04
-0.08793194E-07 0.02390570E-10-0.02535348E+06 0.11232631E+02
CH3O2              L 1/84C   1H   3O   2    0G   300.000  5000.00  1000.00
 0.66812963E 01 0.80057271E-02-0.27188507E-05 0.40631365E-09-0.21927725E-13
 0.52621851E 03-0.99423847E 01 0.20986490E 01 0.15786357E-01 0.75683261E-07
-0.11274587E-07 0.56665133E-11 0.20695879E 04 0.15007068E 02 0.33715510E+04
CH3O2H  CH4O2      T 5/92C   1H   4O   2    0G   298.150  5000.000 1000.00
 0.66499943D+01 0.10351461D-01-0.33524105D-05 0.53645535D-09-0.33949756D-13
-0.19232344D+05-0.77922626D+01 0.27586279D+01 0.18150526D-01-0.40892298D-05
-0.68391987D-08 0.41430701D-11-0.17986394D+05 0.13071986D+02-0.16404863D+05
CH3CHO  CH3HCO     120186C   2O   1H   4     G  0300.00   5000.00  1000.00
 0.05868650E+02 0.10794241E-01-0.03645530E-04 0.05412912E-08-0.02896844E-12
-0.02264568E+06-0.06012946E+02 0.02505695E+02 0.13369907E-01 0.04671953E-04
-0.11281401E-07 0.04263566E-10-0.02124588E+06 0.13350887E+02
CH3CHOH            103190C   2H   5O   1     G  0300.00   4000.00  1500.00
 0.11611482E+02 0.05173117E-01-0.04856684E-05-0.02202894E-08 0.03913721E-12
-0.12488109E+05-0.03688212E+03 0.14159398E+01 0.02870648E+00-0.02373820E-03
 0.11488865E-07-0.02391420E-10-0.08638718E+05 0.01844256E+03
CH3CO                 C   2H   3O   1         0200.000  6000.00  1000.00
 0.53137165E+01 0.91737793E-02-0.33220386E-05 0.53947456E-09-0.32452368E-13
-0.36450414E+04-0.16757558E+01 0.40358705E+01 0.87729487E-03 0.30710010E-04
-0.39247565E-07 0.15296869E-10-0.26820738E+04 0.78617682E+01-0.12388039E+04
CH4                121286C   1H   4          G  0300.00   5000.00  1000.00
 0.01683478E+02 0.10237236E-01-0.03875128E-04 0.06785585E-08-0.04503423E-12
-0.10080787E+05 0.09623395E+02 0.07787415E+01 0.01747668E+00-0.02783409E-03
 0.03049708E-06-0.12239307E-10-0.09825229E+05 0.13722195E+02
CO                 121286C   1O   1          G  0300.00   5000.00  1000.00
 0.03025078E+02 0.14426885E-02-0.05630827E-05 0.10185813E-09-0.06910951E-13
-0.14268350E+05 0.06108217E+02 0.03262451E+02 0.15119409E-02-0.03881755E-04
 0.05581944E-07-0.02474951E-10-0.14310539E+05 0.04848897E+02
CO2                121286C   1O   2          G  0300.00   5000.00  1000.00
 0.04453623E+02 0.03140168E-01-0.12784105E-05 0.02393996E-08-0.16690333E-13
-0.04896696E+06-0.09553959E+01 0.02275724E+02 0.09922072E-01-0.10409113E-04
 0.06866686E-07-0.02117280E-10-0.04837314E+06 0.10188488E+02
C2H                 20387C   2H   1          G  0300.00   5000.00  1000.00
 0.04427688E+02 0.02216268E-01-0.06048952E-05 0.09882517E-09-0.07351179E-13
 0.06590415E+06-0.11994418E+01 0.03050667E+02 0.06051674E-01-0.04956634E-04
 0.02804159E-07-0.08193332E-11 0.06630011E+06 0.05954361E+02
C2H2               121386C   2H   2          G  0300.00   5000.00  1000.00
 0.04436770E+02 0.05376039E-01-0.01912816E-04 0.03286379E-08-0.02156709E-12
 0.02566766E+06-0.02800338E+02 0.02013562E+02 0.15190446E-01-0.16163189E-04
 0.09078992E-07-0.01912746E-10 0.02612444E+06 0.08805378E+02
C2H3                12787C   2H   3          G  0300.00   5000.00  1000.00
 0.05933468E+02 0.04017745E-01-0.03966739E-05-0.14412666E-09 0.02378643E-12
 0.03185434E+06-0.08530313E+02 0.02459276E+02 0.07371476E-01 0.02109872E-04
-0.13216421E-08-0.11847838E-11 0.03335225E+06 0.11556202E+02
C2H4               121286C   2H   4          G  0300.00   5000.00  1000.00
 0.03528418E+02 0.11485185E-01-0.04418385E-04 0.07844600E-08-0.05266848E-12
 0.04428288E+05 0.02230389E+02-0.08614880E+01 0.02796162E+00-0.03388677E-03
 0.02785152E-06-0.09737879E-10 0.05573046E+05 0.02421148E+03
C2H5                12387C   2H   5          G  0300.00   5000.00  1000.00
 0.07190480E+02 0.06484077E-01-0.06428064E-05-0.02347879E-08 0.03880877E-12
 0.10674549E+05-0.14780892E+02 0.02690701E+02 0.08719133E-01 0.04419838E-04
 0.09338703E-08-0.03927773E-10 0.12870404E+05 0.12138195E+02
```

```
C2H5O    CH3CH2O    103190C    2H    5O    1      G  0300.00    4000.00  1500.00
 0.11871147E+02 0.05390415E-01-0.04990159E-05-0.02399584E-08 0.04255456E-12
-0.05950457E+05-0.03996584E+03 0.06904570E+01 0.02951397E+00-0.02245116E-03
 0.10116003E-07-0.02044100E-10-0.15599183E+04 0.02130229E+03
C2H5OH             L 8/88C    2H    6O    1     0G    200.000   6000.000 1000.00
 0.65624365e+01 0.15204222e-01-0.53896795e-05 0.86225011e-09-0.51289787e-13
-0.31525621e+05-0.94730202e+01 0.48586957e+01-0.37401726e-02 0.69555378e-04
-0.88654796e-07 0.35168835e-10-0.29996132e+05 0.48018545e+01-0.28257829e+05
C2H6               121686C    2H    6           G  0300.00    4000.00  1000.00
 0.04825938E+02 0.13840429E-01-0.04557258E-04 0.06724967E-08-0.03598161E-12
-0.12717793E+05-0.05239506E+02 0.14625388E+01 0.15494667E-01 0.05780507E-04
-0.12578319E-07 0.04586267E-10-0.11239176E+05 0.14432295E+02
O                  selle O    1O    00    00    0G       200.00 30100.00 16800.00
 0.63846370E+02-0.11202832E-01 0.71871680E-06-0.18543426E-10 0.16566516E-15
-0.22622359E+06-0.47840036E+03 0.25991110E+01-0.97668390E-04 0.34826298E-07
-0.35243850E-11 0.12158067E-15 0.29186142E+05 0.45660003E+01
OH                 1212860    1H    1           G  0300.00    5000.00  1000.00
 0.02882730E+02 0.10139743E-02-0.02276877E-05 0.02174683E-09-0.05126305E-14
 0.03886888E+05 0.05595712E+02 0.03637266E+02 0.01850910E-02-0.16761646E-05
 0.02387202E-07-0.08431442E-11 0.03606781E+05 0.13588605E+01
O2                 selle O    2O    00    00    0G       200.00 30100.00 10300.00
-0.42477619E+01 0.25114966E-02-0.20177848E-06 0.64732818E-11-0.74126978E-16
 0.19124285E+05 0.62595177E+02 0.33368304E+01 0.10016687E-02-0.27227648E-06
 0.34876004E-10-0.14592070E-14-0.10348727E+04 0.53569296E+01
E-                 selle E    1O    00    00    0G       200.00 30100.00 27300.00
 0.25000000E+01 0.00000000E+00 0.00000000E+00 0.00000000E+00 0.00000000E+00
-0.74537500E+03-0.11733975E+02 0.25000000E+01-0.81502608E-17 0.13029867E-20
-0.72648333E-25 0.13066247E-29-0.74537500E+03-0.11733975E+02
CHO+                       C    1H    1O    1            298.15   20000.00   3654.18
 0.69157265E+01 0.16631107E-03-0.18476343E-07 0.90856429E-12-0.16454441E-16
 0.96129333E+05-0.18089510E+02 0.28762768E+01 0.49486020E-02-0.23085306E-05
 0.51121752E-09-0.43520631E-13 0.99130022E+05 0.65020266E+01
H3O+                       H    3O    1                 298.15   20000.00   5430.90
 0.89508803E+01 0.25281668E-03-0.24594397E-07 0.10878318E-11-0.18090837E-16
 0.64480749E+05-0.33873319E+02 0.26885232E+01 0.54453654E-02-0.17055566E-05
 0.24833293E-09-0.13769440E-13 0.70890268E+05 0.63608217E+01
O2-                        O    2                      298.15    6000.00   2008.71
 0.42592867E+01 0.22468072E-03-0.51397955E-07 0.73545978E-11-0.38558652E-15
-0.72426252E+04 0.47599697E+00 0.31021718E+01 0.27980875E-02-0.22651126E-05
 0.86916517E-09-0.12721884E-12-0.68074793E+04 0.67609020E+01
CH5O+                      C    1H    5O    1         0300.00    5000.00   1000.00
 0.04029061E+02 0.09376593E-01-0.03050254E-04 0.04358793E-08-0.02224723E-12
 0.68531037E+05 0.02378195E+02 0.02660115E+02 0.07341508E-01 0.07170050E-04
-0.08793194E-07 0.02390570E-10 0.69335467E+05 0.11232631E+02
C2H3O+                     C    2H    3O    1           200.000   6000.000 1000.00
 0.53137165E+01 0.91737793E-02-0.33220386E-05 0.53947456E-09-0.32452368E-13
 0.76901865E+05-0.16757558E+01 0.40358705E+01 0.87729487E-03 0.30710010E-04
-0.39247565E-07 0.15296869E-10 0.77864832E+05 0.78617682E+01
OH-                L 3/93O    1H    1E    1     0G    298.150   6000.000 1000.
 2.83405701E+00 1.07058023E-03-2.62459398E-07 3.08376435E-11-1.31383862E-15
-1.80186974E+04 4.49464762E+00 3.43279956E+00 6.19656310E-04-1.89930992E-06
 2.37365946E-09-8.55103755E-13-1.82613086E+04 1.06053670E+00-1.72227709E+04
CO3-2                      C    1O    3E    2           150.00    3500.00    339.08
 0.94085556E+00 0.19045372E-01-0.17014037E-04 0.70874622E-08-0.11350500E-11
 0.30041857E+03 0.19220308E+02 0.49033350E+01-0.16993906E-01 0.10239114E-03
-0.16353731E-06 0.88205784E-10-0.39275852E+02 0.34119054E+01
CO3-                       DHO=-620kJ/mol            150.00    3500.00    339.08
 0.94085556E+00 0.19045372E-01-0.17014037E-04 0.70874622E-08-0.11350500E-11
-0.75559146E+05 0.19220308E+02 0.49033350E+01-0.16993906E-01 0.10239114E-03
-0.16353731E-06 0.88205784E-10-0.75898841E+05 0.34119054E+01
CHO2-                      H    1C    1O    2E    1     298.150   5000.000 1000.
 5.97791811E+00 3.24247847E-03-1.46666291E-06 2.91808902E-10-2.10704956E-14
-5.81813435E+04-7.12854015E+00-3.01936623E+01 2.54607495E-01-6.43484728E-04
 6.92943698E-07-2.65871657E-10-5.36791044E+04 1.47958586E+02
```

```
CHO3-                   H   1C   1O   3E   1    150.00   3500.50   244.14
 0.85898553E+00 0.22417430E-01-0.19057265E-04 0.79286650E-08-0.13068742E-11
-0.90747270E+05 0.20231833E+02 0.88717739E+01-0.10001250E+00 0.73793575E-03
-0.22314617E-05 0.26289221E-08-0.91194014E+05-0.79640994E+01
O-                RUS 89O   1E   1    0    0G   298.150  6000.000 1000.
 2.54474868E+00-4.66695419E-05 1.84912310E-08-3.18159131E-12 1.98962894E-16
 1.14822713E+04 4.52131018E+00 2.90805921E+00-1.69804907E-03 2.98069956E-06
-2.43835127E-09 7.61229313E-13 1.14138341E+04 2.80339097E+00
N2                selle N   20   00   00   0G      200.00 30100.00 16200.00
-0.79881200E+02 0.14669991E-01-0.87379270E-06 0.22241187E-10-0.20839676E-15
 0.35703769E+06 0.66412261E+03 0.31894328E+01 0.92107920E-03-0.22394465E-06
 0.20939065E-10-0.57639899E-15-0.98124572E+03 0.45795398E+01
```

Appendix C

Molecular data

This chapter lists all data used to calculate the transport properties of the methane-air gas mixture. These properties are the diffusion coefficients of all species in the mixture and the heat conductivity of the gas.

For the collision between electrons and the neutral species, differential momentum transfer cross sections are needed. Moreover, seven parameters are required for each neutral species: the two Lennard-Jones parameters (ϵ, σ), the permanent dipole q, the dipole and quadrupole polarizabilities (α, α_{q}), the dispersion coefficient C_6, and the rotational collision number Z_{rot}. Finally, four values are needed for each charged species, except for the electron. They are the numerical parameter n, the dipole polarizability α, the dispersion coefficient C_6, and the rotational collision number Z_{rot}. In addition, two more parameters per species are required, if the process of resonant charge transfer is taken into account.

The TRAPLA library is used for calculating the transport properties [Sel02, SRW98, SR99]. See Section 2.5 for details of the model, and Section 3.3 for information on the newly added data.

C.1 Electron-neutral species collision data

The total momentum transfer cross sections for the collision of electrons with the most abundant neutral species are given in the Tables C.1 and C.2. For the collision with N_2 and O, existing data sets have been used [Sel02]. The contribution of collisions with the other neutral species are neglected. Because of insufficient data in the literature, the assumption $Q^{(2)*}(E) = Q^{(1)*}(E) = Q_{\mathrm{m}}(E)$ has to be made for all collisions. The cross sections are shown only for collision energies up to 10 eV in the tables, which is sufficient for typical temperatures present in the methane-air flames under consideration.

E [eV]	Q_{m} [Å^2]				
	O_2, [LP78]	H_2, [BP85]	H_2O, [Phe03]	CO, [Lan78]	CO_2, [Phe03]
0.0000	0.3500	6.4000	50000.0000	60.0000	600.0000
0.0010	0.3500	6.4000	33000.0000	40.0000	540.0000
0.0020	0.3600	6.5000	16500.0000	25.0000	380.0000
0.0030	0.4000	6.6000	11000.0000	17.7000	307.0000
0.0050	0.5000	6.8000	6600.0000	12.3000	237.0000
0.0070	0.5800	7.1000	4710.0000	9.8000	200.0000
0.0085	0.6400	7.2000	3880.0000	8.6000	182.0000
0.0100	0.7000	7.3000	3300.0000	7.8000	170.0000
0.0150	0.8700	7.7000	2170.0000	6.5000	138.0000
0.0200	0.9900	8.0000	1610.0000	5.9000	120.0000
0.0300	1.2400	8.5000	1060.0000	5.4000	97.0000
0.0400	1.4400	8.9600	830.0000	5.2000	85.0000
0.0500	1.6000	9.2800	650.0000	5.4000	76.0000
0.0700	2.1000	9.8500	456.0000	6.1000	63.0000
0.1000	2.5000	10.5000	318.0000	7.3000	50.0000
0.1200	2.8000	10.8500	265.0000	7.7000	44.0000
0.1500	3.1000	11.4000	210.0000	8.8000	39.0000
0.1700	3.3000	11.6000	184.0000	9.3000	34.0000
0.2000	3.6000	12.0000	153.0000	10.0000	29.0000
0.2500	4.1000	12.5000	124.0000	11.2000	24.0000
0.3000	4.5000	13.0000	102.0000	12.1000	18.0000
0.3500	4.7000	13.4500	89.0000	13.0000	15.0000
0.4000	5.2000	13.9000	78.0000	13.8500	13.0000
0.5000	5.7000	14.7000	63.5000	15.4000	10.0000
0.7000	6.1000	16.3000	46.3000	16.5000	7.1000
1.0000	7.2000	17.4000	33.1000	18.5000	5.2000
1.2000	7.9000	17.8000	28.0000	28.0000	4.8000
1.3000	7.9000	18.0000	26.0000	37.0000	4.7000
1.5000	7.6000	18.2500	22.9000	42.0000	4.6500
1.7000	7.3000	18.2500	20.0000	40.0000	4.6500
1.9000	6.9000	18.1000	18.2000	32.0000	4.8500
2.1000	6.6000	17.9000	16.6000	23.5000	5.0500
2.2000	6.5000	17.7000	16.0000	21.5000	5.2000
2.5000	6.1000	17.0000	14.4000	17.5000	6.4000
2.8000	5.8000	16.4000	13.2000	16.0000	7.6000
3.0000	5.7000	16.0000	12.4000	15.4000	9.0000
3.3000	5.5000	15.6000	11.6000	14.6000	11.5000
3.6000	5.4500	14.8000	10.8000	14.2000	14.0000
4.0000	5.5000	14.0000	10.0000	13.8000	15.2000
4.5000	5.5500	13.1000	9.3000	13.3000	14.8000
5.0000	5.6000	12.2000	8.6000	12.9000	12.7000
6.0000	6.0000	10.4000	7.5500	12.3000	10.0000
7.0000	6.6000	8.9000	7.0500	11.8000	10.0000
8.0000	7.1000	7.8500	6.7000	11.3000	10.8000
10.0000	8.0000	6.0000	6.6000	10.6000	12.1000

Table C.1: Momentum transfer cross sections of significant electron-neutral collisions.

C_2H_2, [Hay90]							
E [eV]	0.012	0.032	0.034	0.053	0.118	0.196	0.361
Q_m [Å^2]	9.854	9.842	9.841	10.883	16.294	17.759	19.634
E [eV]	0.811	1.431	2.130	2.599	3.601	5.667	8.795
Q_m [Å^2]	20.782	20.767	23.300	25.405	18.747	10.819	6.909
E [eV]	16.653	32.903	80.418	147.962	351.266	907.692	
Q_m [Å^2]	4.810	3.301	1.904	1.067	0.345	0.080	
C_2H_4, [Hay90]							
E [eV]	0.012	0.025	0.043	0.059	0.071	0.079	0.088
Q_m [Å^2]	9.577	7.015	4.474	2.813	1.882	1.689	2.000
E [eV]	0.100	0.119	0.159	0.233	0.488	1.169	1.493
Q_m [Å^2]	3.275	4.964	7.521	10.224	14.535	21.301	22.634
E [eV]	2.189	3.358	4.702	7.559	11.252		
Q_m [Å^2]	20.602	17.626	16.549	17.300	16.238		
CH_4, [MHL95]							
E [eV]	0.010	0.016	0.024	0.037	0.065	0.093	0.12
Q_m [Å^2]	21.05	15.55	11.03	7.608	4.271	2.828	2.006
E [eV]	0.15	0.18	0.22	0.29	0.37	0.45	0.56
Q_m [Å^2]	1.257	0.8325	0.5147	0.3857	0.4244	0.6064	0.8783
E [eV]	0.74	0.93	1.26	2.06	2.97	4.16	5.45
Q_m [Å^2]	1.42	2.001	3.019	5.675	9.047	14.23	17.96
E [eV]	8.05	11.24					
Q_m [Å^2]	15.43	12.73					

Table C.2: Momentum transfer cross sections of significant electron-neutral collisions.

C.2 Uncharged species

Table C.3 contains the data of all neutral species needed to calculate the transport properties in the gas mixture. The seven values are the Lennard-Jones parameters (ϵ, σ), the permanent dipole q, the dipole and quadrupole polarizability (α, α_q), the dispersion coefficient C_6, and the rotational collision number Z_{rot}.

References for the new data are given in Section 3.3. With the exception of the dipoles, the polarizabilities, and the dispersion coefficients, all data is taken from [WMD97].

C.3 Charged species

Table C.4 lists the four values needed for each ion to calculate the transport properties. They are the parameter n for the (n,6,4)-potential, the dipole polarizability α, the dispersion coefficient C_6, and the rotational collision number Z_{rot}. References are given in Section 3.3.

As important resonant charge transfer process in a lean methane-air flame, the collision of the oxygen anion with the highly abundant oxygen molecule is taken into account:

$$O_2^- + O_2 \rightarrow O_2 + O_2^- \quad .$$

The experimental data for the collision integral, shown in Table C.5, is used to calculate the contribution of resonant charge transfer to this collision integral, see the Sections 2.5 and 3.3.

Fitting of the collision integral data yields the following parameters for resonant charge transfer (A_{rct}, B_{rct}):

Process	A_{rct}	B_{rct}
O_2^-/O_2	-1.854	29.842

.

Species	ϵ/k [K]	σ [Å]	q [Debye]	α [Å^3]	C_6/e^2 [Å^5]	Z_{rot}	α_{q} [Å^5]
N_2	98.400	3.652	0.000	1.740	2.995	4.500	3.602
O_2	121.100	3.407	0.000	1.581	2.555	6.000	3.136
O	80.000	2.750	0.000	0.802	0.733	0.000	0.798
CH^*	80.000	2.750	1.500	2.000	2.217	0.000	4.433
H	145.000	2.050	0.000	0.667	0.315	0.000	0.630
HCCO	436.000	3.970	0.000	3.677	6.007	2.000	6.641
HO_2	107.400	3.458	2.200	1.500	1.330	3.800	2.660
H_2	38.000	2.920	0.000	0.790	0.501	280.000	1.003
H_2O	572.400	2.605	1.844	1.500	1.479	2.100	2.958
H_2O_2	107.400	3.458	2.200	1.800	1.785	3.800	3.571
C	80.000	2.750	0.000	1.760	1.817	0.000	3.633
CH	80.000	2.750	1.500	2.000	2.217	0.000	4.433
CHO	498.000	3.590	2.000	2.500	2.643	0.000	5.287
$^1CH_2$	141.400	3.746	0.600	2.000	2.166	13.000	4.332
$^3CH_2$	141.400	3.746	0.600	2.000	2.166	13.000	4.332
CH_2O	498.000	3.590	2.330	2.770	4.348	2.000	8.696
CH_2OH	417.000	3.690	1.500	3.000	3.545	2.000	7.090
CH_2CHO	436.000	3.970	0.000	4.049	6.852	2.000	7.622
CH_2CH_2OH	417.000	3.690	1.700	4.855	8.776	2.000	9.878
CH_2CO	436.000	3.970	1.420	4.400	9.697	2.000	19.395
CH_3	141.400	3.746	0.000	2.200	2.481	13.000	4.961
CH_3O	417.000	3.690	2.000	2.900	4.696	2.000	9.391
CH_3OH	417.000	3.690	1.700	3.081	1.740	2.000	10.719
CH_3O_2	244.000	3.763	0.000	2.650	3.842	2.100	4.158
CH_3O_2H	417.000	3.690	1.700	3.081	4.719	2.000	5.157
CH_3CHO	436.000	3.970	2.690	4.278	9.751	2.000	19.501
CH_3CHOH	417.000	3.690	1.700	4.976	9.076	2.000	10.232
CH_3CO	436.000	3.970	2.800	4.000	5.834	2.000	11.667
CH_4	141.400	3.746	0.000	2.448	3.936	13.000	7.872
CO	98.100	3.650	0.112	1.953	2.784	1.800	5.568
CO_2	244.000	3.763	0.000	2.507	4.510	2.100	9.020
C_2H	209.000	4.100	0.700	3.000	5.442	2.500	10.885
C_2H_2	209.000	4.100	0.000	3.487	7.220	2.500	14.439
C_2H_3	209.000	4.100	0.700	3.500	5.264	2.500	10.528
C_2H_4	243.000	4.050	0.000	4.188	9.605	2.000	19.209
C_2H_5	246.000	4.320	0.300	4.000	6.764	2.000	13.529
C_2H_5O	417.000	3.690	2.200	4.000	7.592	2.000	15.184
C_2H_5OH	417.000	3.690	1.690	5.110	14.253	2.000	28.506
C_2H_6	246.000	4.320	0.000	4.226	10.716	2.000	24.216
OH	80.000	2.750	1.660	1.000	0.678	0.000	1.356

Table C.3: Molecular data for the calculation of transport properties: Uncharged species.

Species	n	α [Å^3]	C_6/e^2 [Å^5]	Z_{rot}
CHO^+	12.000	1.341	0.416	0.000
H_3O^+	12.000	0.964	0.967	10.000
O_2^-	12.000	1.581	0.059	3.800
$C_2H_3O^+$	12.000	3.036	4.625	2.000
CH_5O^+	12.000	2.126	4.308	2.000
OH^-	12.000	6.400	3.904	0.000
CO_3^-	12.000	4.900	3.364	0.000
CHO_2^-	12.000	5.100	4.739	0.000
CHO_3^-	12.000	5.100	4.994	0.000
O^-	12.000	3.200	0.779	0.000

Table C.4: Molecular data for the calculation of transport properties: Charged species.

T [K]	300.0	400.0	500.0	600.0	800.0	1000.0	1200.0
$\Omega^{(1,1)}$ [Å^2]	120.0	107.0	98.1	92.1	83.0	77.0	72.6
T [K]	1500.0	2000.0	2500.0	3000.0	4000.0		
$\Omega^{(1,1)}$ [Å^2]	67.9	62.7	59.3	56.7	53.8		

Table C.5: Data points of the collision integral $\Omega^{(1,1)}(T)$ for the collision of O_2^- with O_2 taken from [EPM76].

Appendix D

Symbols

α	dipole polarizability
α_{q}	quadrupole polarizability
A	Arrhenius parameter
A_{rct}	fit parameter for resonant charge transfer
B_{rct}	fit parameter for resonant charge transfer
b	collision impact parameter
β	ambipolarity of species
c	ambipolar charge diffusion flux or concentration
c^0	charge diffusion flux (Fick's law)
$\overline{C}_p$	molar heat capacity at constant pressure
C_6	dispersion coefficient
D_{a}	ambipolar diffusion coefficient
D	diffusion coefficient in mixture or binary diffusion coefficient
$\overline{D}$	average diffusion coefficient of heavy ions
$\Delta_r\overline{G}$	change of Gibbs energy in reaction r
$\Delta_r\overline{H}$	change of enthalpy in reaction r
$\Delta_f\overline{H}$	enthalpy of formation
$\Delta_r S$	change of entropy in reaction r
δ	parameter of Stockmayer potential
e	elementary charge
E	energy or electric field
E_{a}	activation energy
E^{a}	ambipolar electric field
E^{e}	external electric field
ϵ_0	permittivity of vacuum
ϵ	Lennard-Jones parameter
η	viscosity
Φ	equivalence ratio
ϕ	transformed spatial coordinate
γ	parameter of (n-6-4) potential
$\overline{H}$	molar enthalpy
I_{p}	ionization potential
j	ambipolar mass diffusion flux
j^0	mass diffusion flux (Fick's law)
$\tilde{j}$	total mass flux corrected diffusion flux
j_{H}	heat flux
k	Boltzmann constant or reaction rate coefficient

k^{-1}	reaction rate coefficient of backward reaction
K_c	equilibrium constant
λ	heat conductivity
λ_D	Debye length
n	number of moles, parameter of Arrhenius law, or parameter of (n,6,4)-potential
N_A	Avogadro constant
$\nu^{\mathrm{e,p}}$	stoichiometric coefficients for educts and products
M	molar mass or third body
$\overline{M}$	mean molar mass
M_{ij}	reduced molar mass
m	mass
μ	reduced mass or mobility
$\Omega^{(l,s)}$	collision integrals
$\Omega^{(l,s)*}$	reduced collision integrals
p	pressure
q	permanent electric dipole or differential collision cross section
Q_m	total momentum transfer cross section
$Q^{(l)}$	collision cross sections
$Q^{(l)*}$	reduced collision cross sections
Q_rct	contribution of resonant charge transfer to collision cross section
R	gas constant
$R^\pm$	fraction of a reaction of total production and consumption
r	chemical source term or separation of species in collision
$r^\pm$	integrated reaction rates for production and consumption
ρ	density
$\overline{S}$	molar entropy
σ	Lennard-Jones parameter
σ_e	electrical conductivity
S	species symbol
t	time
T	temperature
v	gas velocity
x	position in space
X	mole fraction
χ	scattering angle
Y	mass fraction
Z	charge number
Z_rot	rotational collision number
ξ	parameter of Stockmayer and (n-6-4) potential

Eidesstattliche Erklärung

Ich erkläre hiermit, daß ich die vorliegende Arbeit selbst verfaßt und mich dabei keiner anderen als der von mir ausdrücklich bezeichneten Quellen und Hilfen bedient habe.

Heidelberg, den 16.08.2005

Danksagung

An dieser Stelle möchte ich mich bei allen bedanken, die zum Gelingen dieser Arbeit beigetragen haben. Mein besonderer Dank gilt:

- Herrn Prof. Dr. Dr. h. c. Jürgen Warnatz für die Aufnahme in seine Arbeitsgruppe, die Auswahl des Themas und die jederzeitige Hilfsbereitschaft bei fachlichen und organisatorischen Fragen,
- Herrn PD Dr. Uwe Riedel für die wissenschaftliche Betreuung, die fachliche Freiheit und vor allem für die zusätzliche Unterstützung während der Endphase,
- Ingrid Hellwig und Barbara Werner für die vielen organisatorischen Hinweise und Hilfen,
- allen Mitgliedern des Internationalen Graduiertenkollegs „Complex processes: Modeling, Simulation and Optimization" für die Diskussionen, die Hilfsbereitschaft und die Möglichkeit, einen Einblick in andere Forschungsprojekte zu bekommen,
- Volker Karbach für die freundschaftliche Arbeitsatmosphäre, sein Interesse und seine Hilfsbereitschaft bei allen Problemen und Sven Sanwald für viele klärende Diskussionen,
- Conny Höhr für unendlich viele Dinge; Sebastian Eisebraun für das Korrekturlesen des Manuskripts,
- allen Kollegen der Forschungsgruppe „Reaktive Strömung" für ihre Hilfsbereitschaft, aber vor allem auch für die angenehme Zeit während der Arbeit und in der Freizeit,
- natürlich meinen Eltern für die Unterstützung, die sie mir während der gesamten Studienzeit gaben.